Title: Towards an understanding of the Ca isotopic signal related to ocean acidification and alkalinity overshoots in the rock record

Authors: Matthew S. Fantle[1,*] and Andy Ridgwell[2]

1 Department of Geosciences, Pennsylvania State University, University Park, PA 16802

2 Department of Earth Sciences, University of California, Riverside, CA 92521

* Corresponding author

email: mfantle@psu.edu
phone: 814-863-9968
fax: 814-863-7823

Keywords
Ca isotopes
Marine carbonates
Carbonate authigenesis
Reactive transport modeling
Earth System modeling
Ocean acidification

A manuscript submitted to *Chemical Geology* (Ca Isotope Special Issue)

---

0. Abstract

In this contribution, we explore the idea that the Ca isotope proxy has utility as an indicator of carbonate authigenesis (i.e., post-depositional precipitation of $CaCO_3$ within the sedimentary package). Given the strong contrast in isotopic fractionation factor between the formational and diagenetic environments, Ca isotopes have the potential to fingerprint carbonate authigenesis when it occurs close to the seawater-sediment interface. We demonstrate that Ca isotopes are particularly applicable to exploring ocean acidification events, and potentially ocean anoxic events, and focus our attention on ocean acidification related to the Paleocene-Eocene Thermal Maximum (PETM). We present three scenarios that vary in magnitude and duration of carbon fluxes simulated using an Earth System model of intermediate complexity (cGENIE) and use the cGENIE output to constrain the upper boundary conditions of 1-D reactive transport models of authigenesis and recrystallization in the sedimentary section. Along with simple mixing calculations, the models inform our exploration of the hypothesis that authigenic carbonate induced by a saturation state overshoot during the PETM explains recently published Ca isotope records, and perhaps bulk carbonate records over Ocean Anoxic Event (OAE) 2. Our simulations suggest that fractionation factor variability does not explain the PETM $\delta^{44}Ca$ records, and we propose a $\delta^{44}Ca$-$CaCO_3$ space framework to assist with the elucidation of authigenic additions over time scales that are short relative to the residence time of Ca in the ocean (~1 Ma). Ultimately, we find that the 'authigenic zone' generated in the sedimentary column may be influenced by alkalinity overshoots or redox state; the $CaCO_3$ produced in this zone can overprint temporal signals with depth-dependent signals that reflect lithology and sedimentation rate and need not be spatially uniform, even when driven by a global event. Ultimately, we demonstrate the utility of Ca isotopes for exploring short time scale climatic events and a quantitative framework to guide interpretations.

1. Introduction

Calcium isotopes have recently been applied as tools to identify ocean acidification events – intervals characterized by excess release of CO_2 to the ocean and/or atmosphere that drives coupled decreases in pH and carbonate ion concentration and, hence, carbonate saturation state (e.g., Hönisch et al., 2012) – in the geologic past (e.g., Payne et al., 2010; Hinojosa et al., 2012; Jost et al., 2014; Du Vivier et al., 2015). These studies generally have assumed that (1) ocean acidification modifies the marine Ca cycle, and that (2) the Ca isotopic composition ($\delta^{44}Ca$) of mineral phases, such as calcite and apatite, sample seawater and therefore serve as useful archives of global perturbations to the Ca cycle. Modification of the Ca cycle can arise as a result of reduced (i.e., due to dissolution associated with ocean acidification) or enhanced (i.e., due to precipitation during the alkalinity overshoot) Ca removal via burial of marine carbonates, and/or by changes (and particularly temperature-driven increases) in the weathering of terrestrial carbonates and Ca-bearing silicate minerals.

Thus, the promise of the $\delta^{44}Ca$ proxy is that it might serve as an indicator of the ocean acidification event itself or of enhanced rates of (calcium-) silicate weathering in the aftermath of massive CO_2 release. Conceptually, ocean acidification can impact the Ca isotopic composition of seawater by altering the flux balance of Ca into and out of the ocean (i.e., F_{sed}/F_w; DePaolo, 2004; Fantle and DePaolo, 2005; Fantle, 2010), changing the isotopic fractionation factor associated with carbonate sedimentary removal (e.g., Fantle, 2010; Du Vivier et al., 2015; Komar and Zeebe, 2016), and/or changing the isotopic composition of the input flux to the global ocean (Fantle and Tipper, 2014).

One critically important aspect of this manner of interpreting Ca isotopic composition is the assumption that seawater $\delta^{44}Ca$ is generally insensitive to change over time scales shorter than the residence time of Ca in the ocean. Because the Ca concentration of seawater throughout the Phanerozoic is generally constrained to be greater than (or similar to) that of the modern ocean (e.g., Horita et al., 2002), it is reasonable to assume oceanic residence times of Ca > 500 ka (e.g., Berner and Berner, 1996). This is longer than the ~300 ka silicate weathering feedback time-scale induced by geologically rapid CO_2 release (Lord et al., 2016) and, therefore, any Ca isotope signal of evolving marine $\delta^{44}Ca$ will be considerably damped. Indeed, ocean acidification events *sensu stricto* – that is, the coupled decline in both the pH and carbonate saturation state of the ocean – are a <100 ka time-scale phenomena and hence are significantly shorter than the residence time of Ca in the ocean. Thus, it seems unlikely that Ca isotopes are indicators of exogenic Ca cycle changes due to short time scale ocean acidification events. Only much longer-lasting (>1 Ma) episodes of enhanced CO_2 emissions would be expected to result in sustained elevated concentrations of CO_2 in the atmosphere and Ca fluxes to the ocean, and hence drive the isotopic evolution of the seawater reservoir.

An additional interpretive complication is that the Ca isotopic fractionation factor between carbonate sediments and seawater may be impacted by those geochemical changes associated with ocean acidification (particularly carbonate

saturation state). The apparent interpretive ambiguity that results can be illustrated by comparing two studies, both of which interpreted Ca isotopic variability in carbonates as a consequence of ocean acidification. Firstly, Payne et al. (2010) (and later Hinojosa et al., 2012) measured a substantial decrease in limestone (and later conodont) $\delta^{44}Ca$ associated with the end-Permian mass extinction. The authors interpreted the excursion, which occurred over a couple hundred thousand years, to be a result of ocean acidification driven by enhanced volcanism from large igneous province (LIP) emplacement. The preferred mechanism for this drop in $\delta^{44}Ca$ was an increase in the weathering input mass flux relative to the output mass flux of carbonate from the ocean. More recent work has suggested a similar mechanism as Payne et al (2010) – excess delivery of Ca via platform carbonate weathering associated with sea level regression – as the driver of the negative Ca isotope excursion at the P-T boundary (Wang et al., 2019).

Due to the difficultly in changing the $\delta^{44}Ca$ of the global ocean over short time scales via carbonate dissolution and/or a relative imbalance in the input and output fluxes, Komar and Zeebe (2016) suggested that a weathering feedback of the sort proposed by Payne et al. (2010) would not produce the coupled $\delta^{13}C$ and $\delta^{44}Ca$ trends observed. Instead, Komar and Zeebe (2016) suggest that the drop in $\delta^{44}Ca$ is explained by a change in the fractionation factor associated with carbonate precipitation. Similarly, Du Vivier et al. (2015) measured a relative increase in limestone $\delta^{44}Ca$ associated with Ocean Anoxic Event (OAE) 2 – another LIP emplacement event and assumed interval of enhanced CO_2 outgassing and ocean acidification. The $\delta^{44}Ca$ increase was likewise interpreted as a consequence of changes in the fractionation factor associated with calcite precipitation due to changes in seawater carbonate chemistry. In the simplest terms, the situation is confused: two LIP-driven events that are both associated with ocean acidification, though based on observed $\delta^{44}Ca$ changes that are opposite in sign.

Accordingly, without some means of discriminating between the two scenarios, the Ca isotopic proxy is ambiguous, which severely restricts its utility. This issue is an important one to resolve, as it prevents the straightforward use of the Ca isotope proxy and presents a barrier to the use of the proxy by those outside the Ca isotope community. If we are to move forward with the proxy, then, we must understand specifically how fractionation factor can impact the rock record and, more generally, how nuanced the interpretation of the Ca isotope record must be.

From a broader perspective, it is important to be able to identify relatively short time scale events in the geologic record unambiguously, particularly because ocean acidification associated with rapid/abrupt climate change is the nearest analog to modern-day climate change. Proxies other than carbon isotopes are important to have, especially given claims that the $\delta^{13}C$ of shallow ocean carbonates are significantly impacted by meteoric diagenesis (e.g., Swart, 2015 and references therein; Dyer et al., 2017). More generally, of course, the application of multiple proxies allows for a clearer picture of causative factors, and subsequent impacts on the Earth system, associated with a given event.

At present, we suggest that the Ca isotope proxy is characterized by ambiguity in its interpretation of ocean acidification events. Thus, in this

contribution. we attempt to clarify the issue. In particular, we explore the origin of so-called positive Ca isotopic anomalies via carbonate authigenesis, and evaluate the hypothesis that fractionation factor variability can explain such anomalies. Our exploration is guided by a series of model simulations, which examine geochemical and isotopic trends associated with ocean acidification at the global ocean and sedimentary column scales. Our overriding motivation, and in keeping with the theme of the special issue, is to support the continuing development of the Ca isotope proxy and to promote its utility as a means of reconstructing the past.

2. Authigenic Carbonate: A Link Between Ca Isotopes and Ocean Acidification

In this contribution, we propose that Ca isotopes are a useful and sensitive proxy for ocean acidification, but not in the manner outlined above. Our proposal is predicated on two observations of an ocean acidification event associated with the Paleocene-Eocene Thermal Maximum (PETM). Briefly, the Paleogene (65.5-23 Ma) is characterized by a series of 'hyperthermal' events, during which isotopically light carbon was released into the ocean-atmosphere system. The most prominent of these was the PETM, which occurred at ~55.5 Ma and is cited as one of the best analogs available for future carbon flux scenarios (Westerhold et al., 2012). The release of carbon during the PETM led to a geologically rapid (<10 ka), global increase in temperature at the Earth's surface that was as large as 9-10°C in the surface ocean and 4-5°C in the deep ocean (e.g., McInerney and Wing, 2011). The carbon input lowered ocean pH and carbonate ion concentration and resulted in decreased carbonate mineral preservation in deep-sea sediments. In some locations at the seafloor, carbonate content (i.e., wt. % $CaCO_3$) went to zero, leaving a clay interval in otherwise carbonate-rich oozes (e.g., Zachos et al., 2005). Contemporaneous with warming, as well as pH and carbonate ion concentration decreases, various proxies indicate that dissolved oxygen concentrations also generally declined during the PETM (e.g., Pagani et al., 2006; Sluijs et al., 2006; 2008; Weller and Stein, 2008; Nicolo et al., 2010; Schulte et al., 2011; Dickson et al., 2012; Wieczorek et al., 2013; Zhou et al., 2016; Yao et al., 2018).

The first observation that forms the basis of our proposal, then, is the overshoot in the depth of the carbonate compensation depth (CCD) that followed peak carbon input and the initial dissolution pulse. Both modeling (e.g., Dickens et al., 1997; Zeebe et al., 2009; Cui et al., 2011, Zeebe and Zachos, 2013; Gutjahr et al., 2017) and field measurements (e.g., Zachos et al., 2005; Röhl et al., 2007; Zeebe and Zachos, 2013; Penman et al., 2016) suggest that the overshoot was a global phenomenon, occurring over ~tens to hundreds of ka subsequent to ocean acidification as a consequence of alkalinity added to the ocean via temperature-enhanced silicate weathering (e.g., Kelly et al., 2005; Zeebe and Zachos, 2013). The overshoot, and its consequent impact on carbonate production and preservation in the water column, has been proposed to be responsible for the high and constant $CaCO_3$ contents observed at multiple deep-sea drilling sites. We contend that the overshoot, and specifically increases in bottom water saturation state, not only enhanced preservation of carbonate exported from the surface ocean, but also

provided favorable conditions for the precipitation of authigenic carbonate near the seawater-sediment interface.

The second relevant observation is the considerable variation in the $\delta^{44}Ca$ of marine carbonate sediments over the PETM (Fig. 1; Griffith et al., 2015). This work clearly demonstrated large shifts in sedimentary carbonate $\delta^{44}Ca$ associated with the PETM that occur over time scales that are considerably shorter than the assumed oceanic residence time. The observed shift is largest (~1‰) at ODP Site 1221, the deeper of the two sites and the site at which carbonate contents in the sedimentary column are the lowest, but it is also evident at the shallower Site 1212 (~40% of 1221 excursion; Fig. 1). Such sizeable changes in bulk carbonate $\delta^{44}Ca$ are not explained by evolving seawater $\delta^{44}Ca$ (e.g., Komar and Zeebe, 2011), and were not observed in marine barite (the ostensible "passive" tracer of seawater $\delta^{44}Ca$; Fantle, 2010) at ODP Site 1221. Instead, we contend that the trend in $\delta^{44}Ca$ is explained by the formation of authigenic carbonate from a seawater-like fluid, assuming a fractionation factor ($\alpha_{s\text{-}f}$) between authigenic carbonate and aqueous Ca of ~1 (i.e., 0‰; Fantle and DePaolo, 2007; Fantle, 2015; Griffith et al., 2015). Seawater is the isotopically heaviest reservoir on Earth (~1.9‰), and biogenic marine carbonate is typically offset from seawater by ~1.3‰ (Fantle and Tipper, 2014). There is, therefore, sizeable isotopic leverage to detect authigenic carbonate contributions to typical biogenic carbonates when authigenesis occurs close to the seawater-sediment interface.

The reader should bear in mind that recrystallization may be considered to be a form of authigenesis (literally "born in place"), though one in which the net mass of solid does not change. In the end, distinguishing between net addition of authigenic carbonate and recrystallization is not important to our narrative, as both mechanisms require the formation of a secondary carbonate phase with a significantly different Ca isotopic composition than primary carbonate, though it is an interesting second-order question.

In order for authigenesis to be a feasible explanation of the PETM data, authigenic carbonate would have to form within the diffusive boundary layer in the sedimentary column (i.e., from pore fluid whose $\delta^{44}Ca$ is distinct from that of bulk carbonates). This layer, which represents the depth range over which transport via diffusion (in most cases) and reaction compete effectively to maintain pore fluid $\delta^{44}Ca$ out of isotopic equilibrium with respect to the reacting solid, is on the order of 10 meters in recrystallizing carbonate-rich sections (e.g., Fantle and DePaolo, 2007; Fantle et al., 2010; Fantle, 2015), and on the order of 100 meters in sections where reaction (i.e., dissolution and/or recrystallization) is slower relative to transport (i.e., as at ODP Site 984; Turchyn and DePaolo, 2011). In either case, the isotopic effects of authigenic $CaCO_3$ addition will be limited to within tens of meters of the sediment-seawater interface. At greater depths, recrystallization and/or net dissolution of carbonates erase(s) the isotopic leverage to alter the solid (Fantle and DePaolo, 2007; Fantle et al., 2010; Fantle, 2015; Fantle et al., 2020) by adding Ca to the pore fluid that has the same isotopic composition as the reactive solid and attaining isotopic equilibrium (i.e., $\delta_{solid} - \delta_{fluid} = \Delta_{s-f}^{diagenetic}$; Fantle et al., 2020). In addition, the rate of authigenic carbonate formation would have to be relatively

slow such that there are limited rate-dependent kinetic isotope effects associated with calcite precipitation (see Fantle and Tipper, 2014 for summary of isotope effects associated with mineral precipitation; DePaolo, 2011; Steefel et al., 2014).

To evaluate if authigenesis can explain the PETM data from Sites 1221 and 1212 in a quantitative manner, we present a variety of simple mixing, reactive transport, and Earth System modeling results and analyses. Chief among the questions we address is whether a global event generates a global authigenic response as a consequence of the alkalinity overshoot associated with ocean acidification. In addition, we explore the hypothesis that lower O_2(aq) concentrations that accompany such events may impart an isotopically distinct authigenic signal. This, in turn, suggests a new use for Ca isotopes in exploring the evolution of oxidation state at the Earth's surface.

3. Computational/Modeling Methods

We utilized two numerical modeling constructs in this study. The first is the cGENIE Earth System Model (Ridgwell et al., 2007a) – an 'intermediate complexity' model that comprises a three-dimensional ocean circulation model with 2-D dynamic-thermodynamic sea ice component and energy-moisture balance atmospheric model, plus representation of the global carbon cycle. The specific PETM simulations utilized a CO_2 emissions forcing to the atmosphere that was identical to either that of (i) Gutjahr et al. (2017) or (ii) Gibbs et al. (2016) (i.e., twice the carbon flux of Zeebe et al., 2009). A simulation that matched the Cui et al. (2011) carbon emissions scenario was also run, though did not include Ca isotopes. Control scenarios that had no carbon forcing, as well as no change in Ca isotopic fractionation factor, were also conducted. All experiments were run following the spin-up for 200 ka from the onset of the PETM.

The second modeling effort utilized the multicomponent reactive flow and transport code CrunchTope (e.g., Druhan et al., 2013, Steefel et al., 2014). CrunchTope was used to simulate either carbonate authigenesis (i.e., net addition of solid with or without primary calcite dissolution) or recrystallization (i.e., coupled dissolution-precipitation with no net change in mass of the solid), while varying calcite saturation state, oxygen concentrations, and/or pH at the upper boundary. Because CrunchTope does not allow for a continuous change in boundary conditions, the temporal evolution of the upper boundary condition was set over three discrete intervals and the 'stop-restart' functionality of CrunchTope used (see SI for details). The chemistry over the intervals was constrained by the output from cGENIE, such that the coarse temporal evolution at the upper boundary matched the magnitude of change in the cGENIE simulations. Additional details on both modeling efforts are provided in the Supplementary Information (Sections S1 and S2; Fig. S1; Tables S1-S3).

4. Results and Discussion: Evaluating the Authigenic Hypothesis

In the discussion that follows, we present mass balance arguments in support of the hypothesis that authigenic contributions near the sediment-seawater interface have appropriate leverage to explain the PETM data at Sites 1212 and 1221. We then discuss the main ambiguity in the interpretation of Ca isotopic data, that of fractionation factor variability, and use the cGENIE simulations to support the contention that the fractionation factor in a PETM-like ocean changes minimally due to ocean acidification (given current understanding), and present testable hypotheses that allow us to evaluate this concept. We use the cGENIE output to explore how an authigenic carbonate signal associated with an ocean acidification event might look spatially, both from location to location at the seafloor and with depth in the sedimentary column, and evaluate the degree to which global drivers create spatially invariant signals. Both can impact how we interpret geochemical records of the past, and specifically whether we regard these signals as generated by local or global processes (e.g., Swart and Kennedy, 2012). We present reactive transport simulations of $CaCO_3$ authigenesis associated with the PETM overshoot, as well as the transient drop in oxygen concentrations in bottom waters that may have co-occurred with the rise in temperature and pCO_2. Finally, we propose an authigenic interpretation of OAE 2 Ca isotope records, and evaluate the feasibility of a fractionation factor-based explanation for these records.

4.1 Mass Balance Arguments Favoring an Authigenic Origin for PETM $\delta^{44}Ca$ Signals

The hypothesis of a detectable authigenic Ca isotope signal in the rock record is generally reasonable from an isotopic mass balance perspective (Fig. 2). Considering initial porosities between 0.6 and 0.9 and an authigenic endmember with a $\delta^{44}Ca$ of 1.9‰ (SRM-915a scale), filling between ~10% and 90% of the available pore space can explain the PETM data (Fig. 1; see SI for mixing equations). As the initial carbonate content of the sediment decreases, the amount of authigenic carbonate required to increase bulk carbonate $\delta^{44}Ca$ markedly (>0.5‰) decreases (Fig. 2). This simple estimate does not consider change in porosity as a function of compaction, as compaction is minimal in the upper tens of meters of the sedimentary column. This calculation also does not consider the recrystallization of existing carbonate (i.e., stable mineral recrystallization; e.g., Fantle and DePaolo, 2007; Fantle et al., 2010; Fantle, 2015; Gorski and Fantle, 2017; Lau et al., 2017; Ahm et al., 2018), a topic that is considered in subsequent sections.

If the addition of authigenic carbonate explains variability in the $\delta^{44}Ca$ of bulk sediment over ocean acidification events, then we expect to see a relationship between $\delta^{44}Ca$ and the $CaCO_3$ content of the sediment that can be used to identify such events in the rock record. In the simplest scenario, the carbonate content and the $\delta^{44}Ca$ should vary in a positive manner. One added complication is that carbonate content is also impacted by the flux from the surface ocean to the sedimentary column, which is a function of the balance between production in the surface ocean and the degree of preservation prior to burial (i.e., related to deep

water saturation state and dissolution kinetics in the water column). For instance, changes in the export flux of carbonate from the ocean have been noted to occur during the recovery phase of the PETM (e.g., Penman et al., 2016).

However, while $CaCO_3$ content in sediments may certainly vary on short time scales (i.e., less than the residence time of Ca in the ocean), variability in the $\delta^{44}Ca$ of this flux globally (and thus a relationship between $CaCO_3$ and $\delta^{44}Ca$) may only occur by changes in the fractionation factor ($\Delta^{44}Ca$). The trajectory of a fractionation factor change in $\delta^{44}Ca$-wt. % $CaCO_3$ space depends on whether or not there is a clear and consistent relationship between $\Delta^{44}Ca$ and biogenic production of $CaCO_3$, a topic we discuss in more detail below. Ultimately, while $CaCO_3$ and $\delta^{44}Ca$ may covary due to changes in fluid $\delta^{44}Ca$ values (i.e., global seawater $\delta^{44}Ca$) over time scales longer than the residence time, it seems reasonable to explore the short time scale PETM data for correlations between $CaCO_3$ content and $\delta^{44}Ca$ that are indicative of authigenesis. Following this exploration, we then discuss the likelihood of fractionation factor variability over ocean acidification events such as the PETM.

4.2 Simple Mixing Arguments for an Authigenic Origin for PETM $\delta^{44}Ca$ Signals

In the PETM data (Griffith et al., 2015), there are relationships between $CaCO_3$ content and $\delta^{44}Ca$ that are strongly suggestive of authigenic $CaCO_3$ additions. Given our assumptions regarding the isotopic compositions of the endmembers, the trajectories of the mixing relationships between $\delta^{44}Ca$ and weight percent $CaCO_3$ depend mainly on the initial carbonate content of the sediment (Fig. 3; see SI for mixing equations). Though we only consider one $\delta^{44}Ca$ value for the authigenic endmember, the reader should be aware that the $\delta^{44}Ca$ of the authigenic endmember may vary depending on where in the section it precipitates (open vs closed diagenetic system; e.g., Fantle et al., 2020); authigenesis carried out within the diffusive boundary layer will produce a phase that is isotopically distinct from the primary phase, while authigenesis below the depth of equilibration will not. Endmember $\delta^{44}Ca$ values will also depend on the $\delta^{44}Ca$ of the local water column (e.g., open ocean vs. coastal/near shore environments; Holmden et al., 2012) and potentially the mineralogy of the primary phase (e.g., Fantle et al., 2010; Blättler et al., 2012; Lau et al., 2017; Ahm et al., 2018). The former would generally decrease the leverage to alter by lowering the $\delta^{44}Ca$ of the fluid (e.g., due to mixing of riverine and/or submarine groundwater discharge with seawater). The latter is a result of a change in the fractionation factor associated with mineral precipitation and could either increase or decrease the leverage of the authigenic phase to alter bulk $\delta^{44}Ca$.

For a range of initial carbonate contents, then, the mixing curves can explain the Ca isotopic data that are anomalously high in the PETM intervals at both Sites 1212 and 1221 (Fig. 3a). Interestingly, the data from the shallower Site 1212 lie almost entirely on an authigenic carbonate mixing trend for a carbonate-rich sediment. Taken at face value, this suggests that the Ca isotopic variability at Sites 1212 and 1221 is authigenic in origin. This is entirely consistent, then, with the hypothesis that ocean acidification events promote authigenic carbonate formation

as a consequence of deep ocean oversaturation following the dissolution pulse. However, this preliminary analysis also suggests that the isotopic signal of authigenesis is somewhat complicated, as it theoretically extends at least tens of centimeters below the physical horizon that denotes the onset of the PETM. We explore this in more detail in Section 4.4.

4.3 Expectations for Fractionation Factor Variability Associated with Ocean Acidification

One potential interpretive complication with interpreting the $\delta^{44}Ca$-$CaCO_3$ mixing curves solely in terms of authigenesis is the presence of environmental signals, the relative importance of which depends critically on the time scale over which the Ca isotopic signal occurs. One of the most often cited causes of variations in carbonate $\delta^{44}Ca$ is a change in the fractionation factor associated with $CaCO_3$ formation. Some authors have also claimed that the original carbonate mineralogy (i.e., aragonite vs. calcite) can influence the Ca isotope record (Lau et al., 2017; Jost et al., 2017; Higgins et al., 2018), and the implications and caveats of this hypothesis have been explored in some detail previously (e.g., Fantle, 2010). Accordingly, we will concern ourselves here with the fractionation factor hypothesis, as this seems the most applicable to short time scale ocean acidification events.

Before beginning our analysis, it is worth noting that it is not clear if fractionation factor variability can be reasonably invoked when precipitation is biologically mediated or controlled. Most of the existing empirical relationships between fractionation factor and carbonate system chemistry, for instance, rely on abiotic/inorganic experiments. Given the regulated manner in which organisms, such as foraminifera (e.g., Erez, 2003), precipitate carbonate, it is not at all clear that such results can be used in global models to describe controls on the Ca isotopic composition of a biogenic carbonate output flux.

Further, experimental culture studies are ambiguous when it comes to the control of Ca isotopic fractionation by aqueous carbonate chemistry (Kisakürek et al., 2011; Mejia et al., 2018). If one takes the foraminiferal culture data at face value (e.g., Fig. 3 in Kisakürek et al., 2011), the preferred correlation between $\Delta^{44}Ca$ and carbonate ion concentration is not only weak (slope <0.0005 ‰/μM CO_3^{2-}) but also opposite in sign to the well-studied inorganic precipitation effect (e.g., Tang et al., 2008; 2012). Further, if one considers the growth rate effect on fractionation factor, it is equally unclear if and how carbonate producers respond to elevated CO_2 concentrations (e.g., Riebesell et al., 2000; Langer et al., 2006; Manno et al., 2012; Davis et al., 2017), thus complicating the application of the growth rate-$\Delta^{44}Ca$ correlation to carbonate sediments.

Because of these complications, we adopt the simplest approach and apply the inorganic experimental results of Lemarchand et al. (2004) and Tang et al. (2008; 2012) as a means of exploring previous suggestions that fractionation factor controls Ca isotope records of the past. Our objective is to examine spatial and temporal patterns produced in cGENIE and use this information to generate

predictions about what should be observed in cases where fractionation factor controls the Ca isotopic composition of the rock record.

4.3.1 General Discussion of Fractionation Factor Variability

As previously mentioned, over time scales less than the residence time of Ca in the ocean, variability in seawater δ^{44}Ca is insufficient to drive significant global differences in bulk carbonate δ^{44}Ca (Fig. 1; Komar and Zeebe, 2016). Therefore, during events lasting thousands to a few hundred thousand years, such as the PETM, (i) the $CaCO_3$ content of the sediment (via the balance between production and preservation and the addition of authigenic carbonate), (ii) authigenesis, and/or (iii) the fractionation factor may drive variability in δ^{44}Ca-$CaCO_3$ space. In the latter case, the expectation is that any shift in the fractionation factor in the surface ocean, for instance, due to ocean acidification should coincide with any shift in δ^{13}C, assuming that the decrease in δ^{13}C directly reflects ocean acidification. As we explore in more detail below, this means that any shift in fractionation factor will likely be heterogeneous in the global ocean and will reflect water column chemistry.

Over short time-scale events, the fractionation factor may impact carbonate sediment δ^{44}Ca either locally or globally. Local shifts will result in heterogeneous "anomalies" in the rock record that vary as a function of location and/or environment. In theory, it should be straightforward to identify such a mechanism by measuring contemporaneous carbonates from a range of locations. However, as is clear from the cGENIE modeling discussed below, even a global driver (such as pCO_2) can generate spatially variable signals (e.g., temperature and saturation state). Care must therefore be taken in discriminating between global and local effects, which can be aided by quantifying the spatial variability in saturation state or carbonate ion concentration using proxies or models.

One can also consider changes in the global fractionation factor over short time scales, though this must be thought out carefully. The global fractionation factor is a flux-weighted average (X_i) of all the output modes (i) that occur in the ocean (Fantle, 2010):

$$\Delta^{44}Ca_{output}^{global} = \sum_{outputs,i} \Delta^{44}Ca_i \cdot \frac{F_i}{\sum_i F_i} \; (= X_i) \qquad [2]$$

where $F_i/\sum_i F_i$ is the fraction of the global flux contributed to by the i^{th} output mode (i.e., X_i). The inorganic experimental data suggest that there are potentially two ways to drive changes in the global fractionation factor, keeping in mind the caveat above:

(1) By varying a single (or related) parameter(s), such as temperature or precipitation rate, globally, which drive(s) a fundamental change in $\Delta^{44}Ca_{input}^{global}$ (also referred to as $\Delta^{44}Ca_{sed}$). The expectation is that $\Delta^{44}Ca_i$ of all output modes change in a similar manner or that there is one dominant output mode, such that the effect on carbonate δ^{44}Ca is globally uniform.

(2) By varying one (or more) of the dominant output modes, such that $F_i/\sum_i F_i$ and/or $\Delta^{44}Ca_i$ associated with that mode. The driver of such a change can be local in origin.

An example of the second driver of global fractionation factor is a change in the proportion of Ca removed as aragonite, a topic that was explored in detail by Fantle (2010). Assuming that calcite and aragonite are the main output modes of Ca from the ocean, the global fractionation factor is described by: $\Delta^{44}Ca_{output}^{global} = \Delta^{44}Ca_{calcite} + X_{arag}\left(\Delta^{44}Ca_{arag} - \Delta^{44}Ca_{calcite}\right)$, where X_{arag} is the fraction of the total output flux removed as aragonite (Fantle, 2010). One suggestion has been that the biogenic calcite and aragonite output fluxes are isotopically distinct (Blättler et. al., 2012), and could therefore control seawater isotopic variability. However, post-depositional transformation of metastable phases can reduce the leverage of the aragonite flux to alter either seawater or bulk carbonate δ^{44}Ca (Fantle, 2010; Fantle and Higgins, 2014; Higgins et al., 2018). In order for aragonite output to impact the global fractionation factor, then, the aragonite must not react in the sedimentary column or it must do so in an effectively closed system.

4.3.2. cGENIE Model Constraints on Fractionation Factor Variability Associated with Ocean Acidification Events

Before beginning a discussion of our expectations regarding fractionation factor impacts on Ca isotopic records, which is predicated on cGENIE constraints on the chemical evolution of seawater over the event, we summarize the general output of the three PETM scenarios simulated — Gutjahr et al. (2017), Cui et al. (2011), and Gibbs et al. (2016). The general observations in all cases are similar (Fig. 4):

(1) A rise in temperature and alkalinity (due to carbonate dissolution), and a drop in pH, associated with an increase in atmospheric pCO_2;
(2) Occurrence of widespread seafloor undersaturation at the initiation of the carbon pulse, followed by an extended period of supersaturation (the "overshoot");
(3) A spatially-variable pattern of bottom water supersaturation during the overshoot;
(4) A spatially-variable distribution of sedimentary carbonate contents that reflect the balance between delivery of carbonate to the sedimentary column and core-top dissolution.

The surface saturation state with respect to calcite also exhibits spatial variability over the PETM, which is presented by subtracting the initial steady state spin-up for each simulation from the time at which the minimum saturation state occurs (46, 60, and 6 ka, respectively, for the three scenarios presented). At these times, large decreases in surface ocean saturation state occur in the western Pacific Ocean while much smaller variability is observed in the Southern Ocean and sub-

Arctic Pacific (Fig. S2). Within the thermocline, the trends are broadly similar: the largest drops in saturation state are focused in bands between 15 and 30˚N and 15 and 30˚S, while the South Atlantic exhibits a smaller drop in saturation state compared to surface waters. Recognizing the extent of the spatial variability in such a global scenario is critical, as it allows for some degree of ground-truthing (albeit model-based) when it comes to interpreting Ca isotopic records in terms of fractionation factor variability.

One of the commonly cited drivers of fractionation factor variability is temperature, which the PETM-specific cGENIE simulations suggest is not sufficient to explain the Ca isotope records from Sites 1212 and 1221. Temperature differences due to warming (relative to pre-event T) in the three scenarios investigated can be as much as ~5˚C or so throughout the water column. Given a fractionation factor sensitivity <0.02‰/˚C (e.g., Gussone et al., 2003; Langer et al., 2007; Griffith et al., 2008), one would need a temperature difference at a given location of at least 5-10˚C to see a resolvable signal (~0.1 to 0.2‰). Though the effect is in the right direction (smaller fractionation with increasing temperature), the magnitude of this effect is considerably smaller than what is observed at Sites 1212 and 1221 (Fig. 1b).

In addition, the maximum spatial heterogeneity in the PETM temperature anomaly is only ~1-2˚C at all water depths (shown for the surface ocean in Fig. S3). In other words, the spatial variance in temperature difference (relative to pre-event temperature distributions) is small. This means that site-to-site differences in carbonate $\delta^{44}Ca$ due to temperature-driven changes in fractionation factor over the PETM are likely less than 0.1‰. Temperature-driven changes in fractionation factor, therefore, do not explain the *differences* in the Ca isotope records at Sites 1212 and 1221 over the PETM.

Thus, we turn to those chemical parameters that are commonly cited as controlling the fractionation factor: the saturation state relative to calcite ($\Omega_{calcite}$) and the carbonate ion concentration. We considered variability in the fractionation factor as a function of either the relationship constrained by Lemarchand et al. (2004) and regressed by Gussone et al. (2005):

$$1000 \cdot ln\left(\alpha_{calcite-Ca^{2+}}\right) = -1.31 + 3.69 \cdot m_{CO_3^{2-}}[mmol/kg] \quad [3]$$

or the relationship between saturation state and fractionation factor suggested by Tang et al. (2012):

$$\Delta_{calcite-Ca^{2+}} = -0.067 \cdot \Omega_{calcite} - 0.321 \quad [4]$$

It is important to note that the former relationship (Eqn. 3) is similar to the one utilized by Komar and Zeebe (2016) in their LOSCAR simulation of the end-Permian $\delta^{44}Ca$ dataset published by Payne et al (2010), and that it is opposite in sense to the abiotic experimental data of Tang et al. (2008; 2012) (Eqn. 4; for summary, see Fig. 7 of Fantle and Tipper, 2014). Given the low ammonium concentrations in the experiments of Tang et al. (2008; 2012), these data are arguably more relevant to

the surface ocean, in which ammonium concentrations are negligible, and the sedimentary column (ammonium concentrations in sedimentary pore fluids are generally >100x lower than in the experiments of of Lemarchand et al. (2004) and Al Khatib and Eisenhauer (2017)).

The objective of the cGENIE simulations was to address two questions:

(1) Can fractionation factor variability driven by saturation state be responsible for the PETM-specific Ca isotopic trends noted by Griffith et al. (2015)?
(2) Are there any general lessons that can be gleaned from the PETM simulations that can be applied to similar events?

With regard to the first question, the results of the simulations at Site 1262 are plotted in δ^{44}Ca-$CaCO_3$ space for the carbon flux scenarios described above and the relationships in Eqns. 3 and 4 (Fig. 3a). Site 1262 is representative of a seafloor location that exhibits a strong decrease in sedimentary carbonate content over the PETM, and thus spans a range of $CaCO_3$ values. More muted variations in $CaCO_3$ are observed in the GENIE sedcore output at Sites 1221 and 1212 (Fig. 3a, also see Section 4.4 for discussion of Site 1212; Site 1221 not shown but minimum % $CacO_3$ is ~26% for the Cui et al. (2011) C release scenario), but the extent of variability in δ^{44}Ca is similar at all sites.

The simulations, which document a small change in carbonate δ^{44}Ca associated with ocean acidification over the PETM (Fig. 3a), support the contention that large changes in bulk carbonate δ^{44}Ca are not explained by variations in the fractionation factor associated with the enhanced carbon flux to the atmosphere over the PETM. Insofar as cGENIE accurately captures the processes that link carbonate δ^{44}Ca and water chemistry (i.e., surface water production and deep water/core top dissolution), there must be another explanation for the δ^{44}Ca data observed at Sites 1212 and 1221.

In contrast to earlier cGENIE model studies on contemporary ocean acidification that linked the $CaCO_3$:POC ratio directly to saturation state changes: $F_{z=h_e}^{CaCO_3} = \gamma \cdot r_0^{CaCO_3:POC} \cdot F_{z=h_e}^{POC}$ where $\gamma = (\Omega - 1)^n$ for $\Omega > 1$ (Ridgwell et al., 2007b), we did not consider changes in the carbonate production flux relative to particulate organic carbon (POC) production at the surface. However, such a mechanism moves one along a totally different trajectory than those described by the mixing lines (e.g., gray arrow in Fig. 3a), a conclusion that does not depend on the carbon flux scenario utilized.

Though large changes in bulk carbonate δ^{44}Ca are precluded, smaller changes driven by fractionation factor shifts may occur over the PETM. The maximum modeled drop in surface saturation state ($\Omega_{calcite}$) that is associated with the carbon isotope excursion (CIE) is ~60% (Cui et al. (2011) scenario). This would cause a maximum ~0.3‰ change in $\Delta_{calcite-Ca^{2+}}$, and the effect would be expressed regionally (i.e., in the western Pacific and Indian Oceans) and not globally (Fig. S2). Over most of the surface ocean, the change in $\Delta^{44}Ca_{calcite-Ca^{2+}}$ is more moderate,

between ~0.1 and 0.2‰ at most during the CIE. Such model-based estimates are useful, as they provide a first-order expectation for fractionation factor changes associated with the PETM that can guide the interpretation of future measurements and, potentially, Ca isotope records produced during other events.

With regard to the control of Ca isotopic records by fractionation factor variability, then, our analysis suggests a testable hypothesis: IF the fractionation factor can change over extreme events such as hyperthermals and ocean anoxic events, as a variety of authors have suggested, then there must be variability in the fractionation factor PRIOR to the event that is related to the spatial chemical heterogeneity in the surface ocean. Because there is spatial variability in saturation state and carbonate ion concentration (Fig. S4a and c), there should be resolvable variability (~0.4-0.5‰) in the $\delta^{44}Ca$ of the carbonate sedimentation flux from the ocean prior to the event (Fig. S4b and d).

To be clear, this heterogeneity is not related to heterogeneity in the $\delta^{44}Ca$ of seawater, which is spatially uniform; neither is this hypothesis applicable to locations in which fluid $\delta^{44}Ca$ is influenced locally (such as by riverine or submarine groundwater discharge; e.g., Holmden et al., 2012). Considering only, then, locations that receive carbonate formed from global seawater, our hypothesis is that if the fractionation factor can control Ca isotopes in the rock record, then there must be spatial variability in the $\delta^{44}Ca$ of contemporaneous carbonate sediment.

There is not an abundance of data to evaluate this hypothesis over the PETM. Based on the cGENIE-based constraints on water chemistry (i.e., of surface waters in which carbonate producers live), Sites 1212 and 1221 should contain contemporaneous bulk carbonates that have similar Ca isotopic compositions. The data, however, indicate that pre-PETM bulk carbonates at these sites are significantly different in Ca isotopic composition. Again, this suggests a factor other than differences in the fractionation factor as the causative factor. We therefore conclude that authigenesis explain the Ca isotope records over the PETM.

The significance of such a conclusion is multi-faceted. One aspect that we note here is that temporal mismatches in various geochemical proxy records are sometimes suggested to reflect unexpected changes in the geochemical cycles of those elements constrained by the proxy records, cycles which are then often described as “decoupled”. However, an authigenic signal communicated from the upper boundary overprints temporal signals in the depth domain. With regard to Ca isotopes, the possibility of a sizeable authigenic component obviates the need to invoke global scale decoupling of geochemical cycles, which can be difficult to explain.

4.4 Interpreting the Past Assuming the Presence of an Authigenic $\delta^{44}Ca$ Signal

In Section 4.3, we noted the expectation that a shift in the global fractionation factor associated with a change in seawater chemistry during ocean acidification events should be coincident with any shift in $\delta^{13}C$. The cGENIE simulations suggest that the same is generally true of $CaCO_3$ (Fig. 5). However, at Sites 1212 and 1221 over the

PETM, the maximum $\delta^{44}Ca$ value is offset from the minimum $CaCO_3$ content, and the increase in $\delta^{44}Ca$ at both sites appears correlated in the relative depth domain (Fig. 1).

One way to explain this observation is that dissolution induced by ocean acidification lowers the carbonate content during ocean acidification, and authigenic carbonate then "fills in" the gap from the top down during the alkalinity overshoot. At Site 1221, where $CaCO_3$ contents reach low values, such a scenario is not difficult to imagine, and is supported by our mixing analysis (Fig. 3). At Site 1212, the cGENIE model output suggests that dissolution could have been substantially greater than measured (drop from ~95% to ~80 wt. % $CaCO_3$; Fig. 1) if bioturbation was minimal. In the Gibbs et al. (2016) carbon emission scenario with no bioturbation, the modeled drop in carbonate content at Site 1212 associated with core-top dissolution was ~50 wt. % $CaCO_3$ (Fig. S5). To be consistent with the authigenic interpretation (Fig. 3a), the $CaCO_3$ content at Site 1212 prior to the overshoot would only have to be ~75 wt. % $CaCO_3$, which seems reasonable.

Thus, while it is feasible that the $\delta^{44}Ca$ signal reflects authigenic carbonate additions, this line of reasoning highlights the need to understand the depth range over which authigenesis generated from above can influence the sedimentary record. Accordingly, we turn to reactive transport modeling to address this question.

4.4.1 Reactive Transport Considerations of Authigenesis in the Marine Sedimentary Column

A variety of key questions arise when considering the hypothesis that authigenic carbonate formation, induced by a change in the chemistry of ocean bottom waters, plays a role in determining the Ca isotopic composition of marine sediments during the PETM and, perhaps, other intervals in Earth history. We focus on two related questions: (1) What controls the length scale over which authigenesis acts? and (2) how might an authigenic signal manifest itself in the rock record? We are not claiming that authigenesis is the explanation for all Ca isotope variability observed in the rock record, and there are doubtlessly other signals that are present. We should be clear that the authigenic signal we are discussing is imparted at or near the sediment-seawater interface, where the Ca isotopic leverage to alter the bulk sediment is the most extreme. This is not a deep, burial diagenetic signal and it will not affect all geochemical proxies in a similar manner.

The questions above are directly relevant to the interpretation of geochemical variations in the depth domain as temporal signals that reflect the evolution of the ocean-atmosphere system. It is important to remember that diagenetic processes act in the depth domain, and are not necessarily bound by temporal boundaries (though could be if properties such as grain size, surface area, for instance, covary with geochemistry over time). Diagenesis therefore can overprint temporal records with depth-dependent signals, which may result in misinterpreting the convoluted signal.

With this in mind, authigenic carbonate addition is a reasonable explanation of Ca isotopic variability in the rock record if the length scale over which this effect occurs is large enough to be detected or large relative to the length scale of features observed in the natural system. In the latter case, so-called Ca isotopic excursions are observed over meter to tens of meters length scales, while the variability over the PETM is observed over centimeter length scales (Fig. 1; e.g., Payne et al., 2010; Griffith et al., 2015). So, there is a considerable range of relevant length scales to consider.

In addition, the carbonate added must have a distinct isotopic composition relative to the bulk sediment. In carbonate-rich sediments, this is generally the case in the upper tens of meters of the sedimentary section (Fantle and DePaolo, 2007; Fantle, 2015). In sedimentary systems, the Ca isotopic composition of authigenic carbonate is a function of pore fluid $\delta^{44}Ca$ and the fractionation factor associated with marine carbonate precipitation, which is close to one (Fantle and DePaolo, 2007; Fantle, 2015). In the marine system, pore fluid $\delta^{44}Ca$ is initially the same as seawater (~1.9‰) and is altered in the sedimentary column by any process that puts isotopically distinct Ca into, or takes Ca out of (fractionating isotopically in the process), the pore fluid. The isotopic composition of the upper and lower boundaries can also influence pore fluid $\delta^{44}Ca$; the length scales over which the boundaries can influence pore fluids depend on the relative importance of transport (diffusion/advection) to reaction (e.g., Fantle et al., 2010).

To address these questions, we conducted two sets of authigenic precipitation simulations, which varied primarily in the lithology of the sedimentary column (Table S2). One set of runs was Site 1212-like (96% calcite at depths <175 cm, and 80% and 93% calcite in the upper 25 cm), while the other was Site 1221-like (40% and 60% calcite at depths <175 cm, and 1% calcite in the upper 25 cm). The burial lithology (i.e., the material added by sedimentation that is constrained by the measured % $CaCO_3$ at each site) also differs for each set of site simulations (82.5% calcite at Site 1221, in most cases, though simulations were also run with burial lithologies that were 1% calcite and 96% calcite; 95% calcite at Site 1212). The reader should be aware that the large changes in % $CaCO_3$ that are shown (e.g., in Fig. 7) are not authigenic, but reflect the change in burial lithology assumed for each site (refer to Table S2 for initial and burial lithologies).

Though there are no clear constraints on the rate constants for authigenic precipitation, the simulations suggest that rate constants ~10^{-11} mol/m^2/s can generate the sort of mixing patterns that are inferred at Sites 1212 and 1221. The mineral precipitation rates in the authigenic models are <10^{-4} mol/g/yr, which is two to three orders of magnitude slower than experimental rates at low to moderate saturation states (e.g., Zuddas and Mucci, 1998; Tang et al., 2008) yet faster than carbonate recrystallization rates in natural systems (e.g., Richter and DePaolo, 1987; 1988; Richter and Liang, 1993; Fantle and DePaolo, 2006; 2007; Fantle, 2015).

Assuming such rate constants, the length scale over which the upper boundary saturation state permeates into the sedimentary column at any given time is on the order of tens of centimeters. The length scale is a function of the transport flux (diffusive in this case) relative to the reaction rate (Fig. 6). Given the same

diffusive flux (similar porosity, diffusion coefficients, and concentration gradient), lowering the rate constant will increase the length scale. Assuming that the rate constant is the primary variable, and not the diffusion coefficient (or tortuosity), a larger length scale comes at the cost of slower authigenic carbonate accumulation. The time scale of the event will therefore also determine the amplitude of the authigenic signal, as will burial rate. Burial moves sediment through the zone of authigenesis, determining how much time a sediment package spends in the zone and distributing the signal in the depth domain. Assuming equal rate constants, a slower burial rate will result in greater accumulation of authigenic carbonate over a shorter length scale, compared to high burial rates in which authigenic additions are smaller and the isotopic signal is distributed over a longer length scale. This effect is clearly seen in the model simulations (Fig. 7).

The penetration of the upper boundary signal into the sedimentary column allows for the authigenic signal to stratigraphically "precede" the primary, depositional signal of the event. If one considers sedimentation rates on the order of 25 m/Ma (2.5 cm/ka), the apparent time lag is ~10 ka prior to the event; at lower sedimentation rates (e.g., sedimentation rates in the OAE 2 Portland #1 core are <1 cm/ka), the apparent time lag would be tens of thousands of years. This apparent time lag can be observed in the simulated Site 1221 depth profiles; in this case, the authigenic signal manifests as a local peak in bulk carbonate $\delta^{44}Ca$ that occurs at the edge of the siliciclastic section (Fig. 7b-c), which is material deposited *before* the alkalinity overshoot. A similar peak is observed in the measured data from Site 1221 (Fig. 7d). Such a peak is important to recognize, as it is not a temporal feature, but one associated with diagenetic processes occurring in the depth domain. That said, the peak does not occur at higher burial rates (Fig. 7d), because the siliciclastic unit does not spend appreciable time in the authigenic zone; however, the peak would reappear if precipitation kinetics increased by some mechanism (e.g., increased surface area). This is another example in which the isotopic signal could be misinterpreted as a temporal one, yet would only be present in sections that had slow enough burial and a carbonate-poor lithology exposed in the authigenic zone.

More generally, the simulation of authigenic carbonate precipitation induced by a change in the upper boundary is, as expected, consistent with the simple mixing calculations (Fig. 3b). In addition, the Ca isotopic compositon of the simulated bulk sediment clearly reflects the chemical evolution of the upper boundary condition over the event. Thus, even though Ca isotopes are impacted by a diagenetic process, they are useful for elucidating primary signals.

The simulations presented above are endmember simulations in which neither carbonate dissolution nor recrystallization is permitted. For this reason, pore fluid $\delta^{44}Ca$ does not change over the model domain. The impact of dissolution/recrystallization is to lower pore fluid $\delta^{44}Ca$ values closer to those of the reacting solid; such a shift would alter the leverage of authigenic carbonate to impact bulk carbonate $\delta^{44}Ca$.

The extent to which pore fluid $\delta^{44}Ca$ may change due to recrystallization is evaluated in simulations in which recrystallization of the bulk carbonate is permitted. The rate constants used are consistent with existing constraints on

carbonate recrystallization rates (~10^{-14} mol/m^2/s, which yields rates ~0.1 Ma^{-1}; Fantle and DePaolo, 2007; Fantle, 2015; Huber et al., 2017). In the presence of recrystallizing sediment, pore fluids exhibit <0.5‰ variability in isotopic composition (Fig. 8). Pore fluid $\delta^{44}Ca$ is initially pulled down to ~1.5‰ by bulk carbonate dissolution (as precipitation is assumed not to fractionate), but subsequently increases as the simulation proceeds and the bulk carbonate $\delta^{44}Ca$ evolves towards that of the pore fluid. This is a maximum estimate of the variability in pore fluid $\delta^{44}Ca$, as it assumes the entire solid is open to recrystallization. If the mass of reactive solid is smaller, the leverage to alter pore fluid $\delta^{44}Ca$ at a given rate is less (e.g., Chanda et al., 2019).

Though observations are scarce, such isotopic variability in the pore fluid is generally consistent with observations in the upper ~15 meters of carbonate-rich sedimentary sections (e.g., Fantle and DePaolo, 2007; Fantle, 2015; Higgins et al., 2018). The ultimate point is that even in the presence of recrystallization, isotopic leverage exists in the upper 2 meters of the section to generate isotopically distinct authigenic carbonate. This is expected given that the diffusive reaction length scale (i.e., the length scale over which the system remains somewhat open to transport) for Ca isotopes is on the order of meters to tens of meters (Fantle and DePaolo, 2006; Fantle and DePaolo, 2007; Fantle et al., 2010).

Recrystallization does not explain the PETM data if one assumes that all sedimentary carbonate is equally reactive. In this case, one expects increases in the $\delta^{44}Ca$ of the entire sedimentary package in the upper few meters of the section, with a diagenetic effect that scales with the carbonate content (Fig. 8). This is, as expected, generally similar to the trend expected at low extents of authigenesis, and generally highlights the difficulty disentangling authigenesis and recrystallization.

However, at the most rudimentary level, the interpretation of Ca isotopes as either a primary or diagenetic signal does not rely on distinguishing between authigenesis and recrystallization. The distinction does matter if we want to interpret the diagenetic signal or constrain the impact of authigenesis on the global Ca and/or C cycles (e.g., Schrag et al., 2013). The main differences between the two mechanisms are that recrystallization (i) does not produce any net change in the mass of carbonate in the section, and (ii) generates a dissolution flux that could, if large enough, impact pore fluid $\delta^{44}Ca$. Accordingly, the ideal recrystallization trend is a vertical line in $\delta^{44}Ca$-$CaCO_3$ space (Fig. 3). Thus, distinguishing between recrystallization and authigenesis is difficult at extremes in sedimentary carbonate content (i.e., extremely high and extremely low, such as we have at the PETM sites being explored).

To distinguish between authigenesis and recrystallization, acidification events in oceans with preserved pelagic carbonate records may prove to be ideal case studies. Specifically, sites that move below a shoaling CCD during the event present a “blank canvas” of sorts for authigenesis to impart a signal. In such sediments, where carbonate content is essentially zero, authigenesis can be the only means of drastically changing sedimentary $\delta^{44}Ca$ values. For this reason, future work should not ignore siliciclastic-dominated facies.

794 4.4.2 The Case for Ocean Anoxia as a Global Driver of Carbonate Authigenesis
795
796 One of the outstanding questions regarding a diagenetic origin of isotopic
797 excursions in the rock record is whether or not diagenesis can create effects that are
798 expressed globally. The question is relevant for a range of reasons, most notably
799 that the global expression of an excursion is often suggested either to preclude a
800 diagenetic origin or to argue for the expression of a primary marine signal (e.g.,
801 Halverson et al., 2002). This issue has been addressed in studies of shallow water
802 carbonate diagenesis (e.g., Swart and Eberli, 2005; Swart, 2008), which have
803 suggested global diagenetic drivers such as sea level change (e.g., Swart and
804 Kennedy, 2012) and increased terrestrial weathering rates (e.g., Cui et al., 2017). In
805 this study, we evaluate whether or not global events, such as ocean acidification, can
806 generate globally-expressed, diagenetically-produced geochemical signals.
807 The ambiguity in the logic that primary signals are globally uniform while
808 diagenetic signals are local can be appreciated by considering the example of an
809 ocean acidification event. Associated changes in ocean carbonate ion concentration
810 have been hypothesized to induce variations in the Ca isotopic fractionation factor
811 in biogenic carbonate, which is a primary (not a diagenetic) signal. In this scenario,
812 carbonate ion concentration changes are driven globally, but are not uniform in the
813 ocean (Fig. 4; Figs. S2 and S4). Thus, the Ca isotopic expression of this global event,
814 which is a primary signal, will vary from location to location in the ocean. Clear
815 interpretation therefore requires an understanding of how the Ca isotopic signal is
816 imparted and expectations for the variability given location, lithology,
817 sedimentation rate, etc.
818 One theme of this contribution is that global events may be expressed in the
819 sedimentary record via diagenetic processes, such as a saturation state overshoot
820 associated with an ocean acidification-hyperthermal event. However, an alkalinity
821 overshoot is not the only means of increasing saturation state in the sedimentary
822 column during such events; alkalinity also increases in marine sedimentary pore
823 fluids as sulfate is reduced. A general reaction is:
824
825 $$SO_4^{2-} + 2CH_2O \rightarrow HS^- + 2HCO_3^- + H^+ \quad [5]$$
826
827 though more complex formulations for organic matter (e.g., using Redfield ratios for
828 marine organic matter) and the chemical composition of the electron donor can be,
829 and have been, considered (e.g., Dale et al., 2006; 2008; Soetaert et al., 2007;
830 Bergmann et al., 2013; Arndt et al., 2013). The simple analysis presented herein
831 does not take into account the myriad of complexities surrounding redox reactions
832 in marine sediments (e.g., Arndt et al., 2013 and references therein).
833 In the modern ocean, the zone of sulfate reduction extends from meters to
834 hundreds of meters below the seafloor (Fig. S8), effectively traversing the gradient
835 in pore fluid Ca isotopic composition from seawater-like to carbonate-like. In
836 carbonate-rich sections, authigenic carbonate formed within the upper tens of
837 meters can be isotopically distinct, while authigenic carbonate formed deeper will
838 not be isotopically distinct from bulk carbonate. In order for sulfate reduction to be
839 a viable mechanism for producing isotopically distinct carbonate, sulfate reduction

must generally occur in the upper tens of meters of the sedimentary column (i.e., where pore fluid $\delta^{44}Ca$ is substantially higher than that of the bulk carbonate); this length scale can change depending on the rate at which carbonate dissolves or recrystallizes. In addition, sulfate reduction rates are influenced by a range of parameters, including O_2(aq) concentrations, temperature, sulfate concentrations, and the energetic favorability of the sulfate reduction reaction (e.g., vis- -vis the electron donors). A change in any, or a combination, of these factors can theoretically impact the depth over which sulfate reduction occurs.

In the three CO_2-release scenarios simulated using cGENIE, bottom water oxygen concentrations decreased transiently throughout the ocean over a period of 10 ka (Fig. 9); at some locations at the seafloor, depressed oxygen concentrations persisted over longer, 30 to 40 ka time scales. The change in aqueous oxygen concentration is uniform neither spatially nor with depth in the water column, which suggests that any O_2-related isotopic signal generated by this global event is likely to be expressed heterogeneously. Predictably, it is in deeper sediments that such a signal is most likely to be found (Fig. 9). The decrease in oxygen concentration coincides with the onset of the PETM, increase in export flux of POC, and the initial temperature increase. Accordingly, sulfate reduction must also occur at rates that produce sufficient alkalinity to counterbalance the drop in bottom water saturation state associated with the dissolution pulse.

It should be noted that of the small fraction of the surface ocean POC export flux that reaches the seafloor in cGENIE, none enters the sedimentary column by design and the residual deep ocean settling flux is reoxidized at the sediment-seawater interface (i.e., a 'reflective boundary' condition; Hülse et al., 2017). As a result, seafloor dissolved O_2 concentrations, and the oxygenation impact of changing POC export, will be slightly overestimated. But this hypothesis is worth evaluating, as there is evidence for low oxygen concentrations, and even anoxia, over the PETM (e.g., Pagani et al., 2006; Sluijs et al., 2006; 2008; Weller and Stein, 2008; Nicolo et al., 2010; Gruber, 2011; Schulte et al., 2011; Dickson et al., 2012; Wieczorek et al., 2013; Zhou et al., 2016; Yao et al., 2018). In addition, this mechanism makes possible two different time scales (and potentially depth scales) for an authigenic response: one associated with the main C pulse and one associated with the alkalinity overshoot.

We conduct a preliminary exploration of this hypothesis by utilizing the reactive transport model described in the SI (Section S2), which consists of a reactive network containing aerobic respiration, denitrification, and sulfate reduction (Table S2). The model is run to steady state over ~8 ka, and then perturbed using the cGENIE output to constrain the time scale of the perturbation and the extent to which oxygen concentration, pH, and saturation state decrease (Fig. 10a; Table S2). Our objective is to assess if, for a given sulfate reduction rate formulation, the PETM oxygen perturbation impacts the saturation state of calcite in the sedimentary column *relative to* the pre-perturbation steady state. We can use the same simulations to examine the length scale over which dissolution (driven from the upper boundary) impacts pore fluid $\delta^{44}Ca$. The latter determines if the

authigenic carbonate formed as a result of this process would be isotopically distinct relative to bulk carbonate.

The primary issue with the sulfate reduction hypothesis is that while sulfate reduction produces alkalinity, the canonical reaction (Eqn. 5) also produces protons. The same is true of sulfate reduction coupled to the oxidation of organic substrates such as glucose. In this scenario, without a local sink for H^+ or another source of alkalinity (e.g., carbonate dissolution: $H^+ + CaCO_3 \rightarrow Ca^{2+} + HCO_3^-$; Berner, 1966), the formation of authigenic carbonate is not energetically favorable. To illustrate this (as a reference case), we simulated sulfate reduction using glucose as the electron donor and assuming a rate constant that generates sulfate reduction rates comparable to those observed in the marine system (SI Section S2 and references therein). At these rates, and in the presence of calcite dissolution, pore fluids did not attain supersaturation with respect to calcite in the 10-meter model domain.

Interestingly, if acetate (CH_3COO^-) is the electron donor (e.g., Winfrey and Ward, 1983; Lovley and Klug, 1986; Brüchert and Arnosti, 2003; Dale et al., 2006; 2008; Glombitza et al., 2015; 2008; Beulig et al., 2018), then sulfate reduction does not produce H^+:

$$CH_3COO^- + SO_4^{2-} \leftrightarrow 2HCO_3^- + HS^- \quad [6]$$

For other energetically-favorable electron donors, such as H_2(aq) and formate (e.g., Abram and Nedwell, 1978; Dale et al., 2006; 2008; Larowe and Van Cappellen, 2011; Table 1 in Arndt et al., 2013; Adhikari et al., 2016; Glombitza et al., 2015; Beulig et al., 2018), protons are explicitly consumed in the sulfate reduction reaction:

$$4H_2(aq) + SO_4^{2-} + H^+ \leftrightarrow HS^- + 4H_2O \quad [7]$$

$$4CHO_2^- + SO_4^{2-} + H^+ \leftrightarrow 4HCO_3^- + HS^- \quad [8]$$

Though the microbial reaction network in nature is admittedly far more complicated than we consider, it seems at least plausible that sulfate reduction can induce authigenic carbonate precipitation over some length scale in the sedimentary section if acetate, formate, and/or hydrogen are involved. Accordingly, we explore an endmember model in which sulfate reduction uses acetate as an electron donor (i.e., acetotrophic sulfate reduction) and quantify the impact of a PETM-like ocean acidification perturbation on calcite saturation state in the upper 10 meters of the sedimentary section.

The reactive transport modeling suggests that acetotrophic sulfate reduction has the potential to enhance authigenic carbonate formation in the upper 10 meters of the sedimentary section (Fig. 10). Over the PETM-like acidification event (Fig. 10a), the drop in O_2(aq) at the upper boundary increases sulfate reduction rates at depth, which induces an increase in calcite saturation state relative to the pre-perturbation steady state. Model sulfate reduction rates in the upper 10 m are $<8 \cdot 10^{-6}$ mol/kg water/yr, which are consistent with rates inferred for deep-sea sediments and are $\sim 10^4$ times slower than rates inferred in coastal settings (SI Section S2). Thus, the rates are not so high that the hypothesis is untenable. It is also

worth noting that while the absolute saturation state values are likely not entirely accurate due to the closed lower boundary condition and size of the model domain, the endmember scenario is consistent with an increase in saturation state over meter length scales.

It is also clear from the simulations that dissolution induced from the upper boundary condition over the perturbation has no substantive effect on pore fluid $\delta^{44}Ca$. Dissolution occurs within the upper tens of centimeters of the section, consistent with observations of burndown. However, the dissolution rate is too slow to impact pore fluid $\delta^{44}Ca$, which is maintained at seawater values via diffusive communication with bottom waters. This is in contrast to the recrystallization scenario (Fig. 8), in which pore fluid $\delta^{44}Ca$ is impacted even at rates of dissolution that are comparable to the dissolution/burndown scenario. The reason for this difference is that recrystallization occurs throughout the model domain, at depths that preclude rapid diffusive communication with bottom waters; such conditions result in the development of a pore fluid isotopic gradient. Further, while the burial rate extends the zone over which dissolution is seen, and will by extension affect the depth interval over which authigenic addition is observed (as in the overshoot simulations), increasing burial rates does not change the depth scale over which the alkalinity increase occurs.

While this mechanism is speculative, as it depends on a reaction network that is currently the topic of debate in the scientific community, it suggests that the Ca isotope proxy might have utility that extends beyond its current reach. More specifically, it offers a means of explaining authigenic enrichments during ocean anoxic events that do not require ocean acidification (see Section 4.4.3). Finally, this hypothesis leads to the intriguing suggestion that the formation of authigenic carbonate is linked to the identity/chemistry of the electron donor. Though this is likely complicated, it does suggest that there is still fertile (and perhaps unexpected) ground to be explored with regard to the Ca isotope proxy.

4.4.3. The Role of Authigenesis in Other Deep-Time Records

Assuming that the PETM carbon perturbation (and associated changes in saturation state) is a reasonable analog for carbon perturbations associated with other events in deep time, we can evaluate the impact of authigenesis on other records. Ocean Anoxic Event 2 (OAE 2) is an excellent case study because of the high-quality Ca isotope work produced to date (Blättler et al., 2011; Du Vivier et al., 2015), and because the records exhibit the direction of change that one would associate with shallow carbonate authigenesis. Additionally, the magnitude of the fractionation factor change inferred for the PETM based on cGENIE modeling is consistent with the size of the anomalies reported in OAE 2 Ca isotope records by Du Vivier et al. (2015). Yet questions remain that may be addressed by an authigenic mechanism; at the very least, a discussion of the OAE 2 data will help us identify any outstanding questions that might guide future applications of the Ca isotope proxy to such events.

The Portland #1 core Ca isotopic record over OAE 2 (Fig. 11; Fig. S7) exhibits a negative trend in δ^{44}Ca-wt. % $CaCO_3$ space, which could be interpreted as either a dissolution trend (in the case of a heterogeneous sediment) or a long-term (~1.3 Ma) environmental signal (Du Vivier et al., 2015). A number of datums, which fall off this larger trend, were previously hypothesized to reflect a change in the global fractionation factor over ~600 ka (Du Vivier et al., 2015). We suggest that these δ^{44}Ca data may be explained by authigenic addition of $CaCO_3$ (Fig. 11); just as with fractionation factor variability, however, authigenesis alone cannot explain the increase in $CaCO_3$ content over OAE 2, as there is no unambiguous progression along a simple mixing curve. Instead, we suggest that the Portland #1 core was affected by at least two processes: (i) an increase in relative delivery (or preservation) of $CaCO_3$, and (ii) authigenesis. According to this hypothesis, authigenesis controls the Ca isotopic signal, while the former explains most of the offset to higher $CaCO_3$. This is consistent with suggestions that carbonate content in the Portland #1 core increased as a consequence of reduced siliciclastic delivery (e.g., Meyers et al., 2001), a hypothesis that doesn't *preclude* components of the signal derived via authigenesis

From a Ca isotopic perspective, two other records, Oyubari and Eastbourne, are also consistent with authigenesis (Fig. 11; Du Vivier et al., 2015). Oyubari, in particular, is fascinating, as it occurs at the low end of the $CaCO_3$ range (much like the PETM record at Site 1221), and closely follows the trajectory of the mixing curve. We predict that authigenic additions could explain Portland #1 and Oyubari by increasing the $CaCO_3$ content by <0.9 (Oyubari) to ~5 wt. % (Portland #1) (Fig. 11); such additions (ignoring the effect of any contemporaneous dissolution) would decrease porosity by <<1 to as much as 30%. Theoretically, Eastbourne would require a more sizeable addition but, because it is unclear what the baseline carbonate δ^{44}Ca is, we do not make an estimate of the authigenic addition.

To be absolutely clear, we are not unequivocally stating that the Ca isotopic trends associated with OAE 2 are authigenic in origin. However, we are suggesting that it is plausible, and it represents a viable mechanism that should be considered. If authigenesis explains the Ca isotopic records, this does not necessarily preclude a connection to ocean acidification, as has been hypothesized previously (Du Vivier et al., 2015). However, instead of being driven by the fractionation factor, the Ca isotope record is a result of authigenesis promoted by a saturation state overshoot or, as described above, deoxygenation of the sedimentary column. Authigenesis explains the spatially-variable, yet synchronous, nature of the OAE 2 records (i.e., not the same magnitude at all locales over the event), even though they are ostensibly associated with a global driver (i.e., ocean acidification). Authigenesis also explains the positive nature of the excursion, the correspondence with mixing lines, and the temporally abrupt nature of the excursion.

The alternate hypothesis that fractionation factor variability explains the Ca isotopic records over OAE 2 is consistent with the rate at which carbonate ion concentrations and saturation state change over ocean acidification events generated by extremely rapid C emissions (Fig. 4). However, the fractionation factor decrease of ~0.15‰ suggested to accompany an acidification event generated by

CLIP volcanism (Du Vivier et al., 2015) is inconsistent with foraminiferal culture data (e.g., Kisakürek et al., 2011), which imply an *increase* in carbonate ion concentration of >300 μM during OAE 2 (*NB*: Mejia et al. (2018) present culture data for coccolithophores, yet no experimental pH, alkalinity, or carbonate system data are available to apply their results consistently to this analysis.).

Not only do carbonate ion concentrations *drop* over CO_2-induced ocean acidification events (e.g., Fig. 4), but the absolute value of such a perturbation is more than 25 times larger than the change simulated to occur over the PETM (itself a rather sizeable ocean acidification event over which the maximum simulated drop in carbonate ion concentration in the surface ocean is ~30%; Figs. 4 and S4e-f). In order for this issue of magnitude to be resolved, and ignoring the sign of the perturbation, the biogenic carbonates measured by Du Vivier et al. (2015) must follow the inorganic calcite slope of Tang et al. (2008; 2012). If the biological isotope effect was associated with an alkalinity overshoot during the recovery from ocean acidification, instead of acidification, this could explain the Du Vivier et al. (2015) OAE 2 data. However, one would expect to see the acidification signal first, followed by the overshoot signal, which is not observed in the OAE 2 records.

Finally, it is important to stress that whereas carbon isotopes can act as indicators of diagenetic alteration, they may not be useful indicators in this instance. Though $\delta^{13}C$ is typically utilized to indicate authigenesis induced by the oxidation of organic matter or methane deeper in the sedimentary column, the overshoot mechanism operates differently: it is driven by bottom water chemistry that promotes carbonate authigenesis and need not be accompanied by a $\delta^{13}C$ signal (i.e., bottom water $\delta^{13}C$ DIC) that differs from the primary DIC $\delta^{13}C$. We do not include any quantitative considerations of $\delta^{13}C$ in our calculations or models for the simple fact that $\delta^{13}C$ of the authigenic phase is expected to be similar to the primary phase, such that there is little to no leverage to alter $\delta^{13}C$ in this case. Thus, there need not be a low $\delta^{13}C$ diagenetic component in the OAE 2 cores for our hypothesis to be valid.

Given the fact that significant portions of the seafloor may have been driven anoxic during OAE 2, it is also possible that the zone of sulfate reduction effectively migrated upwards (Section 4.4.2; e.g., Barnes et al., 2020), such that authigenic carbonate was produced over a depth range at which pore fluid $\delta^{44}Ca$ was closer to seawater than bulk carbonate values. Our simulations suggest that this can occur over >1 meter length scales, which is sufficient to explain OAE 2-type trends. It should be noted that such an authigenic signal is likely to have a distinct C isotopic composition compared to the alkalinity overshoot case (e.g., Barnes et al., 2020). The C isotopic offset will depend on a few parameters, including the rate of sulfate reduction and the depth at which the signal is acquired. Though we do not explore this is any detail in this contribution, it is worth noting that the three Portland #1 samples with the highest $\delta^{44}Ca$ values also have the lowest $\delta^{13}C$ values (Sageman et al., 2006).

5. Summary and Remaining Questions

In this contribution, we propose Ca isotopes as a sensitive proxy of ocean acidification, an application of the Ca isotope proxy that takes advantage of (i) the largest Ca isotopic gradient in the Earth system (i.e., that between seawater and marine carbonates) and (ii) the occurrence of alkalinity or saturation state overshoots during hyperthermal events. We suggest that Ca isotopes can identify authigenic carbonate in the rock record, if that carbonate forms within the diffusive boundary layer in the sedimentary column. Carbonate generated in this manner is isotopically distinct, unlike that formed during burial diagenesis, where the leverage to alter bulk carbonate values is typically extremely small (e.g., Fantle et al., 2010). Accordingly, we demonstrate how the formation of authigenic carbonate can be evaluated in δ^{44}Ca-$CaCO_3$ space and subsequently tie existing Ca isotopic data over the PETM and potentially OAE 2 to authigenesis. Because explaining large changes in the δ^{44}Ca of carbonates over relatively short time scales infers large and unreasonable changes in the exogenic Ca cycle, the authigenic mechanism provides a reasonable and intrepretable alternative to Ca cycle-driven changes.

Importantly, the formation of authigenic carbonate can be driven globally (e.g., as in a hyperthermal event such as the PETM) but the geochemical expression of such a global event need not be spatially uniform. The data from ODP Sites 1212 and 1221 and the cGENIE simulations presented herein both demonstrate that the intensity of the authigenic signal is likely not homogeneous across the global ocean. Thus, there should be no unqualified expectation that all records display the same trends in response to a global driver. This is also true of primary signals that are driven by global ocean acidification events, such as fractionation factor variability. The recognition that a global event need not impart a globally consistent geochemical signal highlights the utility of Ca isotopes for mapping out spatial variations in ocean chemistry during alkalinity overshoots.

We also suggest that decreases in bottom water O_2(aq) concentrations can effectively shift the zone of authigenesis related to sulfate reduction in the sedimentary column towards the seawater-sediment interface. If electron donors such as acetate, formate, and hydrogen participate to a significant extent in sulfate reduction, then the chemistry favors the generation of supersaturation states in the upper part of the sedimentary section in which pore fluid δ^{44}Ca is seawater-like. An interesting corollary to this hypothesis, which emphasizes events that *enhance* the production of authigenic carbonate, is a scenario in which a climatic or ocean chemical perturbation reduces the authigenic signal (i.e., by lowering sulfate reduction rates). This raises the intriguing possibility of Ca isotope excursions that move in the opposite direction as those explored in this study.

An advantage of the interpretative framework described in this study is that the Ca isotopic signal of shallow authigenesis is predictable and constant over geologic time: authigenic carbonate formed within tens to hundreds of centimeters of the seawater-sediment interface will always shift bulk sediment to higher δ^{44}Ca values. The mixing trend in δ^{44}Ca-$CaCO_3$ space should be distinct from fractionation

factor changes, though difficult to distinguish from recrystallization. Given what is known about recrystallization rates, however, it seems likely that recrystallization cannot create such trends over short length scales. Further, the amplitude of the authigenic signal is simply limited by the relative mass of authigenic carbonate added to the bulk sediment, and the technique is applicable to a bulk sediment proxy archive over a variety of time scales. The framework also suggests that sample collection should not necessarily focus only on rocks with high carbonate contents, and that there should be an expectation of isotopic effects as one crosses lithologic boundaries.

Future work should focus on identifying geochemical proxies that have distinct differences in elemental and isotopic partitioning between the surface ocean and sedimentary column (e.g., oxygen isotopes, Sr/Ca, Mg/Ca, U/Ca), which can be used in conjunction with Ca isotopes as diagenetic indicators to aid in distinguishing between primary and diagenetic signals (e.g., Fantle et al., 2020). Applying multiple diagenetic indicators is necessary because the isotopic and/or elemental partitioning contrast needed to fingerprint diagenesis may not always be present in the sedimentary column (Fantle et al., 2020). Reliance on Sr isotopes, C isotopes, or Mn concentrations, for instance, as unambiguous diagenetic indicators can lead to interpretations that are not properly informed.

In addition, there is a need to advance our understanding of biologically-mediated isotope effects, in particular the extent to which changes in seawater chemistry impact Ca isotopic fractionation during biologically-mediated $CaCO_3$ precipitation. Because parameters co-vary in natural systems in ways that can complicate the application of culture studies in a simple manner, a robust mechanistic model for such effects is needed. Although recent work has attempted to move in this direction (Mejia et al., 2018), our understanding remains incomplete.

Ultimately, if Ca isotopes prove an effective proxy for authigenesis at the sediment-seawater interface, it may be possible to use Ca isotopes (in conjunction with other tools) to probe the dynamics of the Earth system in novel (and perhaps unexpected) ways. Indeed, Ca isotopes may prove of great utility for elucidating the strength of the weathering feedback over geologic time scales, for constraining the organic substrates participating in sulfate reduction, or as an indicator of surface oxidation state.

Acknowledgements

The CrunchTope work could not have been completed without the sage advice, and considerable patience, of Dr. J. Druhan. MSF also thanks Ben Barnes for extremely helpful, and wide-ranging, discussions, and for sharing his opinion and specific suggestions for revisions of this manuscript. The authors thank one anonymous reviewer, Andy Jacobson, Guest Editor Elizabeth Griffith, and Editor Don Porcelli for helpful comments and advice on revisions. A. Ridgwell acknowledges funding from the European Research Council as part of the "PALEOGENiE" project (ERC-2013-CoG-617313) as well as from the Heising Simons Foundation.

References

Abram, J. W. and Nedwell, D. B. (1978) Hydrogen as a substrate for methanogenesis and sulfate reduction in anaerobic saltmarsh sediment. *Archives of Microbiology* 117, 93-97.

Adhikari, R.R., Glombitza, C., Nickel, J.C., Anderson, C.H., Dunlea, A.G., Spivack, A.J., Murray, R.W., D'Hondt, S. and Kallmeyer, J. (2016) Hydrogen Utilization Potential in Subsurface Sediments. *Frontiers in Microbiology* 7.

Ahm, A.S.C., Bjerrum, C.J., Blattler, C.L., Swart, P.K. and Higgins, J.A. (2018) Quantifying early marine diagenesis in shallow-water carbonate sediments. Geochim Cosmochim Acta 236, 140-159.

Al Khatib, M. and Eisenhauer, A. (2017) Calcium and strontium isotope fractionation in aqueous solutions as a function of temperature and reaction rate; I. Calcite. *Geochim Cosmochim Acta* 209, 296-319.

Arndt, S., Jorgensen, B.B., LaRowe, D.E., Middelburg, J.J., Pancost, R.D. and Regnier, P. (2013) Quantifying the degradation of organic matter in marine sediments: A review and synthesis. *Ear Sci Rev* 123, 53-86.

Barnes, B.D., Husson, J.M., Peters, S.E. (2020) Authigenic carbonate burial in the Late Devonian–Early Mississippian Bakken Formation (Williston Basin, USA). *Sedimentology*, https://doi.org/10.1111/sed.12695.

Bergmann, K.D., Grotzinger, J.P. and Fischer, W.W. (2013) Biological influences on seafloor carbonate precipitation. *Palaios* 28, 99-115.

Berner, R.A. (1966) Chemical Diagenesis of Some Modern Carbonate Sediments. *Am J Sci* 264, 1-36.

Berner, R.A. (1978) Sulfate reduction and rate of deposition of marine sediments. *Earth Planet Sci Lett* 37, 492-498.

Berner, R.A. (1980) Early diagenesis: a theoretical approach. Princeton University Press, Princeton, N.J.

Berner, E. K. and Berner, R. A., (1996). Global environment: water, air, and geochemical cycles. Prentice Hall, Upper Saddle River, N.J.

Beulig, F., Røy, H., Glombitza, C. and Jørgensen, B.B. (2018) Control on rate and pathway of anaerobic organic carbon degradation in the seabed. *Proc Natl Acad Sci* USA 115, 367-372.

Blattler, C.L., Jenkyns, H.C., Reynard, L.M. and Henderson, G.M. (2011) Significant increases in global weathering during Oceanic Anoxic Events 1a and 2 indicated by calcium isotopes. *Earth Planet Sci Lett* 309, 77-88.

Blattler, C.L., Henderson, G.M. and Jenkyns, H.C. (2012) Explaining the Phanerozoic Ca isotope history of seawater. *Geology* 40, 843-846.

Brüchert, V. and Arnosti, C. (2003) Anaerobic carbon transformation: experimental studies with flow-through cells. *Mar Chem* 80, 171-183.

Chanda, P., Gorski, C. A., Oakes, R. L. and Fantle, M. S. (2019) Low temperature stable mineral recrystallization of foraminiferal tests and implications for the fidelity of geochemical proxies. *Earth Planet Sci Lett* 506, 428-440.

Cui, Y., Kump, L. R., Ridgwell, A. J., Charles, A. J., Junium, C. K., Diefendorf, A. F., Freeman, K. H., Urban, N. M., and Harding, I. C., (2011). Slow release of fossil carbon during the Palaeocene-Eocene Thermal Maximum. *Nature Geoscience* 4, 481-485.

Cui, H., Kaufman, A.J., Xiao, S.H., Zhou, C.M. and Liu, X.M. (2017) Was the Ediacaran Shuram Excursion a globally synchronized early diagenetic event? Insights from methane-derived authigenic carbonates in the uppermost Doushantuo Formation, South China. *Chem Geol* 450, 59-80.

Dale, A. W., Regnier, P. and Van Cappellen, P. (2006) Bioenergetic controls on anaerobic oxidation of methane (AOM) in coastal marine sediments: A theoretical analysis. *Am J Sci* 306, 246-294.

Dale, A.W., Regnier, P., Knab, N.J., Jorgensen, B.B. and Van Cappellen, P. (2008) Anaerobic oxidation of methane (AOM) in marine sediments from the Skagerrak (Denmark): II. Reaction-transport modeling. *Geochim Cosmochim Acta* 72, 2880-2894.

Davis, C.V., Rivest, E.B., Hill, T.M., Gaylord, B., Russell, A.D. and Sanford, E. (2017) Ocean acidification compromises a planktic calcifier with implications for global carbon cycling. *Scientific Reports* 7.

DePaolo, D.J. (2011) Surface kinetic model for isotopic and trace element fractionation during precipitation of calcite from aqueous solutions. *Geochim Cosmochim Acta* 75, 1039-1056.

Dickens, G.R., Castillo, M.M. and Walker, J.C.G. (1997) A blast of gas in the latest Paleocene: Simulating first-order effects of massive dissociation of oceanic methane hydrate. *Geology* 25, 259-262.

Dickson, A.J., Cohen, A.S. and Coe, A.L. (2012) Seawater oxygenation during the Paleocene-Eocene Thermal Maximum. *Geology* 40, 639-642.

Druhan, J.L., Steefel, C.I., Williams, K.H. and DePaolo, D.J. (2013) Calcium isotope fractionation in groundwater: Molecular scale processes influencing field scale behavior. *Geochim Cosmochim Acta* 119, 93-116.

Du Vivier, A. D. C., Jacobson, A. D., Lehn, G. O., Selby, D., Hurtgen, M. T., and Sageman, B. B., (2015). Ca isotope stratigraphy across the Cenomanian-Turonian OAE 2: Links between volcanism, seawater geochemistry, and the carbonate fractionation factor. *Earth Planet Sci Lett* 416, 121-131, http://dx.doi.org/10.1016/j.epsl.2015.02.001.

Dyer, B., Higgins, J. A. and Maloof, A. C. (2017) A probabilistic analysis of meteorically altered $\delta^{13}C$ chemostratigraphy from late Paleozoic ice age carbonate platforms. *Geology* 45, 135-138, doi:110.1130/G38513.38511.

Erez, J. (2003) The Source of Ions for Biomineralization in Foraminifera and Their Implications for Paleoceanographic Proxies, in: Dove, P.M., De Yoreo, J., Weiner, S. (Eds.), Biomineralization. Mineralogical Society of America, Washington, D.C., pp. 115-149.

Fantle, M. S. and DePaolo, D. J., (2007). Ca isotopes in carbonate sediment and pore fluid from ODP Site 807A: The Ca^{2+}(aq)-calcite equilibrium fractionation factor and calcite recrystallization rates in Pleistocene sediments. *Geochim Cosmochim Acta* 71, 2524-2546.

Fantle, M. S., Maher, K. M., and DePaolo, D. J., (2010). Isotopic Approaches for Quantifying the Rates of Marine Burial Diagenesis. *Reviews of Geophysics* 48, RG3002, doi:10.1029/2009RG000306

Fantle, M.S. (2010) Evaluating the Ca isotope proxy. *Am J Sci* 310, 194-230, doi 110.2475/2403.2010.2403.

Fantle, M. S. and Higgins, J. A., (2014). The effects of diagenesis and dolomitization on Ca and Mg isotopes in marine platform carbonates: Implications for the geochemical cycles of Ca and Mg. *Geochim Cosmochim Acta* 142, 458-481, doi: 10.1016/j.gca.2014.07.025.

Fantle, M. S. and Tipper, E. T., (2014). Calcium isotopes in the global biogeochemical Ca cycle: Implications for development of a Ca isotope proxy. *Earth Science Reviews* 129, http://dx.doi.org/10.1016/j.earscirev.2013.10.004, 148-177.

Fantle, M. S., (2015). Calcium isotopic evidence for rapid recrystallization of bulk marine carbonates and implications for geochemical proxies. *Geochim Cosmochim Acta* 148, 378-401.

Fantle, M. S., Barnes, B. D., and Lau, K. V. 2020. The Role of Diagenesis in Shaping the Geochemistry of the Marine Carbonate Record. *Annu. Rev. Earth Planet. Sci.* 48: *in press*, doi:10.1146/annurev-earth-073019-060021.

Gibbs, S.J., Bown, P.R., Ridgwell, A., Young, J.R., Poulton, A.J. and O'Dea, S.A. (2016) Ocean warming, not acidification, controlled coccolithophore response during past greenhouse climate change. *Geology* 44, 59-62.

Glombitza, C., Jaussi, M., Røy, H., Seidenkrantz, M. S., Lomstein, B. A. and Jørgensen, B. B. (2015) Formate, acetate, and propionate as substrates for sulfate reduction in sub-arctic sediments of Southwest Greenland. *Frontiers in Microbiology* 6.

Gorski, C.A. and Fantle, M.S. (2017) Stable mineral recrystallization in low temperature aqueous systems: A critical review. *Geochim Cosmochim Acta* 198, 439-465, doi: 410.1016/j.gca.2016.1011.1013.

Griffith, E.M., Paytan, A., Kozdon, R., Eisenhauer, A. and Ravelo, A.C. (2008) Influences on the fractionation of calcium isotopes in planktonic foraminifera. *Earth Planet Sci Lett* 268, 124-136.

Griffith, E. M., Fantle, M. S., Eisenhauer, A., Paytan, A., and Bullen, T. (2015). Effects of ocean acidification on the marine calcium isotope record at the Paleocene–Eocene Thermal Maximum. *Earth Planet Sci Lett* 419, 81-92, http://dx.doi.org/10.1016/j.epsl.2015.03.010.

Gruber, N. (2011) Warming up, turning sour, losing breath: ocean biogeochemistry under global change. *Philosophical Transactions of the Royal Society A* 369, 1980-1996.

Gussone, N., Eisenhauer, A., Heuser, A., Dietzel, M., Bock, B., Böhm, F., Spero, H.J., Lea, D.W., Bijma, J. and Nagler, T.F. (2003) Model for kinetic effects on calcium isotope fractionation (δ^{44}Ca) in inorganic aragonite and cultured planktonic foraminifera. *Geochim Cosmochim Acta* 67, 1375-1382.

Gussone, N., Böhm, F., Eisenhauer, A., Dietzel, M., Heuser, A., Teichert, B.M.A., Reitner, J., Worheide, G. and Dullo, W.C. (2005) Calcium isotope fractionation in calcite and aragonite. *Geochim Cosmochim Acta* 69, 4485-4494.

Gutjahr, M., A. Ridgwell, A., Sexton, P.F, Anagnostou, E., Pearson, P.N., Pälike, H., Norris, R.D., Thomas, E., and Foster, G.L. (2017) Very large release of mostly volcanic carbon during the Paleocene-Eocene Thermal Maximum Paleocene-Eocene Thermal Maximum, *Nature* 548, doi:10.1038/nature23646

Halverson, G.P., Hoffman, P.F., Schrag, D.P. and Kaufman, A.J. (2002) A major perturbation of the carbon cycle before the Ghaub glaciation (Neoproterozoic) in Namibia: Prelude to snowball Earth? *Geochem Geophys Geosys* 3.

Higgins, J.A., Blattler, C.L., Lundstrom, E.A., Santiago-Ramos, D.P., Akhtar, A.A., Ahm, A.S.C., Bialik, O., Holmden, C., Bradbury, H., Murray, S.T. and Swart, P.K. (2018) Mineralogy, early marine diagenesis, and the chemistry of shallow-water carbonate sediments. *Geochim Cosmochim Acta* 220, 512-534.

Hinojosa, J. L., Brown, S. T., Chen, J., DePaolo, D. J., Paytan, A., Shen, S. Z., and Payne, J. L., (2012). Evidence for end-Permian ocean acidification from calcium isotopes in biogenic apatite. *Geology* 40, 743-746.

Holmden, C., Papanastassiou, D. A., Blanchon, P., and Evans, S., (2012). $\delta^{44/40}$Ca variability in shallow water carbonates and the impact of submarine groundwater discharge on Ca-cycling in marine environments. *Geochimica Cosmochimica Acta* 83, 179-194, doi:10.1016/j.gca.2011.12.031.

Hönisch, B., A. Ridgwell, D.N. Schmidt, E. Thomas, S.J. Gibbs, A. Sluijs, R. Zeebe, L. Kump, R.C. Martindale, S.E. Greene, W. Kiessling, J. Ries, J.C. Zachos, D.L. Royer, S. Barker, T.M. Marchitto Jr., R. Moyer, C. Pelejero, P. Ziveri, G.L. Foster, B. Williams (2012) The Geological Record of Ocean Acidification, *Science* 335: 1058-1063.

Huber, C., Druhan, J.L. and Fantle, M.S. (2017) Perspectives on geochemical proxies: The impact of model and parameter selection on the quantification of carbonate recrystallization rates. *Geochim Cosmochim Acta* 217, doi: 10.1016/j.gca.2017.08.023, 171-192.

Hülse, D., S. Arndt, J.D. Wilson, G. Munhoven, and Ridgwell, A. (2017) Understanding the causes and consequences of past marine carbon cycling variability through models, *Earth-Science Reviews* 171, doi: 10.1016/j.earscirev.2017.06.004.

Jacobson, A. D. and Holmden, C., (2008). δ^{44}Ca evolution in a carbonate aquifer and its bearing on the equilibrium isotope fractionation factor for calcite. *Earth Planet Sci Lett* 270, 349-353.

Johnson, J. W., Oelkers, E. H. and Helgeson, H. C. (1992) SUPCRT92 - A Software Package for Calculating the Standard Molal Thermodynamic Properties of Minerals, Gases, Aqueous Species, and Reactions from 1 bar to 5000 bar and 0˚C to 1000˚C. *Comput Geosci* 18, 899-947.

Kelly, D. C., Zachos, J. C., Bralower, T. J. and Schellenberg, S. A. (2005) Enhanced terrestrial weathering/runoff and surface ocean carbonate production during the recovery stages of the Paleocene-Eocene thermal maximum. *Paleoceanography* 20, PA4023, doi:4010.1029/2005PA001163.

Kelly, D.C., Nielsen, T.M.J., McCarren, H.K., Zachos, J.C. and Rohl, U. (2010) Spatiotemporal patterns of carbonate sedimentation in the South Atlantic: Implications for carbon cycling during the Paleocene-Eocene thermal maximum. *Palaeogeogr Palaeoclimatol Palaeoecol* 293, 30-40.

Kisakürek, B., Eisenhauer, A., Böhm, F., Hathorne, E.C. and Erez, J. (2011) Controls on calcium isotope fractionation in cultured planktic foraminifera, *Globigerinoides ruber* and *Globigerinella siphonifera*. Geochim Cosmochim Acta 75, 427-443.

Komar, N. and Zeebe, R. E., (2011). Oceanic calcium changes from enhanced weathering during the Paleocene-Eocene thermal maximum: No effect on calcium-based proxies. *Paleoceanography* 26, doi:10.1029/2010PA001979.

Komar, N. and Zeebe, R. E. (2016) Calcium and calcium isotope changes during carbon cycle perturbations at the end-Permian. *Paleoceanography* 31, 115-130.

Langer, G., Geisen, M., Baumann, K.H., Klas, J., Riebesell, U., Thoms, S. and Young, J.R. (2006) Species-specific responses of calcifying algae to changing seawater carbonate chemistry. *Geochem Geophys Geosys* 7, Q09006, doi:09010.01029/02005GC001227.

Langer, G., Gussone, N., Nehrke, G., Riebesell, U., Eisenhauer, A. and Thoms, S. (2007) Calcium isotope fractionation during coccolith formation in *Emiliania huxleyi*: Independence of growth and calcification rate. Geochem Geophys Geosys 8, doi:10.1029/2006GC001422.

Larowe, D. E. and Van Cappellen, P. (2011) Degradation of natural organic matter: A thermodynamic analysis. *Geochim Cosmochim Acta* 75, 2030-2042.

Lau, K.V., Maher, K., Brown, S.T., Jost, A.B., Altiner, D., DePaolo, D.J., Eisenhauer, A., Kelley, B.M., Lehrmann, D.J., Paytan, A., Yu, M., Silva-Tamayo, J.C. and Payne, J.L. (2017) The influence of seawater carbonate chemistry, mineralogy, and diagenesis on calcium isotope variations in Lower-Middle Triassic carbonate rocks. Chem Geol 471, 13-37.

Lord, N.S., A. Ridgwell, M.C. Thorne, and D.J. Lunt (2016) An impulse response function for the 'long tail' of excess atmospheric CO_2 in an Earth system model, *Global Biogeochemical Cycles*, doi: 10.1002/2014GB005074.

Lovley, D. R. and Klug, M. J. (1986) Model for the Distribution of Sulfate Reduction and Methanogenesis in Fresh-Water Sediments. *Geochim Cosmochim Acta* 50, 11-18.

McInerney, F.A. and Wing, S.L. (2011) The Paleocene-Eocene Thermal Maximum: A Perturbation of Carbon Cycle, Climate, and Biosphere with Implications for the Future. Annu Rev Earth Planet Sci 39, 10.1146/annurev-earth-040610-133431, 489-516.

Manno, C., Morata, N. and Bellerby, R. (2012) Effect of ocean acidification and temperature increase on the planktonic foraminifer *Neogloboquadrina pachyderma* (sinistral). *Polar Biology* 35, 1311-1319.

Meyers, S.R., Sageman, B.B. and Hinnov, L.A. (2001) Integrated quantitative stratigraphy of the Cenomanian-Turonian bridge creek limestone member using evolutive harmonic analysis and stratigraphic modeling. *J Sediment Res* 71, 628-644.

Mejia, L.M., Paytan, A., Eisenhauer, A., Bohm, F., Kolevica, A., Bolton, C., Mendez-Vicente, A., Abrevaya, L., Isensee, K. and Stoll, H. (2018) Controls over $\delta^{44/40}$Ca and Sr/Ca variations in coccoliths: New perspectives from laboratory cultures and cellular models. *Earth Planet Sci Lett* 481, 48-60.

Nicolo, M.J., Dickens, G.R. and Hollis, C.J. (2010) South Pacific intermediate water oxygen depletion at the onset of the Paleocene-Eocene thermal maximum as depicted in New Zealand margin sections. *Paleoceanography* 25.

Pagani, M., Pedentchouk, N., Huber, M., Sluijs, A., Schouten, S., Brinkhuis, H., Sinninghe Damste, J.S., Dickens, G., Backman, J., Clemens, S., Cronin, T., Eynaud, F., Gattacceca, J., Jakobsson, M., Jordan, R., Kaminski, M., King, J., Koc, N., Martinez, N., McInroy, D., Moore Jr., T.C., O'Regan, M., Onodera, J., Pälike, H., Rea, B., Rio, D., Sakamoto, T., Smith, D.C., St John, K.E.K., Suto, I., Suzuki, N., Takahashi, K., Watanabe, M. and Yamamoto, M. (2006) Arctic hydrology during global warming at the Palaeocene/Eocene thermal maximum. *Nature* 442, 671-675.

Payne, J. L., Turchyn, A. V., Paytan, A., DePaolo, D. J., Lehrmann, D. J., Yu, M. Y., and Wei, J. Y., (2010). Calcium isotope constraints on the end-Permian mass extinction. *Proc Natl Acad Sci USA* 107, 8543-8548.

Penman, D.E., Turner, S.K., Sexton, P.F., Norris, R.D., Dickson, A.J., Boulila, S., Ridgwell, A., Zeebe, R.E., Zachos, J.C., Cameron, A., Westerhold, T. and Rohl, U. (2016) An abyssal carbonate compensation depth overshoot in the aftermath of the Palaeocene-Eocene Thermal Maximum. *Nature Geoscience* 9, 575-581, doi:510.1038/ngeo2757.

Richter, F.M. and DePaolo, D.J. (1987) Numerical models for diagenesis and the Neogene Sr isotopic evolution of seawater from DSDP Site 590B. *Earth Planet Sci Lett* 83, 27-38.

Richter, F.M. and DePaolo, D.J. (1988) Diagenesis and Sr isotopic evolution of seawater using data from DSDP-590B and DSDP-575. *Earth Planet Sci Lett* 90, 382-394.

Richter, F.M. and Liang, Y. (1993) The Rate and Consequences of Sr Diagenesis in Deep-Sea Carbonates. *Earth Planet Sci Lett* 117, 553-565.

Ridgwell, A., Hargreaves, J.C., Edwards, N.R., Annan, J.D., Lenton, T.M., Marsh, R., Yool, A. and Watson, A. (2007a) Marine geochemical data assimilation in an efficient Earth System Model of global biogeochemical cycling. *Biogeosciences* 4, 87-104.

Ridgwell, A., Zondervan, I., Hargreaves, J., Bijma, J., and Lenton, T. (2007b) Assessing the potential long-term increase of oceanic fossil fuel CO_2 uptake due to 'CO_2-calcification feedback', *Biogeosciences* 4, 481-492.

Riebesell, U., Zondervan, I., Rost, B., Tortell, P.D., Zeebe, R.E. and Morel, F.M.M. (2000) Reduced calcification of marine plankton in response to increased atmospheric CO_2. *Nature* 407, 364-367.

Rittmann, B. E. and McCarty, P. L. (2001) Environmental Biotechnology: Principles and Applications. McGraw-Hill, New York.

Rohl, U., Westerhold, T., Bralower, T. J. and Zachos, J. C. (2007) On the duration of the Paleocene-Eocene thermal maximum (PETM). *Geochem Geophys Geosys* 8, doi:10.1029/2007GC001784.

Sageman, B.B., Meyers, S.R. and Arthur, M.A. (2006) Orbital time scale and new C-isotope record for Cenomanian-Turonian boundary stratotype. *Geology* 34, 125-128.

Schrag, D.P., Higgins, J.A., Macdonald, F.A. and Johnston, D.T. (2013) Authigenic Carbonate and the History of the Global Carbon Cycle. *Science* 339, 540-543.

Schulte, P., Scheibner, C. and Speijer, R.P. (2011) Fluvial discharge and sea-level changes controlling black shale deposition during the Paleocene-Eocene Thermal Maximum in the Dababiya Quarry section, Egypt. *Chem Geol* 285, 167-183.

Sime, N. G., De La Rocha, C. L., Tipper, E. T., Tripati, A., Galy, A. and Bickle, M. J. (2007) Interpreting the Ca isotope record of marine biogenic carbonates. *Geochim Cosmochim Acta* 71, 3979-3989.

Sluijs, A., Schouten, S., Pagani, M., Woltering, M., Brinkhuis, H., Sinninghe Damsté, J.S., Dickens, G.R., Huber, M., Reichart, G.-J., Stein, R., Matthiessen, J., Lourens, L.J., Pedentchouk, N., Backman, J., Moran, K. and Scientists, t.E. (2006) Subtropical Arctic Ocean temperatures during the Palaeocene/Eocene thermal maximum. *Nature* 441, 610-613.

Sluijs, A., Rohl, U., Schouten, S., Brumsack, H.J., Sangiorgi, F., Damste, J.S.S. and Brinkhuis, H. (2008) Arctic late Paleocene-early Eocene paleoenvironments with special emphasis on the Paleocene-Eocene thermal maximum (Lomonosov Ridge, Integrated Ocean Drilling Program Expedition 302). *Paleoceanography* 23.

Soetaert, K., Hofmann, A.F., Middelburg, J.J., Meysman, F.J.R. and Greenwood, J. (2007) The effect of biogeochemical processes on pH. *Mar Chem* 105, 30-51.

Steefel, C.I., Druhan, J.L. and Maher, K. (2014) Modeling Coupled Chemical and Isotopic Equilibration Rates. *Procedia Earth and Planetary Science* 10, 208-217.

Swart, P.K. and Eberli, G. (2005) The nature of the $\delta^{13}C$ of periplatform sediments: Implications for stratigraphy and the global carbon cycle. *Sediment Geol* 175, 115-129.

Swart, P.K. (2008) Global synchronous changes in the carbon isotopic composition of carbonate sediments unrelated to changes in the global carbon cycle. *Proc Natl Acad Sci USA* 105, 13741-13745.

Swart, P.K. and Kennedy, M.J. (2012) Does the global stratigraphic reproducibility of $\delta^{13}C$ in Neoproterozoic carbonates require a marine origin? A Pliocene-Pleistocene comparison. *Geology* 40, 87-90.

Swart, P.K. (2015) The geochemistry of carbonate diagenesis: The past, present and future. *Sedimentology* 62, 1233-1304.

Tang, J. W., Dietzel, M., Böhm, F., Kohler, S. J. and Eisenhauer, A. (2008) Sr^{2+}/Ca^{2+} and $^{44}Ca/^{40}Ca$ fractionation during inorganic calcite formation: II. Ca isotopes. *Geochim Cosmochim Acta* 72, 3733-3745.

Tang, J. W., Niedermayr, A., Kohler, S. J., Böhm, F., Kisakürek, B., Eisenhauer, A. and Dietzel, M. (2012) Sr^{2+}/Ca^{2+} and $^{44}Ca/^{40}Ca$ fractionation during inorganic calcite formation: III. Impact of salinity/ionic strength. *Geochim Cosmochim Acta* 77, 432-443.

Turchyn, A.V. and DePaolo, D.J. (2011) Calcium isotope evidence for suppression of carbonate dissolution in carbonate-bearing organic-rich sediments. *Geochim Cosmochim Acta* 75, 7081-7098.

Wang, J.Y., Jacobson, A.D., Zhang, H., Ramezani, J., Sageman, B.B., Hurtgen, M.T., Bowring, S.A. and Shen, S.Z. (2019) Coupled $\delta^{44/40}Ca$, $\delta^{88/86}Sr$, and $^{87}S/^{86}Sr$ geochemistry across the end-Permian mass extinction event. *Geochim Cosmochim Acta* 262, 143-165.

Weller, P. and Stein, R. (2008) Paleogene biomarker records from the central Arctic Ocean (Integrated Ocean Drilling Program Expedition 302): Organic carbon sources, anoxia, and sea surface temperature. *Paleoceanography* 23, PA1S17, doi:10.1029/2007PA001472.

Westerhold, T., Rohl, U. and Laskar, J. (2012) Time scale controversy: Accurate orbital calibration of the early Paleogene. *Geochem Geophys Geosys* 13, Q06015, doi:10.1029/2012GC004096.

Wieczorek, R., Fantle, M.S., Kump, L.R. and Ravizza, G. (2013) Geochemical evidence for volcanic activity prior to and enhanced terrestrial weathering during the Paleocene Eocene Thermal Maximum. *Geochim Cosmochim Acta* 119, 391-410.

Winfrey, M.R. and Ward, D.M. (1983) Substrates for Sulfate Reduction and Methane Production in Intertidal Sediments. *Appl Environ Microbiol* 45, 193-199.

Yao, W.Q., Paytan, A. and Wortmann, U.G. (2018) Large-scale ocean deoxygenation during the Paleocene-Eocene Thermal Maximum. *Science* 361, 804-806

Zachos, J. C., Rohl, U., Schellenberg, S. A., Sluijs, A., Hodell, D. A., Kelly, D. C., Thomas, E., Nicolo, M., Raffi, I., Lourens, L. J., McCarren, H., and Kroon, D., (2005). Rapid acidification of the ocean during the Paleocene-Eocene thermal maximum. *Science* 308, 1611-1615.

Zeebe, R. E., Zachos, J. C., and Dickens, G. R., (2009). Carbon dioxide forcing alone insufficient to explain Palaeocene-Eocene Thermal Maximum warming. *Nature Geoscience* 2, 576-580.

Zeebe, R. E. and Zachos, J. C., (2013). Long-term legacy of massive carbon input to the Earth system: Anthropocene versus Eocene. *Philosophical Transactions of the Royal Society A-Mathematical Physical and Engineering Sciences* 371, 2012006, doi:10.1098/rsta.2012.0006.

Zhou, X., Thomas, E., Winguth, A.M.E., Ridgwell, A., Scher, H., Hoogakker, B.A.A., Rickaby, R.E.M. and Lu, Z. (2016) Expanded oxygen minimum zones during the late Paleocene-early Eocene: Hints from multiproxy comparison and ocean modeling. *Paleoceanography* 31, 1532-1546.

Zuddas, P. and Mucci, A. (1998) Kinetics of calcite precipitation from seawater: II. The influence of the ionic strength. *Geochim Cosmochim Acta* 62, 757-766.

Figure captions

Figure 1 — (a) Calcium carbonate content (wt. %) and (b) Ca isotopic composition ($\delta^{44}Ca$; ‰) of bulk carbonate sediments and marine barite from ODP Sites 1212 and 1221 (Griffith et al., 2015). In (b), both the seawater and SRM-915a scales are shown for completeness. All records are shown on relative depth scales, relative to the carbon isotope excursion (CIE) indicated by carbonate $\delta^{13}C$ (‰). Error bars (external reproducibility) are not included, for clarity, but vary between 0.05 and 0.3‰ (see Griffith et al., 2015).

Figure 2 — Calcium isotopic composition ($\delta^{44}Ca$; ‰) of bulk sediment due to mixing between biogenic marine and authigenic endmembers, as a function of % initial pore space filled. Shaded areas indicate a range in initial carbonate content of the sediment between 50 and 100 wt. %. Also shown are mixing envelopes that vary as a function of the initial porosity (ϕ) of the bulk sediment. The authigenic endmember is assumed to have a constant $\delta^{44}Ca$ value of 1.9‰, which is the modern seawater value (e.g., Fantle and Tipper, 2014). In reality, the $\delta^{44}Ca$ of the authigenic endmember will vary based on where in the sedimentary section it forms.

Figure 3 — Effect of authigenic carbonate addition on bulk sediment $\delta^{44}Ca$ and weight percent (wt. %) $CaCO_3$. Mixing curves are shown in each panel as solid lines with tick marks; tick marks indicate discrete points at which mixing calculations were performed (see SI for calculation details). Each curve follows the trajectory of mixing for a sediment with an initial $CaCO_3$ content and $\delta^{44}Ca$, porosity, and the $\delta^{44}Ca$ of the endmember authigenic phase ($\delta^{44}Ca$ = 1.9‰). Tick marks reflect the percentage of pore space filled (select values noted by tick mark labels; also included in parentheses are select values for wt. % $CaCO_3$); ticks marks are arbitrarily spaced in order to capture the shapes of the mixing trends (esp. at low initial % $CaCO_3$) but the spacing is consistent between mixing curves. (a) Bulk nannofossil oozes (ODP Sites 1212 and 1221) plotted as blue and green circles, respectively. Site 1262 cGENIE sedcore output (curves in red/green; blue/orange) shown for PETM-specific carbon flux scenarios (Gutjahr et al., 2017; Gibbs et al., 2016), respectively, and the two Ca isotopic fractionation factor-water chemistry relationships, described in the text. The cGENIE output has different delta values due to differences in the initial, pre-event steady state for each C flux scenario. In (b), blue and green curves indicate CrunchTope simulations described in the text; dashed lines indicate the effects of numerical mixing on the solid (see SI Section S2 for details). The green curve indicates "1221-like" conditions (k=$5 \cdot 10^{-11}$ mol/m^2/s; sedimentation rate=10 m/Ma), while the blue curve indicates "1212-like" conditions (k=$1 \cdot 10^{-11}$ mol/m^2/s; sedimentation rate=10 m/Ma). In (b), arrows indicate the initial lithology at the seawater-sediment interface (i.e., the upper 11 and 25 cm at Sites 1212 and 1221, respectively) at the beginning of the simulations and the primary burial lithologies assumed in the 1212- and 1221-like simulations (see Tables S1 and S2 for additional reactive transport modeling details).

Figure 4 — cGENIE sedcore model output for three carbon flux scenarios: (a) Gutjahr et al. (2017), (b) Cui et al. (2011), and (c) Gibbs et al. (2016). All temperatures, alkalinities, and aqueous concentrations, including the relative saturation state $\left(\Omega_{calcite}(t)/\Omega_{calcite}(t_o)\right)$, are those of bottom water at a given site. The weight percent $CaCO_3$ is the concentration of calcite that is buried. Thirty-five sites spanning the global ocean, indicated by each of the colored curves, are plotted; the locations of each are shown in Fig. S1.

Figure 5 — cGENIE sedcore model output for the Gibbs et al. (2016) scenario at grid location 1607 (ODP Site 1262). The weight % $CaCO_3$, carbonate $\delta^{44}Ca$ (‰), and carbonate $\delta^{13}C$ (‰) are shown.

Figure 6 — CrunchTope model output for calcite saturation state over the three-step overshoot perturbation detailed in Table S2. The two sets of curves refer to different rate constants assumed for calcite precipitation, which vary by a factor of ten in this example. Both the initial and burial porosity are assumed to be 0.75 in the simulations shown.

Figure 7 — Site 1221-like and Site 1212-like CrunchTope simulations over a PETM-like overshoot (see SI for details of simulation boundary conditions). In the simulations, precipitation is permitted but neither bulk mineral dissolution nor recrystallization are permitted. Site 1221-like: (a) schematic of initial sedimentary system (i.e., prior to alkalinity overshoot initiated at upper boundary) and burial lithology during overshoot (arrow), (b) $\delta^{44}Ca$ of bulk solid and pore fluid, (c) % $CaCO_3$, and (d) comparison of results assuming a range of rate constants and a burial rate of 25 m/Ma instead of 10 m/Ma. Site 1221-like: (e) schematic of initial sedimentary system (i.e., prior to alkalinity overshoot) and burial lithology during overshoot (arrow), (f) $\delta^{44}Ca$ of bulk solid and pore fluid, and (g) % $CaCO_3$. (h) Secular variability in calcite saturation state (Ω) and pH at the upper boundary of the model domain, as constrained by the cGENIE simulations. Data points in (d) are the Site 1221 bulk carbonate $\delta^{44}Ca$ values from Griffith et al. (2015).

Figure 8 —Site 1221-like (a) $\delta^{44}Ca$, (b) % $CaCO_3$, and (c) schematic and Site 1221-like (c) $\delta^{44}Ca$, (d) % $CaCO_3$, and (f) schematic from CrunchTope simulations with bulk recrystallization enabled. Data points in (a) are the Site 1221 bulk carbonate $\delta^{44}Ca$ values from Griffith et al. (2015).

Figure 9 — cGENIE model output for three carbon flux scenarios: (a) Gutjahr et al. (2017), (b) Cui et al. (2011), and (c) Gibbs et al. (2016). For each scenario, we show the atmospheric CO_2 concentration over the event, the sedcore bottom water O_2(aq) output at a range of sites throughout the global ocean (indicated in Fig. S1), and spatial maps of relative oxygen concentration in both the 2756.6 meter mid-depth interval and a longitudinal cross-section. Relative O_2(aq) concentrations are

calculated by normalizing minimum O_2(aq) by initial O_2(aq) concentrations (i.e., at 0.5 or 10 ka, depending on the model scenario).

Figure 10 — Reactive transport simulation of acetotrophic sulfate reduction over a (a) PETM-like perturbation in which saturation state relative to calcite, pH, and aqueous oxygen concentration vary (see Table S3 for simulation details); the initial condition set in the column is indicated at t=0, while the time interval over which an initial steady state is reached is indicated by the dashed line. Plotted model output includes: (b) sulfate reduction rate (mol/kg water/year), as well as pore fluid (c) pH, (d) aqueous oxygen concentration (mol/kg water), (e) saturation state relative to calcite ($\Omega_{calcite}$), and (f) volume fraction (%) of calcite in the modeled 1-D section. The colored curves reflect the model output at the times indicated in (f); the model is first run to a steady state sulfate reduction rate over 8 ka, then perturbed to lower pH values and lower O_2(aq) concentrations in three pulses (6.5, 4.6, and 8.9 ka). The timing and bottom water chemistry of the perturbation pulses is constrained by the cGENIE model output. The vertical, red curve (~0 ka) is the initial chemistry at t=0.

Figure 11 — Mixing calculation for core data presented by Du Vivier et al. (2015) associated with OAE 2; assumptions are shown at the bottom of the panel (also see Fig. 3 caption for related details). The line labeled “environmental signal” is a catchall term that indicates any process occurring in the natural system, besides authigenesis/recrystallization. The mixing calculation was performed for 'percentage of pore space filled' in even increments, which is what the ticks marks repesent; however, because of the way mixing works in this system, the tick marks don't appear to be evenly-spaced in δ^{44}Ca-wt. % $CaCO_3$ space.

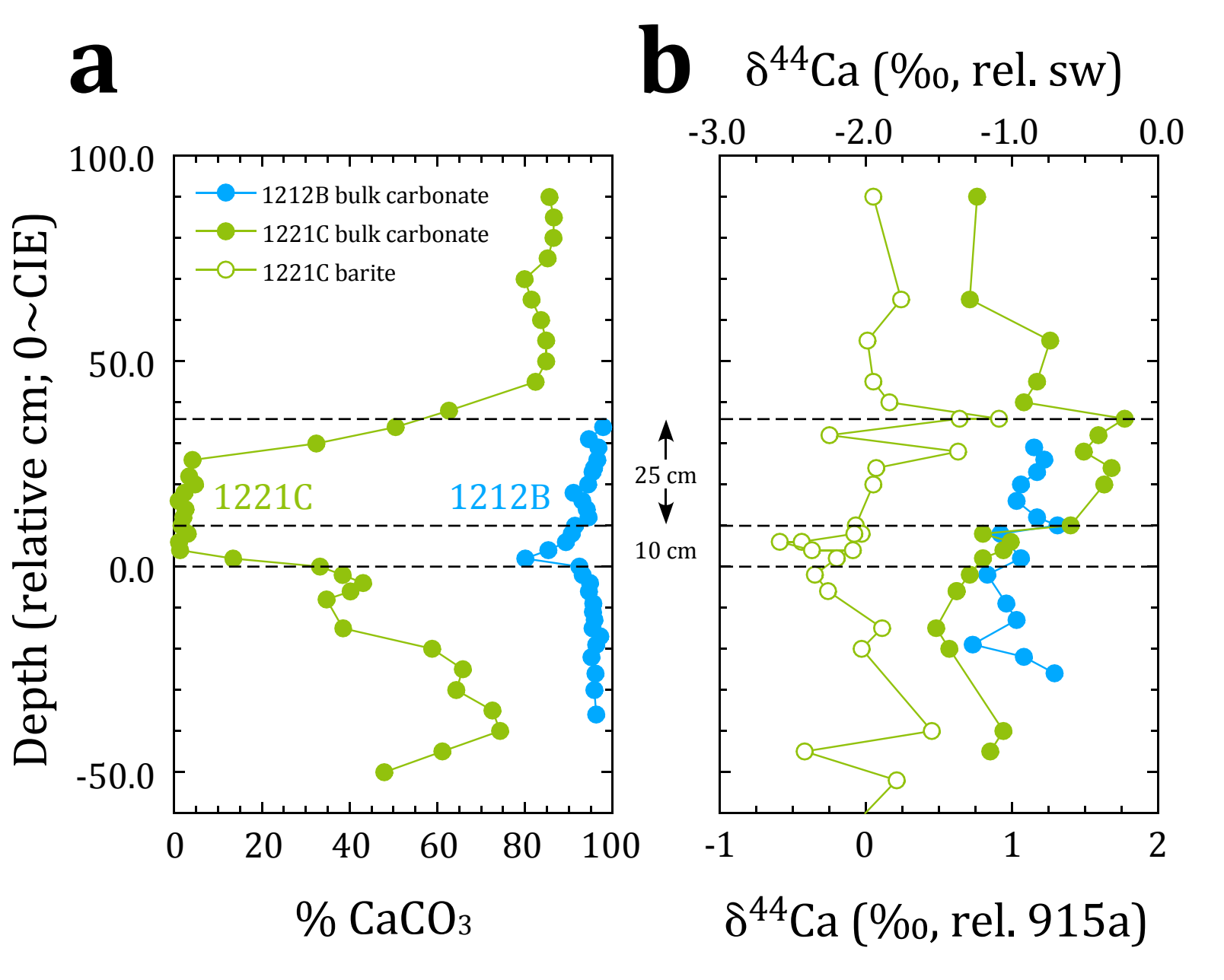
a
b
δ44Ca (‰, rel. sw)
-3.0
-2.0
-1.0
0.0
100.0
50.0
0.0
-50.0
Depth (relative cm; 0~CIE)
1212B bulk carbonate
1221C bulk carbonate
1221C barite
1221C
1212B
25 cm
10 cm
0
20
40
60
80
100
% CaCO3
-1
0
1
2
δ44Ca (‰, rel. 915a)

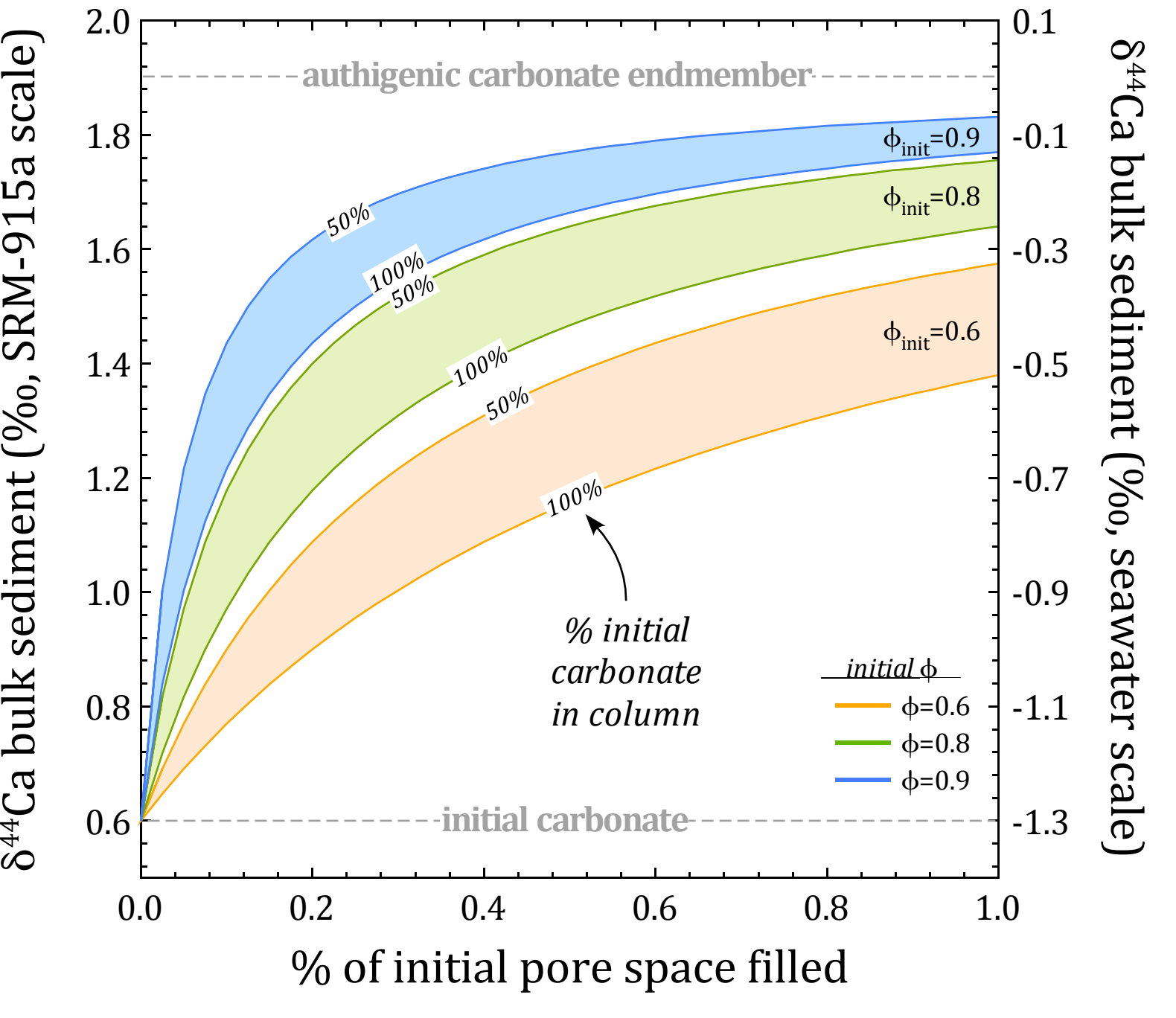
authigenic carbonate endmember
initial carbonate
ϕ_{init}=0.9
ϕ_{init}=0.8
ϕ_{init}=0.6
50%
100%
50%
100%
50%
100%
% initial carbonate in column
initial ϕ
ϕ=0.6
ϕ=0.8
ϕ=0.9
δ44Ca bulk sediment (‰, SRM-915a scale)
δ44Ca bulk sediment (‰, seawater scale)
% of initial pore space filled
2.0
1.8
1.6
1.4
1.2
1.0
0.8
0.6
0.1
-0.1
-0.3
-0.5
-0.7
-0.9
-1.1
-1.3
0.0
0.2
0.4
0.6
0.8
1.0

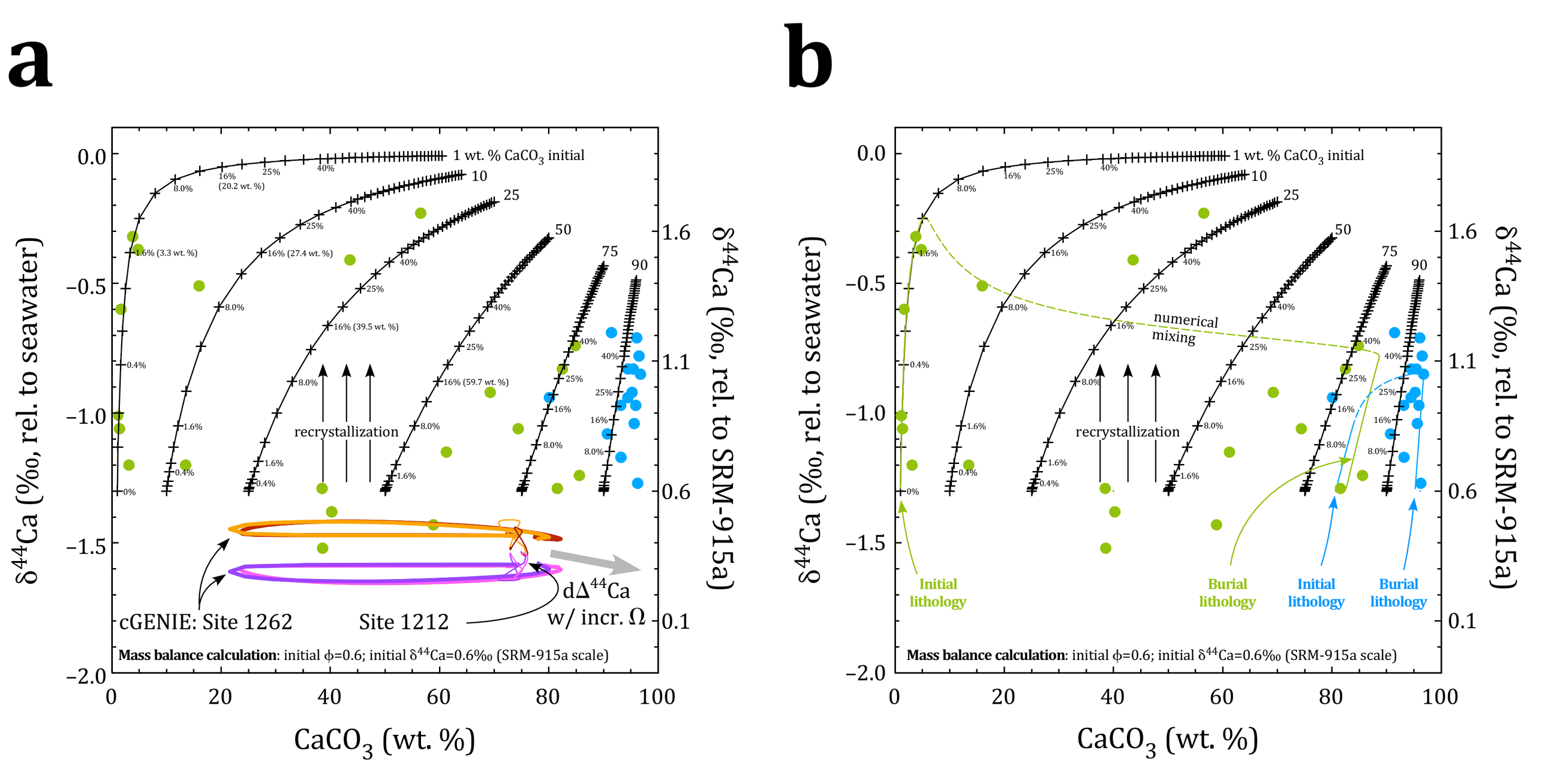
a
b
1 wt. % CaCO3 initial
10
25
50
75
90
recrystallization
numerical mixing
cGENIE: Site 1262
Site 1212
dΔ44Ca w/ incr. Ω
Initial lithology
Burial lithology
Initial lithology
Burial lithology
Mass balance calculation: initial ϕ=0.6; initial δ44Ca=0.6‰ (SRM-915a scale)
δ44Ca (‰, rel. to seawater)
δ44Ca (‰, rel. to SRM-915a)
CaCO3 (wt. %)

a

b

c

Gutjahr scenario

Cui scenario

Gibbs scenario

pCO_2 [atm]

pH

Temperature [°C]

Alkalinity (µM)

$[CO_3^{2-}]$ (µM)

$\Omega_{calcite}(t)/\Omega_{calcite}(t_0)$

$CaCO_3$ [wt %]

Time (ka)

Grid Locations [iijj]

0218 3200 m
0521 3200 m
0618 3200 m
0717 2900 m
0718 3200 m
3523 1900 m
3524 2250 m
3622 2500 m
3623 2500 m
3624 2500 m
1021 1750 m
1022 1500 m
1127 1500 m
1607 3600 m
1608 1500 m
1707 2600 m
1708 3200 m
1709 3400 m
1631 2150 m
1702 2100 m
1802 1525 m
2207 3560 m
2209 4220 m
2115 3990 m
2214 3200 m
2217 4300 m
2315 2740 m
2503 1350 m
2504 900 m
2603 1500 m
2510 3520 m
2511 3450 m
2610 4900 m
2705 4000 m
2707 3476 m

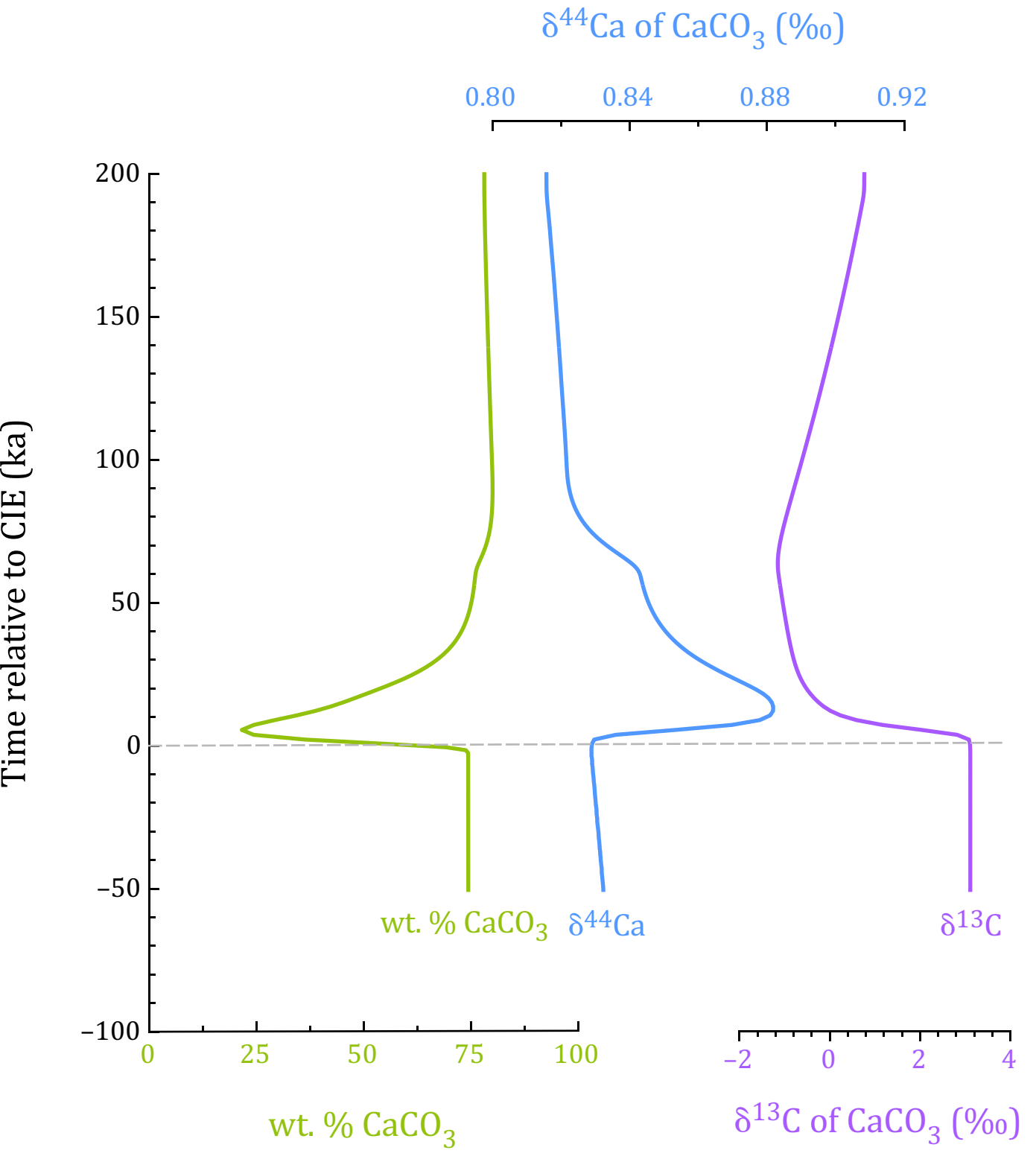
δ44Ca of CaCO3 (‰)
0.80
0.84
0.88
0.92
200
150
100
50
0
−50
−100
Time relative to CIE (ka)
wt. % CaCO3
δ44Ca
δ13C
0
25
50
75
100
wt. % CaCO3
−2
0
2
4
δ13C of CaCO3 (‰)

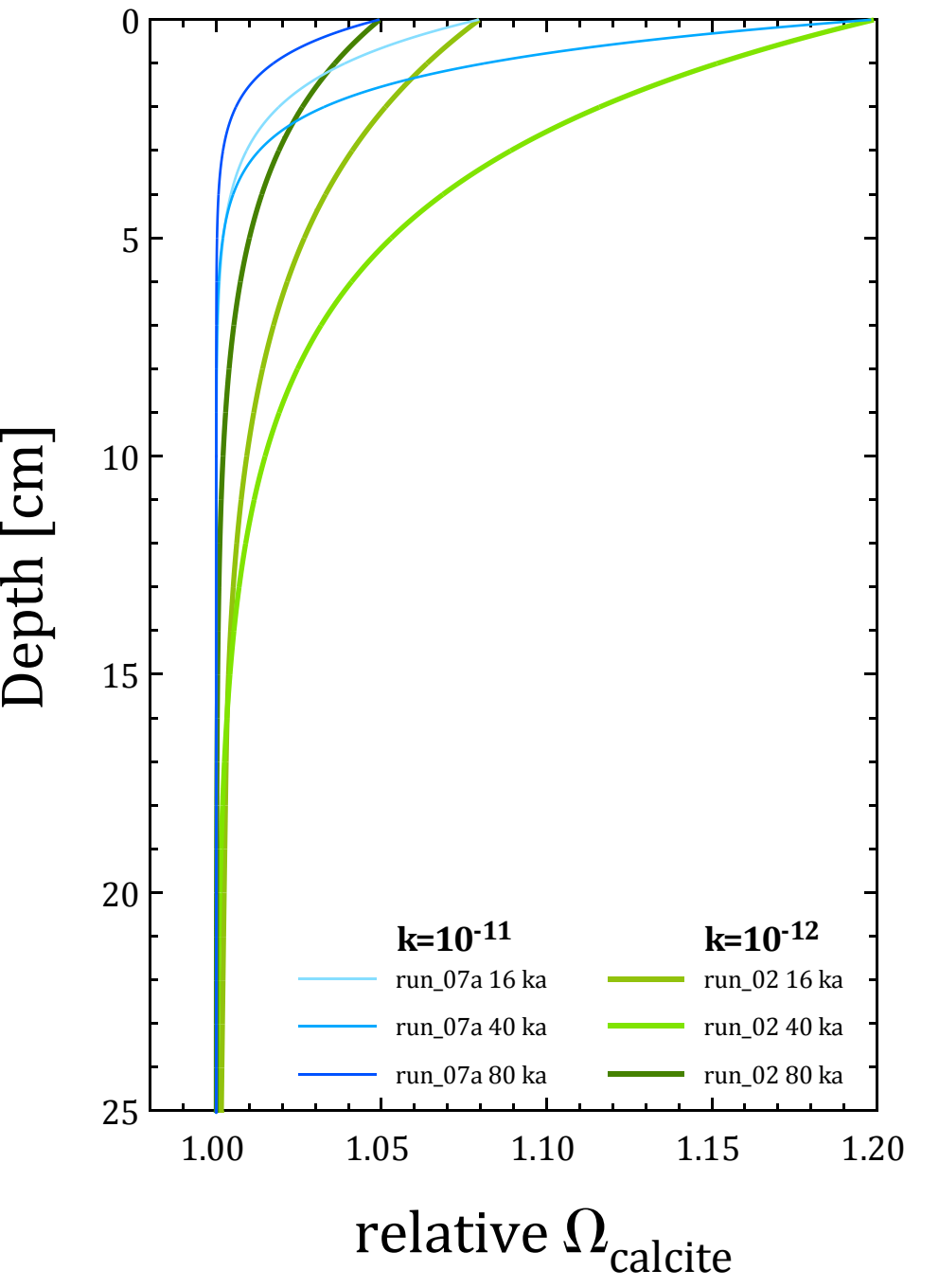
Depth [cm]
0
5
10
15
20
25
1.00
1.05
1.10
1.15
1.20
relative Ω calcite
k=10-11
run_07a 16 ka
run_07a 40 ka
run_07a 80 ka
k=10-12
run_02 16 ka
run_02 40 ka
run_02 80 ka

a

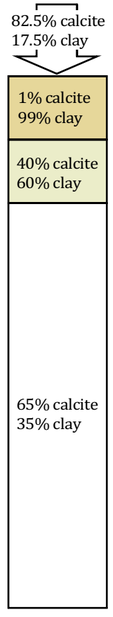
82.5% calcite
17.5% clay
1% calcite
99% clay
40% calcite
60% clay
65% calcite
35% clay

b

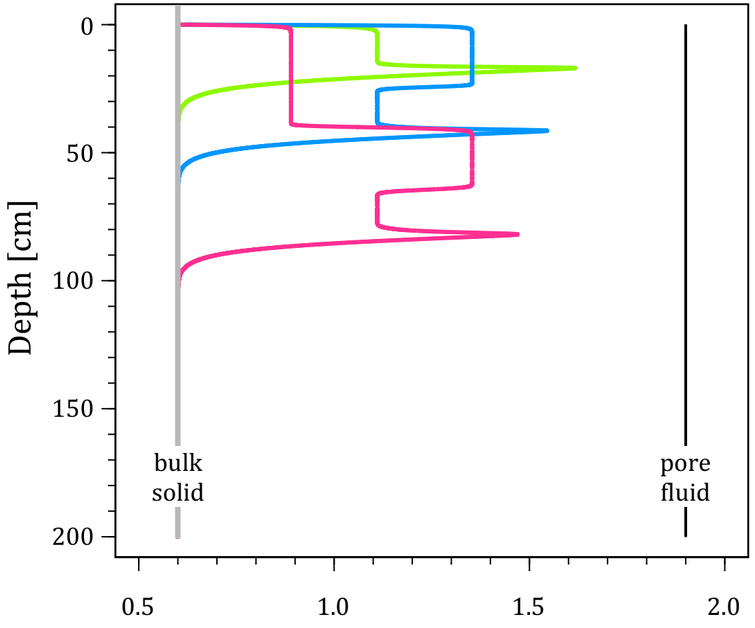
Depth [cm]
0
50
100
150
200
bulk
solid
pore
fluid
0.5
1.0
1.5
2.0

c

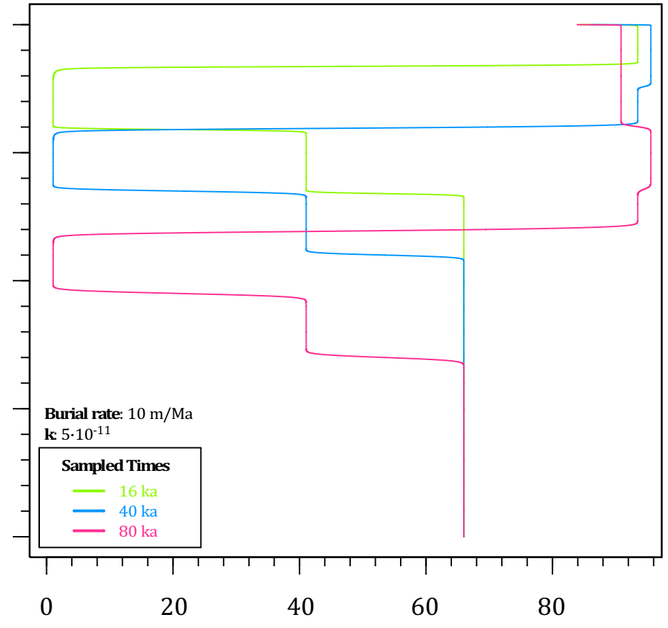
Burial rate: 10 m/Ma
k: 5·10-11
Sampled Times
16 ka
40 ka
80 ka
0
20
40
60
80

d

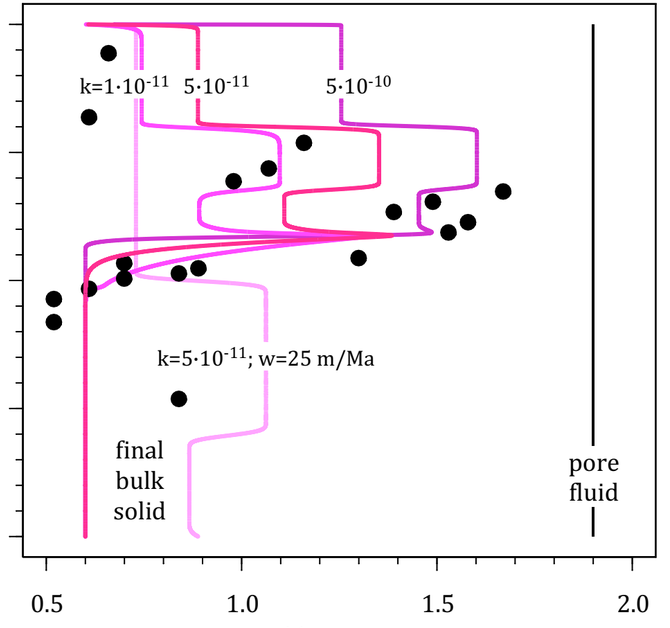
k=1·10-11
5·10-11
5·10-10
k=5·10-11; w=25 m/Ma
final
bulk
solid
pore
fluid
0.5
1.0
1.5
2.0

e

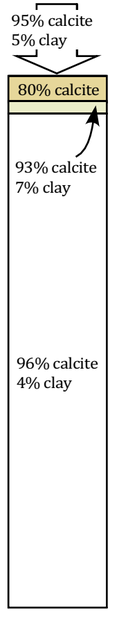
95% calcite
5% clay
80% calcite
93% calcite
7% clay
96% calcite
4% clay

f

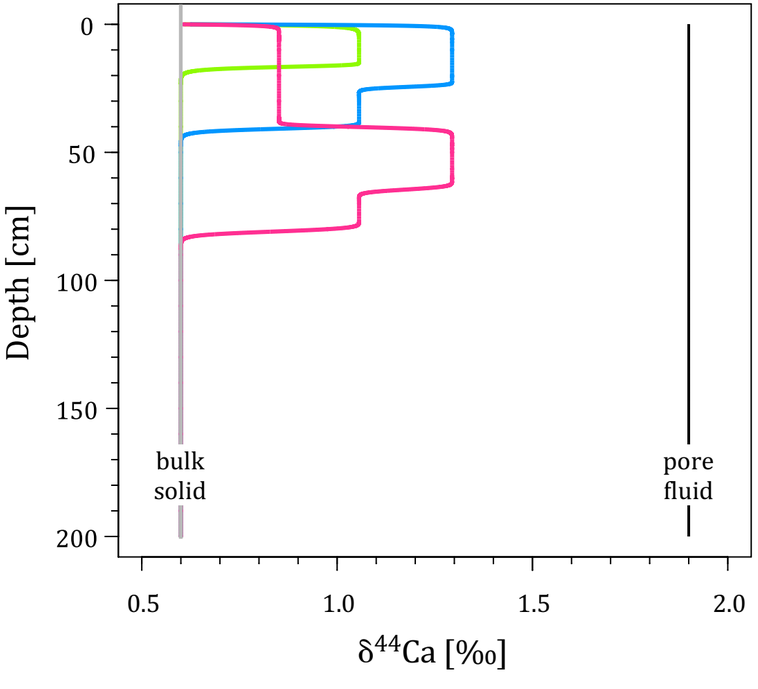
δ44Ca [‰]
Depth [cm]
0
50
100
150
200
bulk
solid
pore
fluid
0.5
1.0
1.5
2.0
δ44Ca [‰]

g

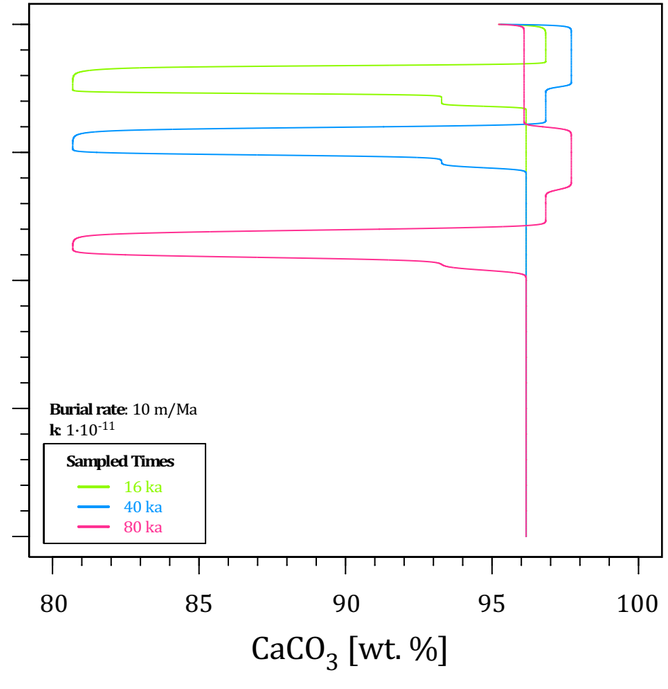
CaCO3 [wt. %]
Burial rate: 10 m/Ma
k: 1·10-11
Sampled Times
16 ka
40 ka
80 ka
80
85
90
95
100
CaCO3 [wt. %]

h

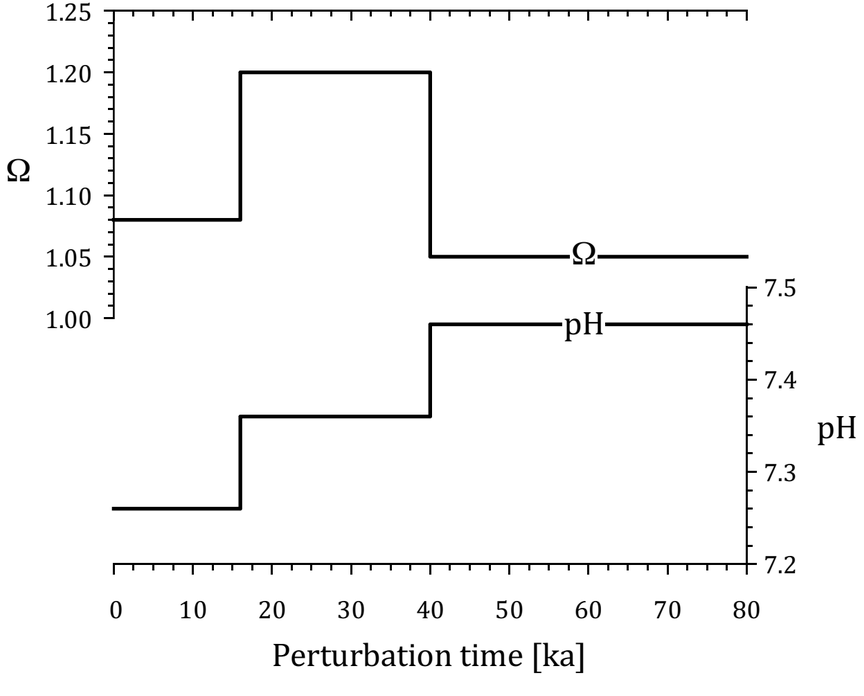
δ44Ca [‰]
Ω
1.25
1.20
1.15
1.10
1.05
1.00
Ω
pH
7.5
7.4
7.3
7.2
pH
0
10
20
30
40
50
60
70
80
Perturbation time [ka]

a
b
c
Depth [cm]
0
50
100
150
200
0.5
1.0
1.5
2.0
δ44Ca [‰]
initial solid
bulk solid
pore fluid
initial pore fluid
0
20
40
60
80
CaCO3 [wt. %]
Burial rate: 10 m/Ma
k: 10-14 mol/m2/s
Sampled Times
16 ka
40 ka
80 ka
82.5% calcite
17.5% clay
1% calcite
99% clay
40% calcite
60% clay
65% calcite
35% clay
d
e
f
95% calcite
5% clay
80% calcite
93% calcite
7% clay
96% calcite
4% clay
80
85
90
95
100

a

b

c

Gutjahr scenario

Cui scenario

Gibbs scenario

pCO_2 [atm]

$3 \cdot 10^{-3}$

$2 \cdot 10^{-3}$

$1 \cdot 10^{-3}$

0

O_2 concentration (µM)

Time (ka)

46 ka/0.5 ka: 2756.57 m mid-depth

60 ka/10 ka: 2756.57 m mid-depth

6 ka/0.5 ka: 2756.57 m mid-depth

0.3 0.4 0.5 0.6 0.7 0.8 0.9 1.0

Depth (meters)

Longitude

a

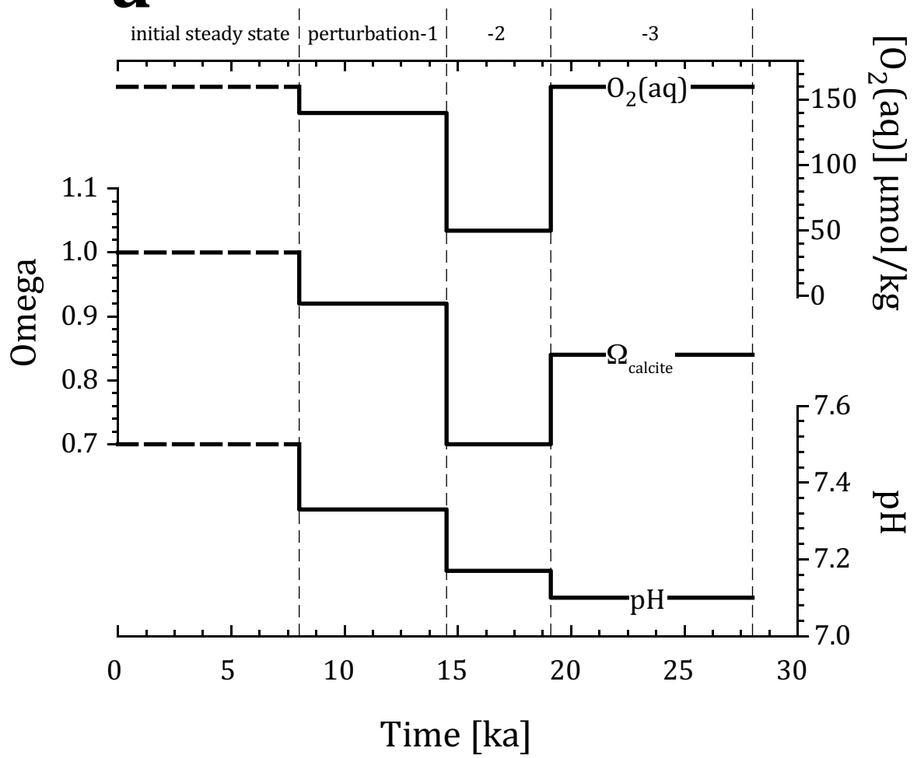
initial steady state
perturbation-1
-2
-3
O_2(aq)
$\Omega_{calcite}$
pH
Omega
1.1
1.0
0.9
0.8
0.7
150
100
50
0
O_2(aq)] µmol/kg
7.6
7.4
7.2
7.0
pH
0
5
10
15
20
25
30
Time [ka]

b

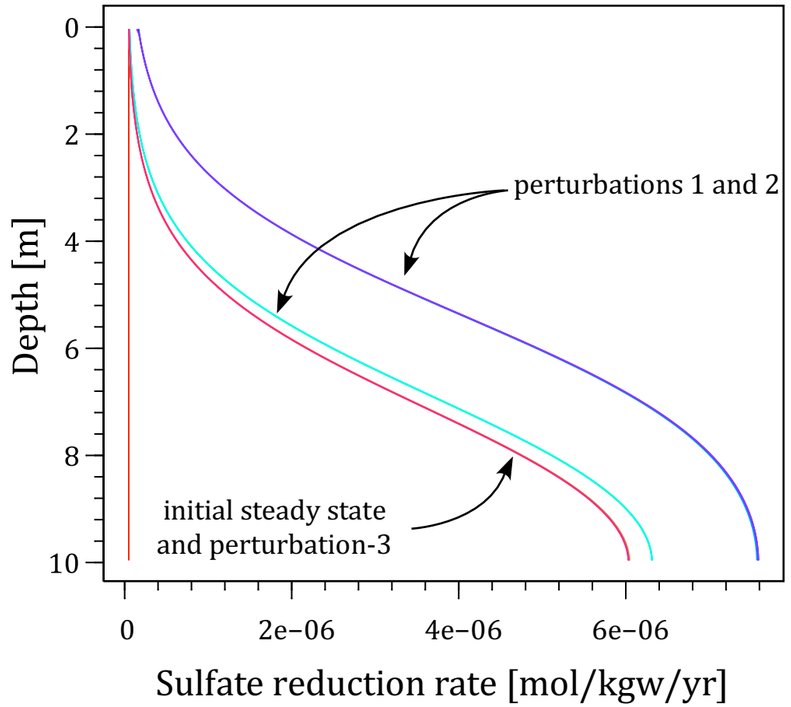
perturbations 1 and 2
initial steady state
and perturbation-3
Depth [m]
0
2
4
6
8
10
0
2e−06
4e−06
6e−06
Sulfate reduction rate [mol/kgw/yr]

c

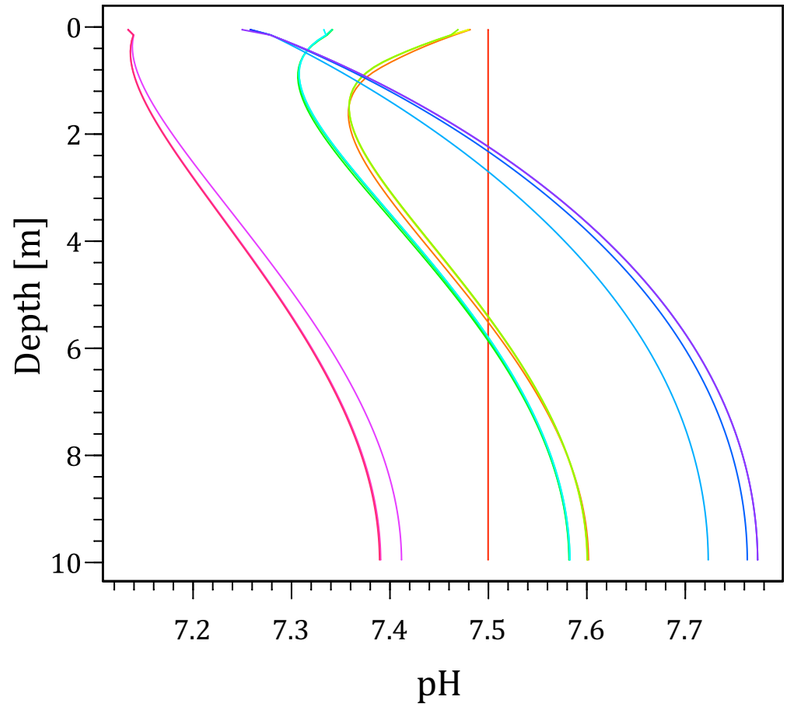
Depth [m]
0
2
4
6
8
10
7.2
7.3
7.4
7.5
7.6
7.7
pH

d

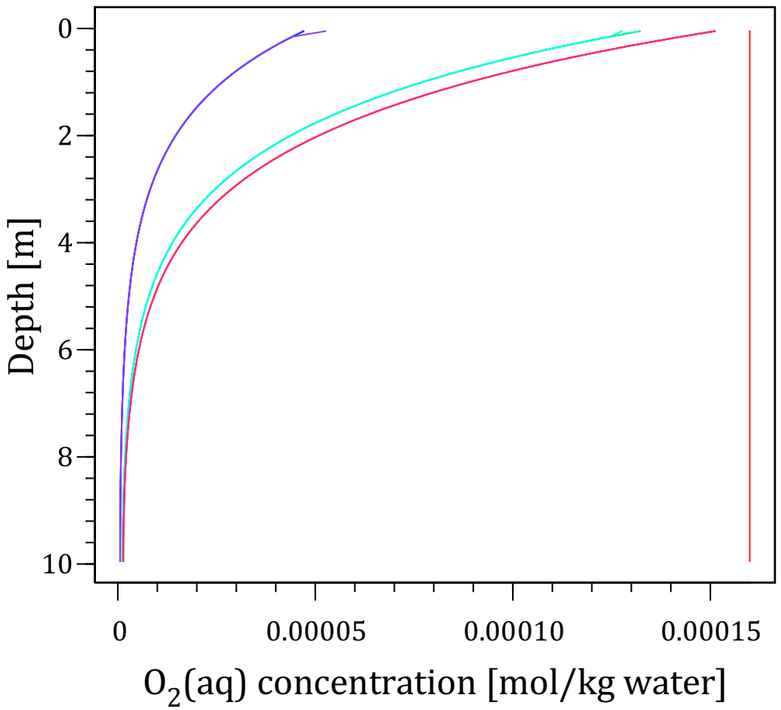
Depth [m]
0
2
4
6
8
10
0
0.00005
0.00010
0.00015
O_2(aq) concentration [mol/kg water]

e

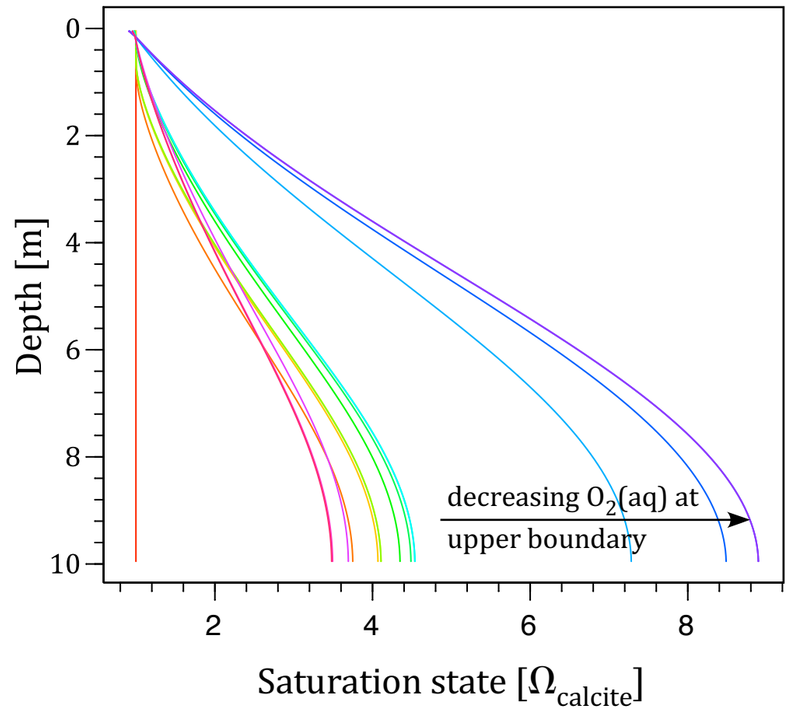
Depth [m]
0
2
4
6
8
10
decreasing O_2(aq) at
upper boundary
2
4
6
8
Saturation state [$\Omega_{calcite}$]

f

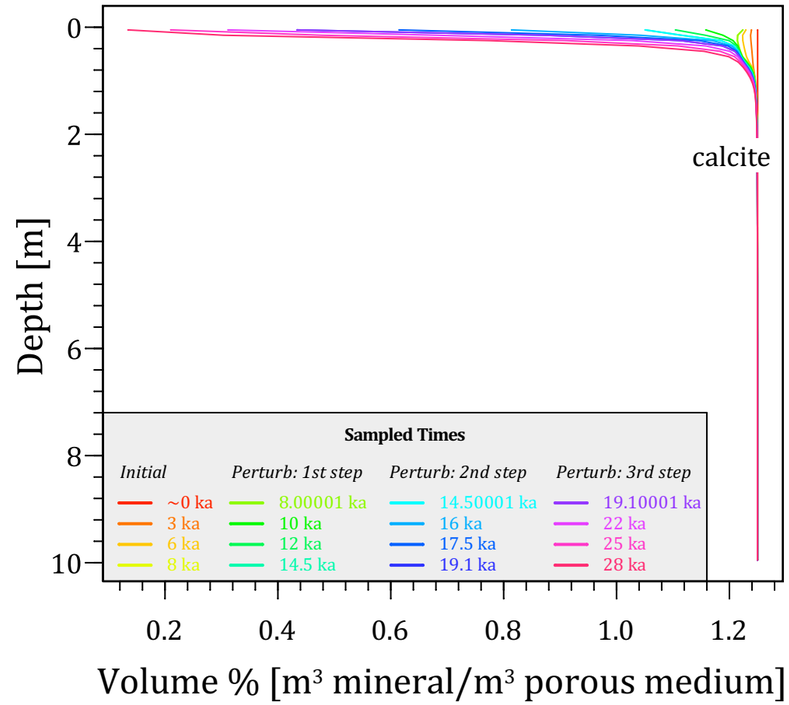
Depth [m]
0
2
4
6
8
10
calcite
Sampled Times
Initial
~0 ka
3 ka
6 ka
8 ka
Perturb: 1st step
8.00001 ka
10 ka
12 ka
14.5 ka
Perturb: 2nd step
14.50001 ka
16 ka
17.5 ka
19.1 ka
Perturb: 3rd step
19.10001 ka
22 ka
25 ka
28 ka
0.2
0.4
0.6
0.8
1.0
1.2
Volume % [m³ mineral/m³ porous medium]

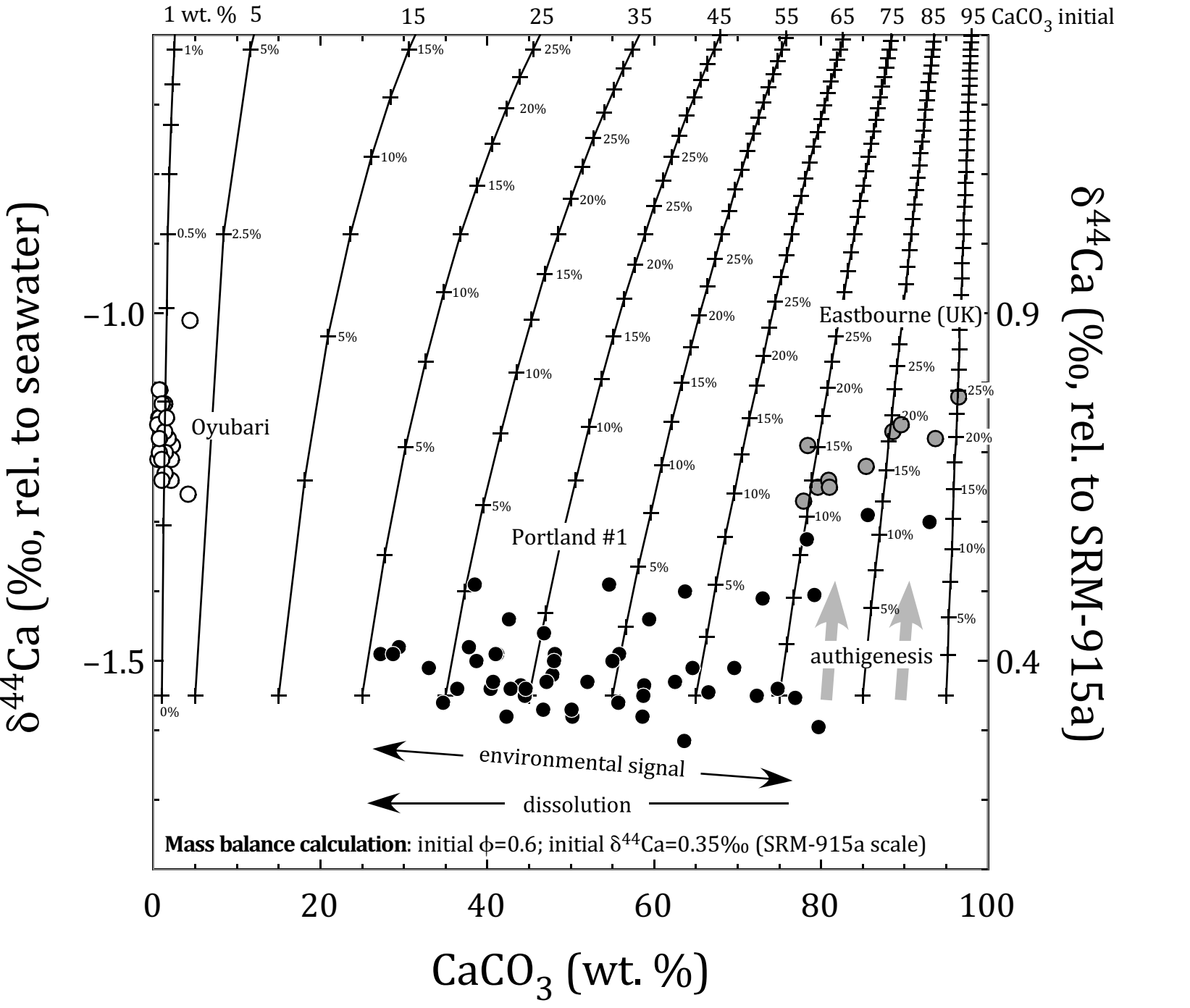
1 wt. %
5
15
25
35
45
55
65
75
85
95
CaCO3 initial
1%
5%
15%
25%
20%
25%
10%
15%
20%
25%
0.5%
2.5%
15%
10%
25%
20%
15%
25%
5%
20%
25%
10%
15%
20%
25%
5%
15%
20%
25%
10%
15%
20%
25%
5%
10%
15%
20%
25%
5%
10%
15%
20%
25%
0%
Eastbourne (UK)
Oyubari
Portland #1
authigenesis
environmental signal
dissolution
Mass balance calculation: initial ϕ=0.6; initial δ44Ca=0.35‰ (SRM-915a scale)
−1.0
−1.5
0.9
0.4
δ44Ca (‰, rel. to seawater)
δ44Ca (‰, rel. to SRM-915a)
0
20
40
60
80
100
CaCO3 (wt. %)

Calculation of Mixing Trajectories

The equations used to calculate the mixing trajectories in Fig. 3 are detailed below. The calculations assume an initial porosity (ϕ), initial $\delta^{44}Ca$ values for the carbonate and the authigenic endmember, and an initial $CaCO_3$ content (in weight percent $CaCO_3$). The calculations simply assume that the a proportion of the available pore space (volume, cm^3) is subsequently filled with pure $CaCO_3$ (ρ=2.7 g cm^{-3}), and the resultant ϕ, $\delta^{44}Ca$, and wt. % $CaCO_3$ calculated as a result:

$$\phi = \frac{\phi_{init} \cdot V_{total}[cm^3] - N_{CaCO_3\ added}[mol\ CaCO_3] \cdot \frac{100.08[g\ mol^{-1}]}{2.7[g\ CaCO_3\ cm^{-3}]}}{V_{total}[cm^3]}$$

$$\delta^{44}Ca_{bulk} = \frac{\left(\delta^{44}Ca_{init} \cdot N_{CaCO_3\ init} + \delta^{44}Ca_{added} \cdot N_{CaCO_3\ added}\right)}{N_{CaCO_3\ total}}$$

$$wt.\%\ CaCO_3 = \frac{\left(mass_{CaCO_3\ init}[g] + mass_{CaCO_3\ added}[g]\right)}{(1-\phi)V_{total} \cdot 2.7[g\ sedt\ cm^{-3}]} \cdot 100$$

The initial mass of Ca in the sediment is calculated from the initial wt. % $CaCO_3$ by:

$$N_{CaCO_3\ init} = (1-\phi) \cdot V_{total} \cdot 2.7\ g\ sedt\ cm^{-3} \cdot \frac{g\ CaCO_3}{g\ sedt} \cdot \frac{mol\ CaCO_3}{100.08\ g}$$

The bulk sediment density is assumed to be 2.7 g cm^{-3}, as is that of calcite, in order to simplify the calculations.

Model Description

S1. cGENIE Earth System Modelling

cGENIE simulates the ocean-(atmosphere)-sediment cycling of a range of elements (C, Ca, P, Fe, O) and their isotopes (where applicable), and includes a terrestrial weathering component to balance burial loss. Both organic (Hülse et al., 2018) and inorganic (i.e., carbonate) (Ridgwell and Hargreaves, 2007) carbon can be buried in the model, and the composition of the sedimentary column tracked over model time (Ridgwell, 2007), though no carbonate diagenetic processes – besides core top dissolution – are currently simulated.

In the current study, we employ an established late Paleocene tectonic and climatic model configuration (Ridgwell and Schmidt, 2010), with the spatial grid and locations of the relevant ODP sites shown in Fig. S2. The modeled Ca cycle has a global $CaCO_3$ budget based on recent Paleogene hyperthermal studies (Kirtland Turner and Ridgwell, 2013; Gutjahr et al., 2017). In this study, the steady state (and pre-event) global pelagic $CaCO_3$ burial rate in marine sediments is 14.4 Tmol $CaCO_3$ yr^{-1}. Also consistent with these studies, we omit shallow, neritic sinks, such as is induced by corals today. Modern continental weathering studies generally partition the atmospheric CO_2 consumption during weathering between silicate and carbonate weathering in the ratio ~12 Tmol CO_2 yr^{-1} to 7-12 Tmol CO_2 yr^{-1} (e.g., Gaillardet et al., 1999; Ludwig et al., 1998; Amiotte-Suchet et al., 2003; Munhoven, 2002. Assuming that (1) all silicate CO_2 consumption is associated with Ca^{2+} and that for silicate weathering, 2 mol CO_2 are consumed for every 1 mol Ca^{2+} released but (2) CO_2 is

consumed only in a 1:1 with $CaCO_3$ in carbonate weathering, leads to an approximate 2:3 split in riverine Ca^{2+} supply between silicate vs. carbonates. We therefore partition the total 14.4 Tmol Ca^{2+} yr^{-1} supply required to balance carbonate burial into 6 Tmol yr^{-1} from silicates, and 8.4 Tmol yr^{-1} derived from the weathering of terrestrial carbonates. We further assume that of the 6 Tmol yr^{-1} of silicate weathering, 4 Tmol yr^{-1} is Ca^{2+} and 2 Tmol yr^{-1} is Mg^{2+}. Because carbonate deposition and burial is assumed only to occur in the form of $CaCO_3$ in the model, we prescribe a fixed 2 Tmol yr^{-1} hydrothermal exchange of Mg^{2+} for Ca^{2+}, hence balancing the global budgets of both Ca^{2+} and Mg^{2+}.

In terms of the Ca isotope cycle (Fig. S2), the $\delta^{44}Ca$ of weathering calcium-silicate minerals is assumed to be 0.94 ‰, with 0.60‰ for the $\delta^{44}Ca$ of terrestrial carbonates (Fantle and Tipper, 2014). Hydrothermal $\delta^{44}Ca$ is assumed to have a $\delta^{44}Ca$ of 0.9‰ (Blattler et al., 2011). Finally, we set the fractionation factor between biogenic carbonates and seawater Ca^{2+} at $\Delta^{44}Ca$ = -1.1‰ (Holmden et al., 2012), but discuss and test alternative assumptions regarding the fractionation factor below.

For completeness, we include carbon isotopes in cGENIE, as described in Kirtland Turner and Ridgwell (2016). To improve the balance of the long-term C cycle, we prescribe a fixed burial flux of organic carbon to marine sediments of 2.57 Tmol yr^{-1}, which is isotopically fractionated by -30.0‰ relative to the $\delta^{13}C$ of total dissolved inorganic carbon in the surface ocean. Balancing the carbon budget then requires 8.57 Tmol yr^{-1} of volcanic CO_2 outgassing ($\delta^{13}C$ = -6‰), and a $\delta^{13}C$ of weathered carbonates on land of 3‰ – all plausible and modern-like values. Consequently, the mean $\delta^{13}C$ of newly deposited carbonate is that of weathering carbonates (3‰) and the geologic carbon isotope cycle is balanced (the specific organic carbon burial flux was chosen to simplify the C isotope budget). Carbonate and silicate weathering are both assumed to be responsive only to global mean surface land temperature, the parameterizations of which are utilized by Berner (1994) and Brady (1991), respectively, and described and evaluated in full by Lord et al. (2015). The reference value for the mean annual air temperature over land for both weathering processes is 19.0°C.

To spin up the isotope cycles in the model, we take the model spin-up from Gutjahr et al. (2017) which lacked explicit representation of $\delta^{44}Ca$, set the isotopic value of the dissolved calcium in the ocean (which has a mean concentration of 18.2 mmol kg^{-1}) to 1.92 ‰ (Fantle and Tipper, 2014), and then run the cGENIE model in an accelerated mode (Lord et al., 2015) for a total of 2 Ma.

The specific PETM simulations utilized a CO_2 emissions forcing to the atmosphere that was identical to that of (i) Gutjahr et al. (2017), or (ii) Gibbs et al. (2016) (i.e., twice the carbon flux of Zeebe et al., 2009). A simulation that matched the Cui et al. (2011) carbon emissions scenario was also run, though did not include Ca isotopes. Control scenarios that had no carbon forcing, as well as no change in Ca isotopic fractionation factor, were also conducted. All experiments were run following the spin-up for 200 ka from the start of PETM onset.

S2. CrunchTope modeling of sedimentary diagenesis

The multicomponent reactive flow and transport code CrunchTope (Druhan et al., 2013; Steefel et al., 2014) was used to simulate diagenetic reactions in the sedimentary column. CrunchTope considers both thermodynamics and kinetics, and includes a solid solution model for simulating isotopic exchange (accessed using the ISOTOPE block in the input file); the solid phase may either back-react ('bulk' option in the ISOTOPE block) or be unreactive ('none' option). The means by which recrystallization is simulated is described in Section 1.3 of Druhan et al. (2013). Mineral reaction rates are parameterized as transition state theory-like (TST) rate laws, in which rate constants, surface areas, chemical affinity dependencies, and saturation state may all be considered. Rate laws may be 'dissolution only' or 'precipitation only', in which cases precipitation or dissolution, respectively, are suppressed. Monod, as well as irreversible, rate formulations are also

available (see below). Modeled transport may be diffusive or advective, and diffusion may be considered on a species-by-species basis.

The modeled sections presented herein were assumed to be influenced only by diffusion, and species-specific diffusion coefficients were employed (at T=13˚C; Table S1; Tables 4.3, 4.7, and 4.8, Eqns. 4.4, 4.57, 4.58, and 4.59 – P=1000 bar, S=35 permil where appropriate – in Boudreau (1997); aqueous silica from Rebreanu et al. (2008); glucose from Ribeiro et al. (2006)), and a cementation exponent (m: $D_{sedt} = \phi^{-m}$) between one and two was used. Burial rates varied between ~10 m/Ma and 150 m/Ma over all the simulations.

CrunchTope was used to simulate authigenic precipitation and recrystallization scenarios, in which the saturation state, oxygen, and pH outputs from cGENIE were used to constrain the temporal evolution of the upper boundary condition. The evolution of the upper boundary was necessarily stepwise, and not continuous, as CrunchTope does not permit the former. Instead, we utilized the stop-restart functionality in CrunchTope, which allowed us to change the upper boundary condition at specific times (Table S2). The 80 ka overshoot portion of the PETM was simulated in CrunchTope assuming two initial lithologies: carbonate-poor over the upper ~25 cm (ODP Site 1221 analog) and carbonate-rich (ODP Site 1212 analog). The initial and burial lithologies (i.e., volume fractions of minerals in the initial column and in the burial flux at the upper boundary), burial rates, and porosities of the clay-rich and carbonate-rich sections are also listed in Table S2.

In addition, the extent to which the solid is assumed to be open to back-reaction was also varied in the simulations: in some simulations, the pre-existing carbonate was assumed to be unreactive while in others, all of the carbonate solid was assumed to be open to back-reaction with the pore fluid. The implementation of this feature in CrunchTope is described in detail by Druhan et al. (2013). The siliciclastic solids (kaolinite and quartz) were constrained to be unreactive over the time scale of the simulations, while the rate constants of the carbonate solid were varied over a range of values. Porosity, therefore, only varied as a function of the initial state and the amount of calcite added.

The reactive transport model results presented are not steady state results (with respect to Ca isotopes). Because burial is in operation, and the solid lithology varies with depth, the model does not necessarily reach steady state with respect to the Ca isotopic composition of the solid and pore fluid. In the authigenic simulations, no dissolution of the solid phase is permitted; thus, the pore fluid does not vary with depth and could technically be described as at steady state. However, the solid in this scenario has authigenic carbonate being added to it constantly from the upper boundary, and is constantly being buried and moved away from the interface. Because the depth zone over which authigenic carbonate is added to the model section is limited, and burial operates, there are no cases in which the pore space is filled completely, which (in the absence of any removal flux) is what would be required to reach a steady state with respect to the solid. In any given time interval over which the chemistry of the upper boundary is constant, then, steady state is not necessarily achieved (nor is it expected). In the recrystallization scenarios investigated, the same is true of both the solid and the pore fluid δ^{44}Ca; again, the primary driver here is the solid composition, which impacts pore fluid δ^{44}Ca via dissolution. However, the chemistry of the pore fluid in each simulated scenario (e.g., saturation state, pH) is generally in steady state in the depth regime over each of the three intervals.

It should be noted that there are numerical mixing effects on the solid phase in the CrunchTope simulations when burial is on. A variety of simulations were conducted to determine if changing the grid spacing (i.e., *dz*) or burial rate could reduce the effect, but neither did. Thus, we present the simulations with the caveat that they contain a small degree of numerical mixing in the solid (which is pointed out in the mixing figures), similar to what would be expected due to bioturbation.

In order to investigate the impact of variable O_2(aq) concentrations at the upper boundary, a simplified redox ladder consisting of aerobic oxidation of organic matter, denitrification, and

sulfate reduction was simulated. In CrunchTope, the BIOMASS formulation adapts the rate scheme for microbial reactions proposed by Jin and Bethke (2003; 2005), which are assumed to obey Monod-type kinetics:

$$rate = k_{max} m_B \frac{m_i}{m_i + K_{half}} \frac{K_{in} + m_j}{K_{in}} \left(1 - e^{\frac{\Delta G_r + m\Delta G_p}{\chi RT}}\right) \quad [1]$$

where k_{max} is the maximum rate constant (yr^{-1}), m_B is biomass concentration, m_i is concentration of the electron donor or acceptor that controls the Monod dependence, m_j is concentration of the electron or acceptor that inhibits reaction, K_{half} is the half-saturation constant, K_{in} is the inhibition constant, ΔG_r is the Gibbs free energy of the redox reaction, ΔG_p is the phosphorylation potential, m is the number of ATPs synthesized in the reaction, and χ is the average stoichiometric number for the overall reaction (Jin and Bethke, 2005). Reactions utilizing acetate as the electron donor, as well as those using glucose as the electron donor, are shown in Table S3. Sulfide oxidation is included in the reaction network, and its rate assumed to be described by an irreversible rate law (*i.e.*, $rate = k \prod_i a_i^n$; Millero et al., 1987)

The Monod expression for sulfate reduction depends on total concentrations of the electron acceptor (acetate and glucose) and sulfate, and was inhibited by both O_2(aq) and nitrate concentrations (Table S3). In the simple construct employed, concentrations of the electron donor are maintained <100 μM over the course of the simulations but never decrease to zero. The biomass concentration was assumed to be constant.

Maximum modeled sulfate reduction rates were $<10^{-5}$ mol $SO_4^{2-} kg_{water}^{-1} year^{-1}$, which is comparable to those in deep-sea sediments (e.g., Goldhaber and Kaplan, 1975; Canfield, 1991) and significantly lower than continental margin sediments in which sulfate concentrations are driven to zero over ~1 m to tens of meter length scales (rate ~ $<10^{-2}$ mol $SO_4^{2-} L^{-1} year^{-1}$; e.g., Dale et al., 2008).

The redox ladder model allows isotopically distinct calcium carbonate to dissolve but precipitation is not permitted. Thus, carbonate can dissolve and buffer pH in the sediment, which is modeled as a clay-rich sediment with 96.4% (by volume) unreactive kaolinite ($log\ k = 10^{-30} mol\ m^{-2} s^{-1}$) and 3.6% $CaCO_3$, the latter of which has a $\delta^{44}Ca$ value of 0.6‰ on the SRM-915a scale. Calcite dissolution rates are constrained by rate constants (10^{-3} to $10^{-5}\ mol\ m^{-2} s^{-1}$) that generate dissolution rates that are considerably slower than those observed in laboratory experiments at circumneutral pH (e.g., Shiraki et al., 2000). More appropriately, such rate constants create a dissolution zone that is generally less than 25 cm, which is consistent with what is assumed for chemical burndown during with the PETM.

Supplemental Tables

Table S1: Diffusion coefficients used in CrunchTope TRANSPORT block.

Species name in CrunchTope input file	**Diffusion coefficient** [a] [m^2/yr]
H+	0.23531
Na+	0.03129
Cl-	0.04823
OH-	0.12653
Mg++	0.01672
Sr++	0.01857
Ca40++	0.01869
Ca44++	0.01869
NH4+	0.04624
NO3-	0.04525
Acetate	0.02480
Acetic_acid(aq)	0.02789
SO4--	0.02490
HCO3-	0.02723
CO3--	0.02181
Al+++	0.01585
CO2(aq)	0.04255
NH3(aq)	0.04952
N2(aq)	0.04019
O2(aq)	0.05385
H2S(aq)	0.03984
HS-	0.04356
H2(aq)	0.04522

Relevant TRANSPORT block inputs	**Value/range**	**Comments**
space_units	meters	
time_units	years	
calculate_diffusion	0.020	Diffusion coefficient of any species w/ missing D_25 entry
cementation_exponent	1.0 – 2.0	
dispersivity	0.0	

a – Diffusion coefficients were calculated at 13˚C using the following references: Tables 4.3, 4.7, and 4.8, Eqns. 4.4, 4.57, 4.58, and 4.59 – P=1000 bar, S=35 permil where appropriate – in Boudreau (1997); aqueous silica from Rebreanu et al. (2008); glucose from Ribeiro et al. (2006).

Table S2: Summary of conditions associated with CrunchTope reactive transport modeling.

	'low O_2(aq)' runs — 20 ka [a]		
Parameter \ **Input file**	**Diss-1**	**Diss-2** restart file	**Diss-3** restart file
Variable in time			
Upper boundary Ω [b]	0.92	0.70	0.84
Column Ω [b]	1	na [c]	na [c]
Temperature *	13˚C	13˚C	13˚C
pH (initial column)	7.50	na [c]	na [c]
pH (upper boundary)	7.33	7.17	7.10
O_2(aq) µM	140	50	160
Time interval	6.5 ka	4.6 ka	8.9 ka
Constant in time			
Column height/dz	10 m/0.1 m	Mineral specific surface area	1 m^2/g [e]
Lower boundary state	open/closed		
Initial porosity	0.65	*Ca isotope-specific*	
Burial porosity	0.65	Pore fluid δ^{44}Ca (initial)	1.9‰
Burial lithology	3.6% $CaCO_3$	Bulk solid δ^{44}Ca (initial)	0.6‰
Burial rate	10-60 m/Ma	Solid δ^{44}Ca (burial)	0.6‰
Diffusion coefficients [d]	$f(T,\phi)$	$\alpha_{diffusion}$	1.000
Time step (max)	1 year	$\alpha_{precipitation}$	1.000
Time step (init)	10^{-14} year	$\alpha_{dissolution}$	1.000

	'authigenic precipitation' runs — 80 ka		
Parameter \ **Input file**	**Precip-1**	**Precip-2** restart file	**Precip-3** restart file
Variable in time			
Upper boundary Ω [b]	1.08	1.20	1.05
Column Ω [b]	1	na [c]	na [c]
Temperature *	13˚C	13˚C	13˚C
pH (initial column)	7.26	na [c]	na [c]
pH (upper boundary)	7.26	7.36	7.46
O_2(aq) µM	na	na	na
Time interval	16 ka	24 ka	40 ka
Constant in time			
Column height/dz	2 m/0.01 m	Mineral specific surface area	1 m^2/g [e]
Initial porosity	0.75	Burial porosity	0.75
Initial lithology (1212-like)		Initial lithology (1221-like)	
Upper 11 cm	80% $CaCO_3$	*Upper 25 cm*	1% $CaCO_3$
Lower 189 cm	93/96% $CaCO_3$	*Lower 175 cm*	40/65% $CaCO_3$
Burial lithology (1212-like)	95% $CaCO_3$	Burial lithology (1221-like)	82.5% $CaCO_3$ 1% $CaCO_3$
Lower boundary state	closed	Time step (init)	10^{-14} year
Burial rate	5-150 m/Ma	Time step (max)	1 year
		Diffusion coefficients [d]	$f(T,\phi)$
Ca isotope-specific			
Pore fluid δ^{44}Ca (initial)	1.9‰	$\alpha_{diffusion}$	1.000
Bulk solid δ^{44}Ca (initial)	0.6‰	$\alpha_{precipitation}$	1.000
Solid δ^{44}Ca (burial)	0.6‰	$\alpha_{dissolution}$	1.000

a – '*low O_2(aq)*' do not consider a precipitating carbonate phase, only a dissolving phase with a fixed isotopic composition of 0.6‰.
b – Saturation state with respect to pure calcite.
c – 'na' indicates geochemistry picked up from end of previous simulation (i.e., during restart).
d – See Table S3 for diffusion coefficients used.
e – Specific mineral surface area the same for all minerals in simulations.
* – Over entire model domain; temperature (T) is not dynamically updated in CrunchTope, so no temperature perturbation is applied in the reactive transport simulations. The assignment of temperature impacts diffusion coefficients and equilibrium constants. In the 'low O_2(aq)' runs, the impact of T on equilibrium constants was not considered.

Table S3: Parameters used in aqueous kinetic database utilized in CrunchTope. All reactions are written for one electron (e^-) transferred.

Aerobic oxidation					*log K*[a]
$e^- donor = acetate$: $\frac{1}{8}CH_3COO^- + \frac{1}{4}O_2(aq) \leftrightarrow \frac{1}{4}HCO_3^- + \frac{1}{8}H^+$					18.3437
$e^- donor = glucose$: $\frac{1}{24}C_6H_{12}O_6 + \frac{1}{4}O_2(aq) \leftrightarrow \frac{1}{4}HCO_3^- + \frac{1}{4}H^+$					19.6922
Type	K_{half}	K_{in}	k_{max}	bq[b]	χ
MonodBiomass	Total acetate: 1e-03 O_2(aq): 1e-03	none	1	2	1

Denitrification					*log K*[a]
$e^- donor = acetate$: $\frac{1}{8}CH_3COO^- + \frac{1}{5}NO_3^- + \frac{3}{40}H^+ \leftrightarrow \frac{1}{10}H_2O + \frac{1}{4}HCO_3^- + \frac{1}{10}N_2(aq)$					17.5697
$e^- donor = glucose$: $\frac{1}{24}C_6H_{12}O_6 + \frac{1}{5}NO_3^- \leftrightarrow \frac{1}{10}H_2O + \frac{1}{4}HCO_3^- + \frac{1}{10}N_2(aq) + \frac{1}{20}H^+$					18.9183
Type	K_{half}	K_{in}	k_{max}	bq[b]	χ
MonodBiomass	Total acetate: 1e-03 $NO_3^-(aq)$: 1e-03	O_2(aq): 1e-06	1	2	1

Sulfate Reduction					*log K*[a]
$e^- donor = acetate$: $\frac{1}{8}CH_3COO^- + \frac{1}{8}SO_4^{2-} \leftrightarrow \frac{1}{4}HCO_3^- + \frac{1}{8}HS^-$					1.0541
$e^- donor = glucose$: $\frac{1}{24}C_6H_{12}O_6 + \frac{1}{8}SO_4^{2-} \leftrightarrow \frac{1}{4}HCO_3^- + \frac{1}{8}HS^- + \frac{1}{8}H^+$					2.4026
Type	K_{half}	K_{in}	k_{max}	bq[b]	χ
MonodBiomass	Total acetate: 1e-03 $SO_4^{2-}(aq)$: 1 to 10e-03	O_2(aq): 1e-06 $NO_3^-(aq)$: 1e-03	1	2	1

Sulfide oxidation					*log K*[a]
$\frac{1}{8}HS^- + \frac{1}{4}O_2(aq) \leftrightarrow \frac{1}{8}H^+ + \frac{1}{8}SO_4^{2-}$					17.2896
Type	*Dependence (and n value)*	*k*			
Irreversible	Total HS^-(aq): 1.0 Total O_2(aq): 1.0 H^+: -0.16	0.5			

a – *log* K_{eq} values calculated using SUPCRT (Johnson et al., 1992).
b – $bq = m \cdot \Delta G_p$ (e.g., Jin and Bethke, 2003; 2005)

Figure S1

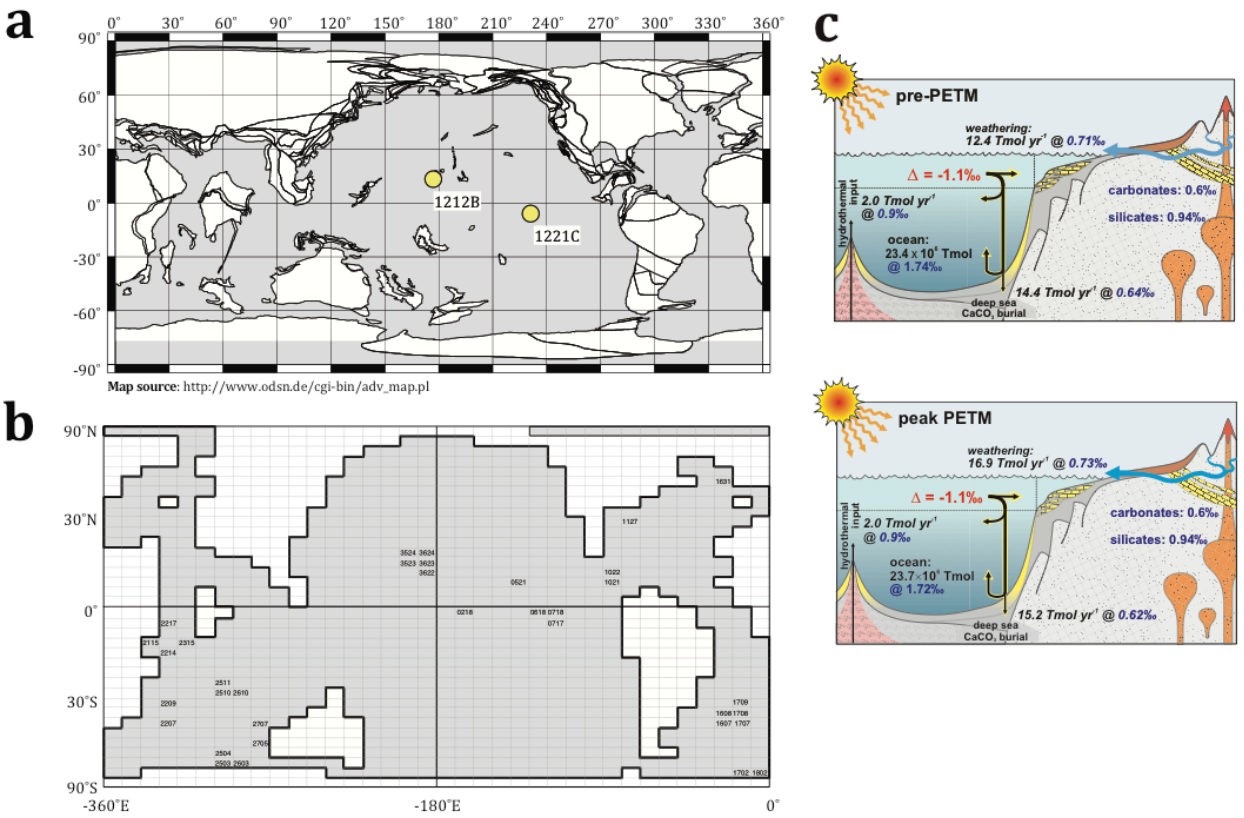

(a) Paleogeographical map at ~55 Ma (http:www.odsn.de/cgi-bin/adv_map.pl), with ODP Sites 1212 and 1221 shown. (b) cGENIE grid showing location and designations of sites saved in simulations presented. (c) Schematic diagrams of Ca cycle applied in cGENIE for pre- and peal-PETM conditions.

Figure S2

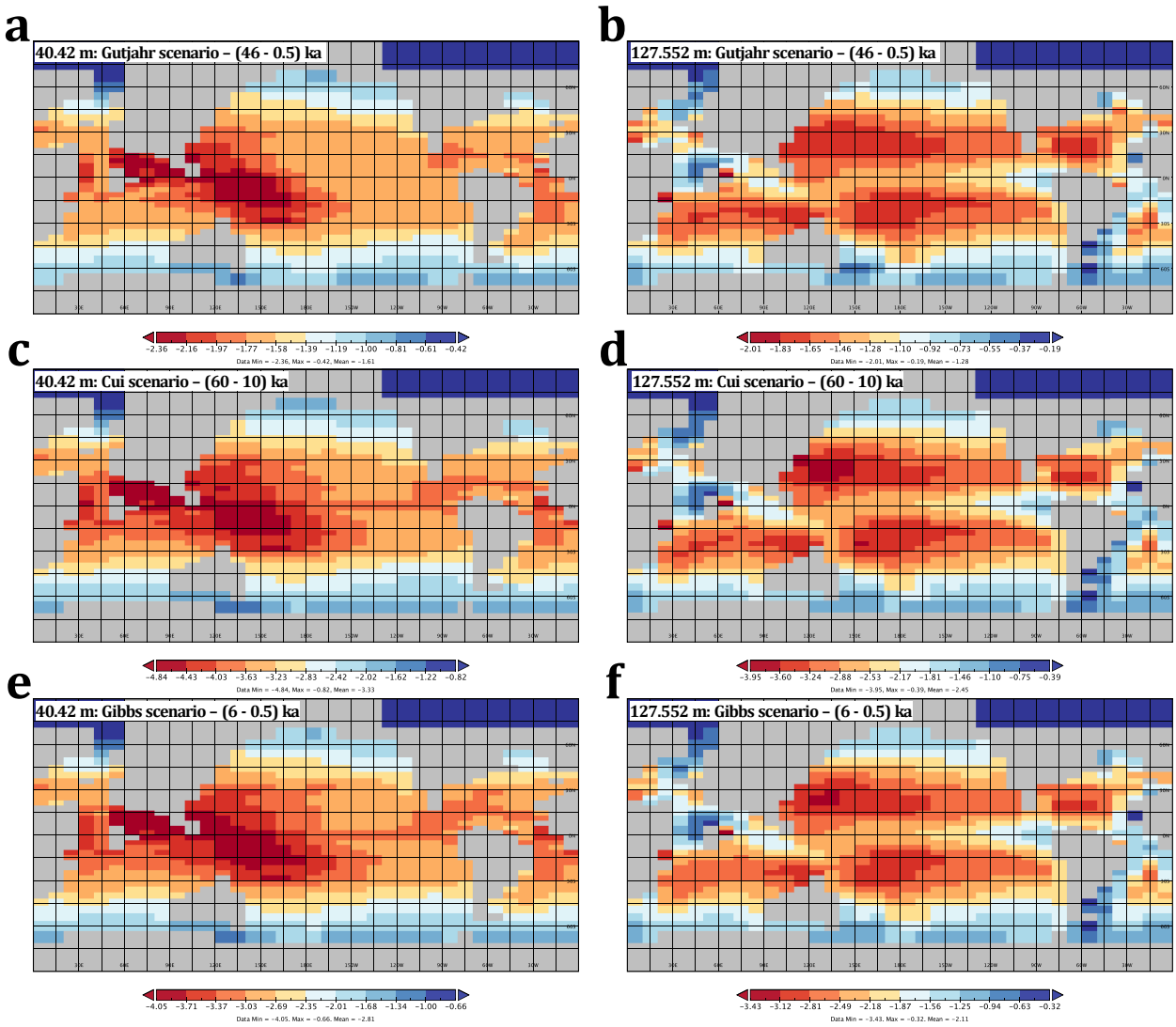

cGENIE model output for PETM scenarios described in the text and in SI Section S1. Saturation state ($\Omega_{calcite}$, i.e., saturation state with respect to calcite) differences between pre- and peak-PETM in the surface ocean box (40.42 meters mid-depth) and the next, deeper water column box (127.552 meters mid-depth) for the three scenarios run: (a-b) Gutjahr et al. (2017), (c-d) Cui et al. (2011), and (e-f) Gibbs et al. (2016).

Figure S3

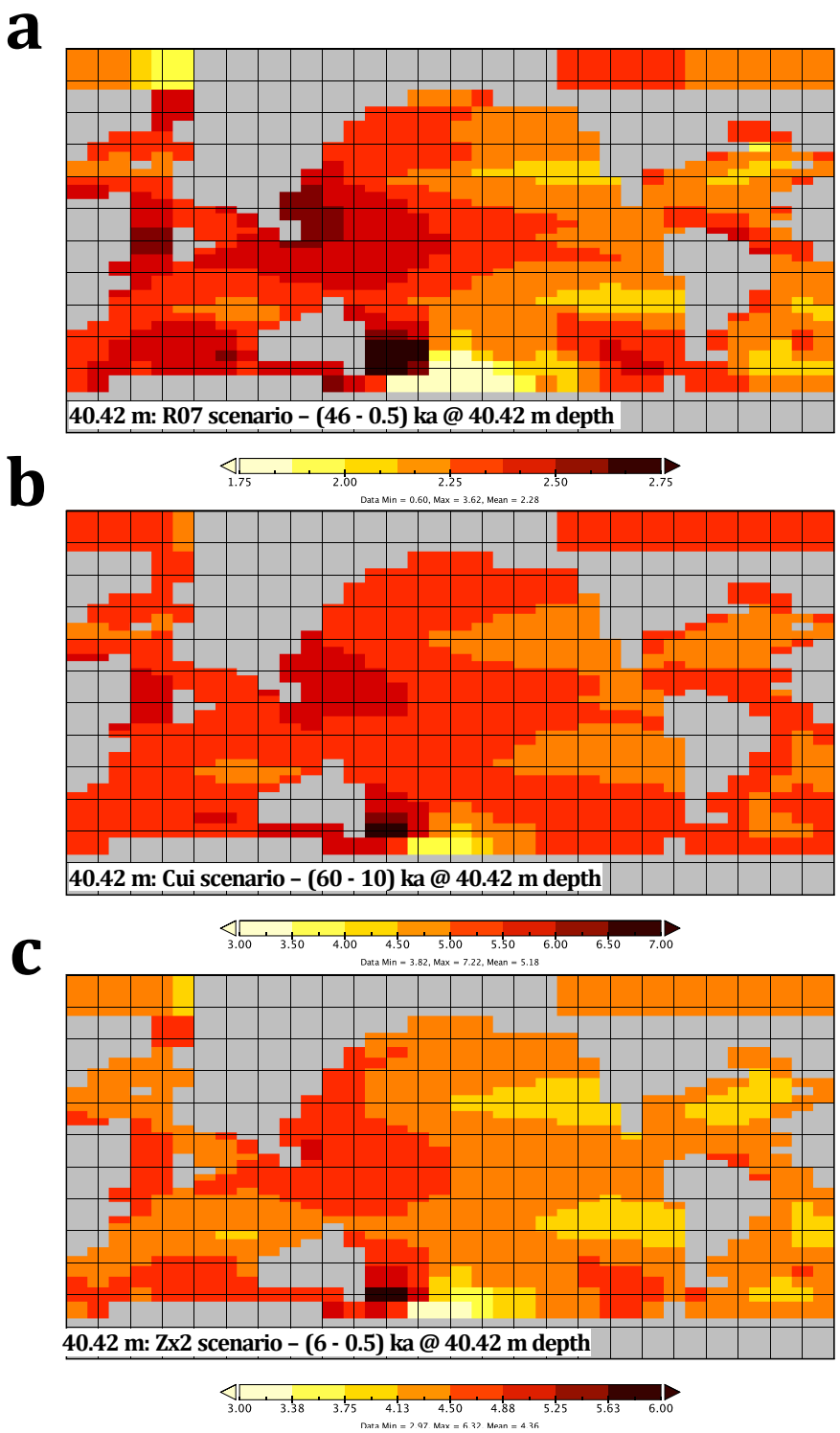

cGENIE model output for PETM scenarios described in the text and in SI Section S1. Temperature differences between pre- and peak-PETM in the surface ocean box (40.42 meters mid-depth) for the three scenarios run: (a) Gutjahr et al. (2017), (b) Cui et al. (2011), and (c) Gibbs et al. (2016).

Figure S4

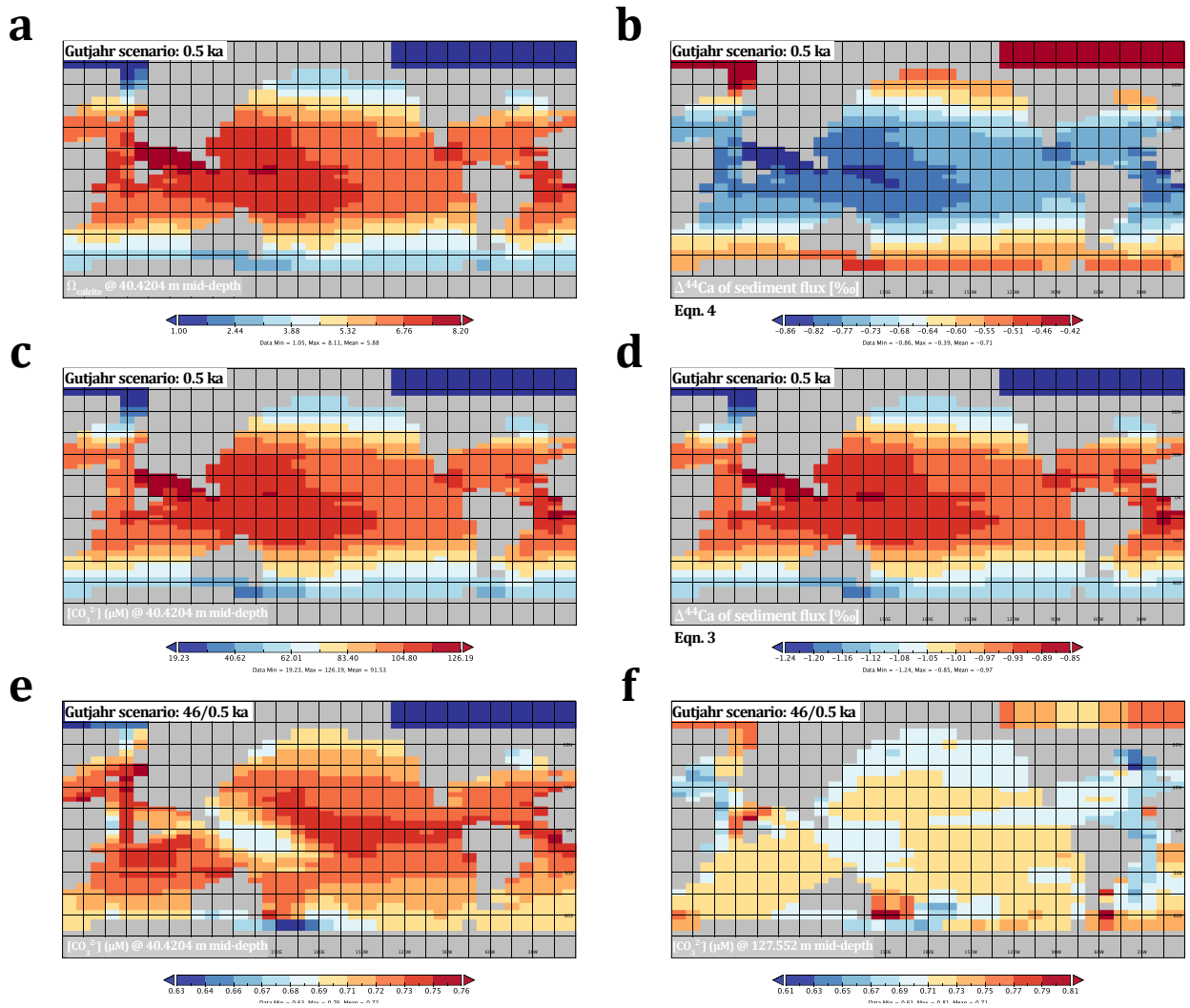

cGENIE model output for PETM scenarios described in the text and in SI Section S1. (a) Saturation state with respect to calcite ($\Omega_{calcite}$) in the surface ocean, and (b) the corresponding $\Delta^{44}Ca$ (‰) of the carbonate output flux to the sedimentary column (relative to the surface ocean: $\delta^{44}Ca$ of sedimentation flux - $\delta^{44}Ca$ of surface ocean) at 0.5 ka simulation time (pre-event). (c) Carbonate ion concentration (μM) in the surface ocean, and (d) the corresponding $\Delta^{44}Ca$ (‰) of the carbonate output flux to the sedimentary column (relative to the surface ocean: $\delta^{44}Ca$ of sedimentation flux - $\delta^{44}Ca$ of surface ocean) at 0.5 ka simulation time (pre-event). Carbonate ion concentration (μM) at 46 ka (peak event) relative to 0.5 ka (pre-event) at (e) 40.4204 meters depth and (f) 127.552 meters depth. All panels refer to the Gutjahr et al. (2017) carbon flux scenario. The equation numbers indicated in panels (b) and (d) refer to in-text equations used to constrain the Ca isotopic composition of the output flux.

Figure S5

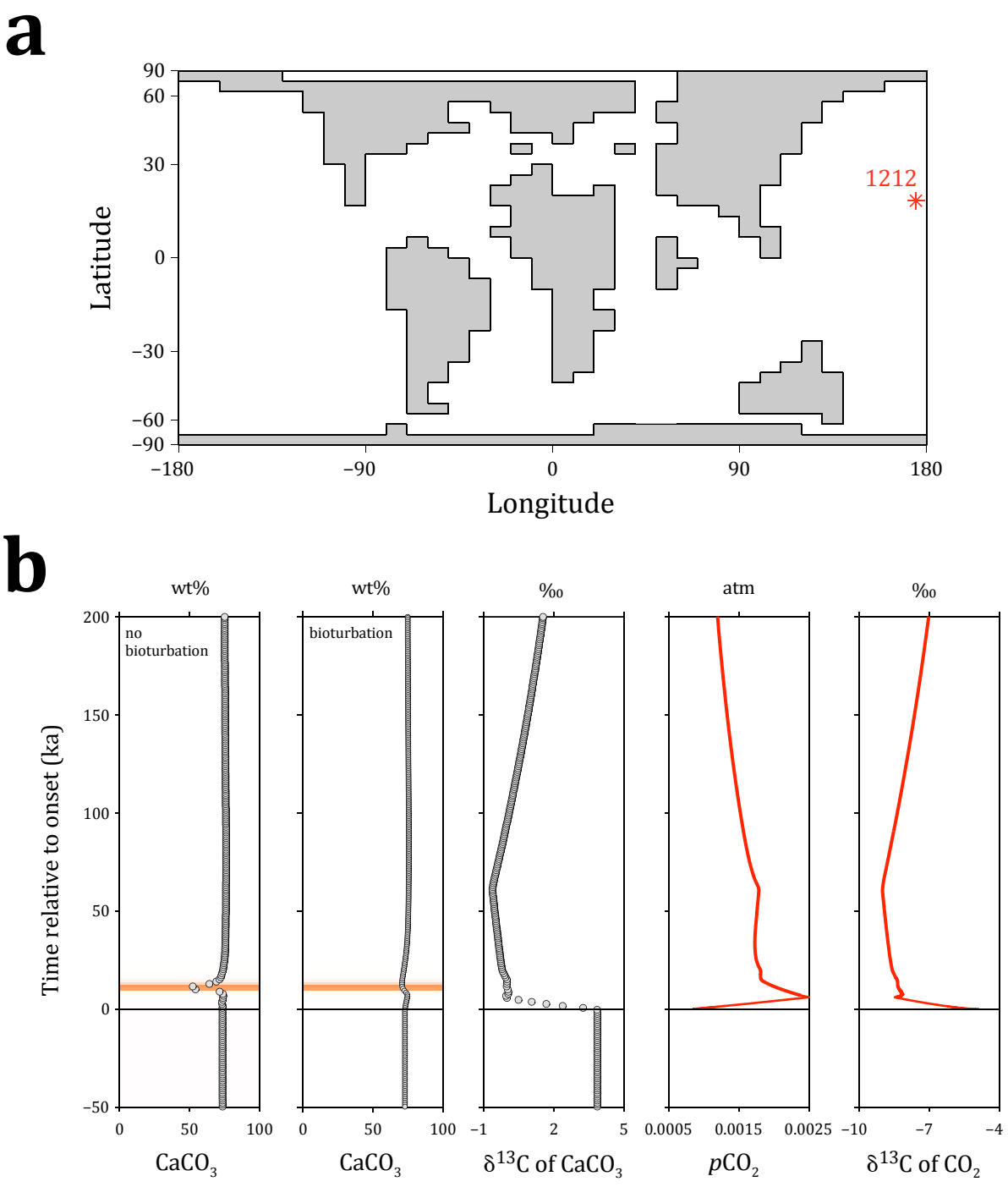

(a) Paleogeographical map with location of Site 1212 indicated, and (b) cGENIE model $CaCO_3$ (wt. %) output with bioturbation and no bioturbation (orange shading indicates the zone of dissolution associated with the PETM). Also included are model output for the $\delta^{13}C$ of the $CaCO_3$ output flux (‰), the pCO_2 of the model atmosphere (atm), and the $\delta^{13}C$ of atmospheric CO_2 (‰).

Figure S6

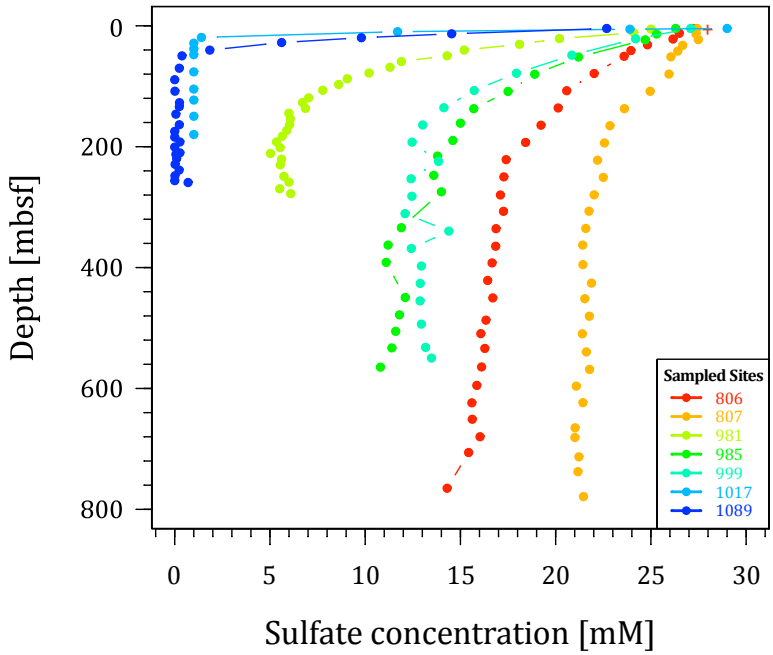

Sulfate concentration profiles at Ocean Drilling Program selected sites. Data from Janus database: http://www-odp.tamu.edu/database/. The red cross at depth = 0 mbsf is 28 mM, the approximate concentration of modern seawater.

Figure S7

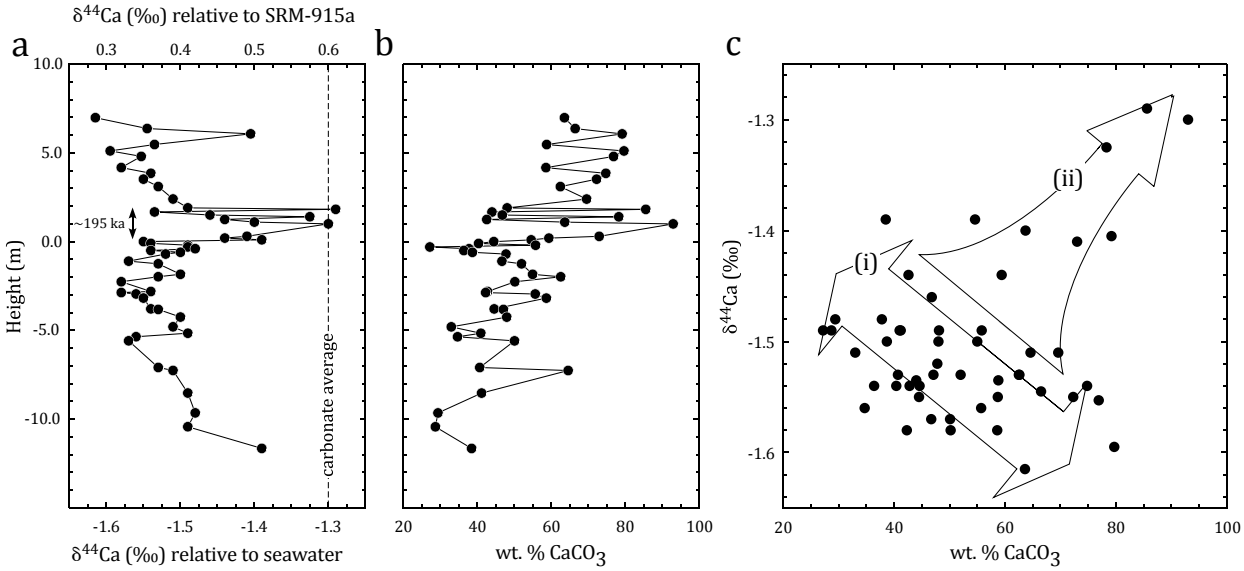

(a) Calcium isotopic ($\delta^{44}Ca$, ‰ on the seawater and SRM-915a scales) and (b) carbonate concentration (wt. %) from the Portland #1 core, as reported by Du Vivier et al. (2015), plotted as a function of stratigraphic height (m). (c) Cross-plot of Ca isotope and $CaCO_3$ concentration data, the general trends of which are denoted by (i) and (ii). Note that neither trend highlighted by the arrows in (c) are meant to indicate any particular mechanism, but simply to highlight the two arrays that are present. One might, for instance, consider trend (i) to be a function of two mechanisms, one of which controls the increase in $CaCO_3$ (e.g., a decrease in clastic relative to carbonate deposition) and one of which controls the $\delta^{44}Ca$ increase (e.g., authigenesis).

References

Amiotte-Suchet, P., Probst, J.L. and Ludwig, W. (2003) Worldwide distribution of continental rock lithology: Implications for the atmospheric/soil CO2 uptake by continental weathering and alkalinity river transport to the oceans. *Global Biogeochem Cy* 17.

Berner, R.A. (1994) 3GEOCARB-II – A Revised Model of Atmospheric CO_2 over Phanerozoic Time. *Am J Sci* 294, 56-91.

Blättler, C.L., Jenkyns, H.C., Reynard, L.M. and Henderson, G.M. (2011) Significant increases in global weathering during Oceanic Anoxic Events 1a and 2 indicated by calcium isotopes. *Earth Planet Sci Lett* 309, 77-88.

Boudreau, B.P. (1997) Diagenetic models and their implementation: modelling transport and reactions in aquatic sediments. Springer, Berlin; New York.

Brady, P.V. (1991) The Effect of Silicate Weathering on Global Temperature and Atmospheric CO_2. *J Geophys Res-Sol Ear* 96, 18101-18106.

Canfield, D.E. (1991) Sulfate reduction in deep-sea sediments. *Am J Sci* 291, 177-188.

Cui, Y., Kump, L. R., Ridgwell, A. J., Charles, A. J., Junium, C. K., Diefendorf, A. F., Freeman, K. H., Urban, N. M., and Harding, I. C., (2011). Slow release of fossil carbon during the Palaeocene-Eocene Thermal Maximum. *Nature Geoscience* 4, 481-485.

Dale, A.W., Regnier, P., Knab, N.J., Jorgensen, B.B. and Van Cappellen, P. (2008) Anaerobic oxidation of methane (AOM) in marine sediments from the Skagerrak (Denmark): II. Reaction-transport modeling. *Geochim Cosmochim Acta* 72, 2880-2894.

Druhan, J.L., Steefel, C.I., Williams, K.H. and DePaolo, D.J. (2013) Calcium isotope fractionation in groundwater: Molecular scale processes influencing field scale behavior. *Geochim Cosmochim Acta* 119, 93-116.

Fantle, M. S. and Tipper, E. T., (2014). Calcium isotopes in the global biogeochemical Ca cycle: Implications for development of a Ca isotope proxy. *Earth Science Reviews* 129, http://dx.doi.org/10.1016/j.earscirev.2013.10.004, 148-177.

Gaillardet, J., Dupre, B., Louvat, P. and Allegre, C.J. (1999) Global silicate weathering and CO_2 consumption rates deduced from the chemistry of large rivers. *Chem Geol* 159, 3-30.

Gibbs, S.J., Bown, P.R., Ridgwell, A., Young, J.R., Poulton, A.J. and O'Dea, S.A. (2016) Ocean warming, not acidification, controlled coccolithophore response during past greenhouse climate change. *Geology* 44, 59-62.

Goldhaber, M.B. and Kaplan, I.R. (1975) Controls and Consequences of Sulfate Reduction Rates in Recent Marine Sediments. *Soil Science* 119, 42-55.

Gutjahr, M., A. Ridgwell, A., Sexton, P.F, Anagnostou, E., Pearson, P.N., Pälike, H., Norris, R.D., Thomas, E., and Foster, G.L. (2017) Very large release of mostly volcanic carbon during the Paleocene-Eocene Thermal Maximum Paleocene-Eocene Thermal Maximum, *Nature* 548, doi:10.1038/nature23646

Holmden, C., Papanastassiou, D. A., Blanchon, P., and Evans, S., (2012). $\delta^{44/40}$Ca variability in shallow water carbonates and the impact of submarine groundwater discharge on Ca-cycling in marine environments. *Geochimica Cosmochimica Acta* 83, 179-194, doi:10.1016/j.gca.2011.12.031.

Hülse, D., Arndt, S., Daines, S., Regnier, P. and Ridgwell, A. (2018) OMEN-SED 1.0: a novel, numerically efficient organic matter sediment diagenesis module for coupling to Earth system models. *Geoscientific Model Development* 11, 2649-2689.

Jin, Q. S. and Bethke, C. M. (2003) A new rate law describing microbial respiration. *Appl Environ Microbiol* 69, 2340-2348.

Jin, Q. S. and Bethke, C. M. (2005) Predicting the rate of microbial respiration in geochemical environments. *Geochim Cosmochim Acta* 69, 1133-1143.

Kirtland Turner, D. and Ridgwell, A. (2013) Recovering the true size of an Eocene hyperthermal from the marine sedimentary record. *Paleoceanography*, 28, 700-712, doi:10.1002/2013PA002541.

Kirtland Turner, S.K. and Ridgwell, A. (2016) Development of a novel empirical framework for interpreting geological carbon isotope excursions, with implications for the rate of carbon injection across the PETM. Earth Planet Sci Lett 435, 1-13.

Lord, N.S., A. Ridgwell, M.C. Thorne, and D.J. Lunt (2015) An impulse response function for the 'long tail' of excess atmospheric CO_2 in an Earth system model, *Global Biogeochemical Cycles*, doi: 10.1002/2014GB005074.

Ludwig, W., Amiotte-Suchet, P., Munhoven, G. and Probst, J.L. (1998) Atmospheric CO_2 consumption by continental erosion: present-day controls and implications for the last glacial maximum. *Global Planet Change* 17, 107-120.

Millero, F. J., Hubinger, S., Fernandez, M. and Garnett, S. (1987) Oxidation of H_2S in seawater as a function of temperature, pH, and ionic strength. *Environ Sci Technol* 21, 439-443.

Munhoven, G. (2002) Glacial-interglacial changes of continental weathering: estimates of the related CO_2 and HCO_3^- flux variations and their uncertainties. *Global Planet Change* 33, 155-176.

Rebreanu, L., Vanderborght, J.P. and Chou, L. (2008) The diffusion coefficient of dissolved silica revisited. *Mar Chem* 112, 230-233.

Ribeiro, A.C.F., Ortona, O., Simoes, S.M.N., Santos, C.I.A.V., Prazeres, P.M.R.A., Valente, A.J.M., Lobo, V.M.M. and Burrows, H.D. (2006) Binary mutual diffusion coefficients of aqueous solutions of sucrose, lactose, glucose, and fructose in the temperature range from (298.15 to 328.15) K. *J Chem Eng Data* 51, 1836-1840.

Ridgwell, A. and Hargreaves, J.C. (2007) Regulation of atmospheric CO_2 by deep-sea sediments in an Earth system model. *Global Biogeochem Cy* 21.

Ridgwell, A. (2007) Interpreting transient carbonate compensation depth changes by marine sediment core modeling. *Paleoceanography* 22.

Ridgwell, A. and Schmidt, D. N. (2010) Past constraints on the vulnerability of marine calcifiers to massive carbon dioxide release. *Nature Geoscience*, 3, 196-200, doi:10.1038/ngeo755.

Shiraki, R., Rock, P.A. and Casey, W.H. (2000) Dissolution kinetics of calcite in 0.1 m NaCl solution at room temperature: An atomic force microscopic (AFM) study. *Aquatic Geochemistry* 6, 87-108.

Steefel, C.I., Druhan, J.L. and Maher, K. (2014) Modeling Coupled Chemical and Isotopic Equilibration Rates. *Procedia Earth and Planetary Science* 10, 208-217.

Zeebe, R. E., Zachos, J. C., and Dickens, G. R., (2009). Carbon dioxide forcing alone insufficient to explain Palaeocene-Eocene Thermal Maximum warming. *Nature Geoscience* 2, 576-580.